Micron-scale liquid engineering for porous polymer patterning

Qingxin Zhang

Queens' College

Department of Engineering

University of Cambridge

This dissertation is submitted for the degree of

Doctor of Philosophy

September 2018

I would like to dedicate this thesis to my loving parents,

and my supervisor Dr. Ronan Daly,

for their unconditional support.

Declaration

I hereby declare that except where specified in referencing and acknowledgement to the work of others, the contents of this thesis are original and have not been submitted in whole or in part for any other degree or qualification in this, or any other University. This thesis is the results of my own work and includes nothing that is the outcome of work done in collaboration, except where specifically indicated in the text. This thesis contains 42,547 words including appendices, bibliography, footnotes, tables and equations.

Qingxin Zhang

Sep. 2018

Acknowledgements

I am most grateful to Dr. Ronan Daly, my respected supervisor for my PhD studies, for his patience, continuous encouragement and support, for equipping me with fundamental research skills and trusting me. His guidance throughout the time of my PhD and writing of this thesis. His serious scientific attitude and meticulous academic spirit has profoundly affected and inspired me, allowing me the freedom to explore. I could not have imagined having a better supervisor for my PhD study.

Besides, I would like to thank my advisor Prof. Bill O'Neill for his encouragements. Also I am grateful to Prof. Ian Hutchings, for his support of the resources in my research. My thanks also go to Dr. Ching-Hsien Chen and Dr. Wen-Kai Hsiao for their training of some experimental rigs. I acknowledge my colleague Yoanna Shams for her encouragement and help throughout my PhD. Thanks to other colleagues who made our group pleasant.

I appreciate the help from Dr. Clare Conboy with the rheology study, and Dr. Stefanie Reichelt's help on the confocal microscopy. I am grateful for Dr. Niamh Fox's help with the design and formulation of the titration, also for her other help and kindness. Thank my friend Ziyan Zhao for mCherry and GFP. Thanks to James Macdonald for his help with some FIB work.

Thanks my class-S friends Hao Li, Yuankun Luo, and Yuanjun Chen for their company and encouragement who made my life in Cambridge unforgettable. Thanks for Bingqing Zhao for the days we laughed together.

I would like to thank my parents for encouraging me to pursue this PhD degree after my undergraduate study, and their immeasurable support in my life and study.

Thanks for the financial support from the Cambridge Commonwealth, European and International Trust.

Finally, special thanks to you, who is reading my thesis.

Abstract

Porous polymer structures have a rich history of applications from insulation and impact absorption to superhydrophobic coatings, controlled drug release materials, biological scaffolds and photonic materials. Different approaches such as lithography, etching and direct templating were developed to produce porous polymers. There is still a huge development potential in the preparation techniques.

In 1994 a self-organisation technique was reported to trap and self-organise condensed water droplets at a solution surface and then imprint their shape directly into a polymer film. This single-step direct templating method operates at ambient conditions and can be processed and controlled to form a wide range of porous structures and surface functionalities. However, there are significant manufacturing challenges that have prevented this technique from reaching the market. This research tackles this problem by combining top-down techniques for precise liquid deposition utilising inkjet printing technique with the same bottom-up self-assembly processes at micron-scale by ordering drops and encapsulating materials in drops to load functional materials into the porous structure directly. This research aims firstly at controlling and simplifying the system to understand the force balances and interfacial phenomena by observing the impact behaviour of droplets generated by inkjet printing onto organic solvent and polymer, with the aid of high-speed imaging systems. Secondly to deliver a new, simple and scalable engineering solution to translate this technique to the manufacturing of materials with controlled surface properties.

Inkjet technique enables precise deposition of droplets onto substrates, with controlled volume, speed, and compatible with a wide range of materials by altering the type and dimensions of the printheads also the driving waveforms. Manipulating polymer viscosity is a new approach of regulating pore ordering and geometry. This research made a breakthrough in the porous polymer production, showing highly ordered structures, easy porosity design, biocompatible processing methods, and digitally controllable and programmable production. In addition, it is the first time obtaining highly ordered porous polydimethylsiloxane (PDMS) using droplets as templates. These porous PDMS have a huge potential in the applications of drug delivery device, biosensor, high-throughput screening, and flexible electronics.

Contents

Nomenclature

BF	Breath figure
cP	Centipoise
d	Diameter of the droplets
DMP	Dimatix materials printer
dr	Relative diameter
ds	Centre-to-centre distance between two droplets
e	Standard measure of surface stability
fps	Frames per second
g	Gravitational acceleration
GW	Glycerol water
Oh	Ohnesorge number
PDMS	Polydimethylsiloxane
R	Rayleigh number
r	Radius
Rc	Critical Rayleigh number
Re	Reynolds number
V	Velocity
We	Weber number
∅	Impact angle
α	Contact angle
ε	Volume expansion
γ	Surface tension
ΔT	Temperature difference
η	Viscosity
κ	Thermal diffusivity

λc	Capillary length
v	Kinematic viscosity
ρ	Density
σ	Surface tension
τ	Line tension
δ	Solubility parameter
S	Swelling ratio

Chapter 1 Introduction

Porous polymer films have a tremendous range of applications in the field of filtration, catalysts, sensors, self-cleaning surfaces, cell scaffolds for tissue engineering, drug delivery vehicles, and photonic materials owing to the controlled porous structure, which has large surface areas, low weight, uniform pore size, great adsorption capacity, variable scales and tuneable chemistry. With all these advantages, porous polymer films gained great research interest and the attention on porous polymers is still increasing long with manufacturing research to find ways of preparing suitable materials with scalable and inexpensive, yet reliable, techniques.

This increasing attention in both research and manufacturing led to numerous techniques being developed for producing porous polymer films of different pore sizes and for different applications, for instance, soft lithography, rapid prototyping, direct templating and laser patterning. These techniques are relying on the design and production of a specific template before imprinting, transferring the pattern to the polymers or etching, which give rise to the intrinsic and unavoidable high cost. Once the template is designed and produced, they can be reused repeatedly when producing the same structure. Although there are disadvantages in these techniques of producing porous polymers, it has shown the potential of large-scale production.

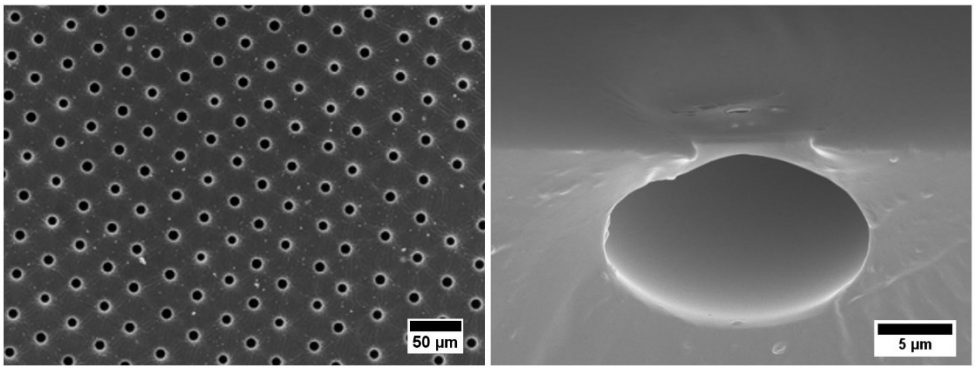

Figure 1.1 Top and cross-section view of the porous polymer made in this research.

Separate to these multiple step methods, a self-organisation method of producing porous polymers was reported in 1994 and attracted great attention in the past two decades. The self-

organisation technique, known as the 'breath figure (BF) method', was reported to self-organise and trap condensed water droplets at a polymer solution surface. Breath figures refer to the droplet patterns formed on cold surfaces, in the BF method as the solvent of the polymer solution evaporates, the temperature at the solution surface decreases and induces the condensation of water droplets, then the droplets self-organise to form hexagonal arrays and finally imprint the shape of the droplets directly into the polymer that remains after solvent evaporation. This direct templating method initiated a one-step approach of producing porous polymer films, which operates at ambient conditions and can be controlled to form a wide range of porous structures regarding size differences and morphology. However, there are significant manufacturing challenges that have prevented this method from reaching the market. Despite the simple templating process, the mechanisms of the growth and self-organisation of the droplets are not fully understood yet. The structure produced by this method is highly sensitive to the relative humidity and air flowrate, which is difficult to control to a sufficient accuracy and can now only be conducted at lab scale in carefully designed environment. Also currently the feasible solvents and materials are not completely explored, and the polymers are limited to certain molecular weights and by the choice of solvents. In the selection of solvents and in the fine-tuning of the morphology of the pores, this breath figure method is quite empirical for each chosen polymer, especially in terms of the conditions required to control the porosity. Also, the solvents used are almost entirely classified as harmful chemicals, and vaporisation process is a significant waste, making up approximately 95% of the original sample.

Nonetheless the innovation in this single-step direct templating method provided a new direction of patterning polymers. In this research, the aim is explore how this approach can be moved closer to a manufacturable process, still using droplets as templates directly deposited onto polymer solutions to produce porous polymers but avoiding the main challenges noted above. As the pore size is a vital determinant for the functionality of the polymer, a more reliable technique of controlling the size of the droplets is also required to be developed. Inkjet technique is one of the most reliable direct deposition techniques for liquids, deposition of very small droplets of controlled volume can be achieved with high accuracy, at high throughput and for a low cost, which is already employed in large scale manufacturing as a method for material delivery. As a maskless and contactless additive manufacturing process, it is being

investigated progressively more as a substitute to lithography and etching to pattern electronics. However, until now, no research on inkjet technique patterning of polymer thin films in conjunction with the BF method has been published. Therefore this research aims at looking for a scalable method of porous polymer production.

This thesis reports a new preparation method of highly ordered porous polymers combining the top-down direct deposition of droplets using inkjet printing technique, and the bottom-up self-organisation of droplets on the polymer surface. In order to develop a more stable and scalable production method, the whole process from drop generation to drop self-organisation needs to be examined. Drop generation from commercially available nozzles were observed with high-speed imaging system to explore the driving signals for single drop printing. By varying the size of the printhead and the waveform, drop size control was examined to try and create monodisperse droplet arrays, which is the fundamental of template generation. The range of behaviours that can occur when printing to liquid surfaces can include creation of defects and as a result, the importance of the printing control through the driving waveform was examined. The impact behaviour for each drop of different size, impact velocity, and viscosity was studied to find the threshold for ensuring reliable patterning. The droplet stability at the substrate/air interface due to the effect of surface tension was then examined, as this is the main parameter to control the process. In the breath figure method the self-organisation is driven by the temperature difference provided by solvent evaporation, therefore heat from the bottom of the container was applied to provide the temperature difference and also drive the packing and self-organisation of the droplets in this case. After examining a number of liquids, Polydimethylsiloxane (PDMS) was patterned with droplets using this new technique. While this polymer cannot be patterned with the traditional breath figure method, it is a useful biocompatible and implantable material. With the cross-linking mechanism, PDMS does not need to use organic solvents, and so a move can be made towards a cross-linking change in viscosity for templating, rather than solvent evaporation. Another advantage of using this new technique is inkjet printing can deliver the materials into the pores directly for in-situ loading, and the dose can be controlled strictly.

In this thesis, a literature review into the BF method of templating polymers including the widely reported mechanisms of self-organisation and growth of droplets is provided in Chapter

2, then the polymers and applications that the BF method can achieve are listed. The inkjet technique mechanisms are also reviewed in this chapter, to analyse the challenges and gaps in these research fields and to get better-defined research questions. In Chapter 3, the research methods and the development and setup of experimental rigs are introduced and materials used. Next, notable results during the research are summarized and discussed in detail in Chapters 4, 5 and 6. Finally, a summarised conclusion and suggestions of promising future research is in the last chapter.

Chapter 2 Background and literature review

2.1 Research background introduction

In 1994, a single-step polymer templating method was developed known as the 'breath figure (BF) method', which is the capture in a polymer film of droplet patterns formed on cold liquid surfaces. This technology is based on the evaporation of volatile solvent solutions containing polymers, providing the temperature difference for water vapour to condense on the surface and also the convection to drive the self-assembly of the droplets to form hexagonal rafts. As the solvents evaporate, the droplets template the remaining entangled polymer. This method then attracted significant attention and has been a focus of research for the past two decades. Research on this method has focused on the developing monodisperse pores, templating different polymers, functionalising polymer surfaces, exploring applications, and scaling up. Due to the strict conditions for BF formation, for example temperature, relative humidity, air flowrate, and solvent choosing, this method of templating polymers is still confined within the lab scale. Inspired by these research activities, this work looked for a scalable method of manufacturing porous polymers with controlled microstructures by using droplets as templates, and took advantage of drop self-organisation to form highly-ordered structures. The key hypothesis is that inkjet printing can be used as a way of introducing droplets in a more reliable and scalable method. For this reason, a review of the field of BF method patterning is required and an introduction of the level of control over inkjet printing is also included.

2.2 Porous polymer films

2.2.1 Introduction

Ordered porous materials have been investigated since 1990s, and have drawn wide attention from the fields of physics, material, and chemistry [1]. Porous polymers are important because they have the advantages of high surface area, distinct porosity [2] and the potential for easy processability by self-organisation [3]. Highly ordered porous polymers with monodisperse sized pores are of great interest to industry for a substantial number of applications in a variety of fields reported [4][5], such as material separation [6], catalyst supports [7], optical devices

[8][9], cell scaffolds for tissue engineering [10][11] and sensors [12]. It still has a huge potential in the way of preparation and in the development of applications.

The pores of solids are classified according to the size. Pore sizes smaller than 2 nm are within the range of micropores, pores sizes from 2 nm to 50 nm are called mesopores, and those above 50 nm are attributed to macropores. Pore morphology, including the pore size and shape, are crucial determinants of the properties of porous polymers films. The narrow size distribution and the uniform shape of the pores is the key advantage often noted in the BF method. For example, a material with uniform micropores, such as a zeolite, can separate molecules on the basis of their size by selectively adsorbing a small molecule from a mixture containing molecules too large to enter its pores. Clearly, a distribution of pore sizes would limit the ability of the solid to separate molecules of differing sizes. Therefore, researchers have made great efforts in controlling the porosity arrangement and narrowing down the size distribution of the pores, and developed number of methods for producing ordered porous polymers.

2.2.2 Methods of producing porous polymers

There are a wide range of approaches to fabricate patterned porous polymer films, such as lithography [13] and direct templating [3].

Soft lithography techniques, which refers to the fabrication of patterns using PDMS stamp [14], was the most commonly used processing method for fabricating structures of 500 nm and larger scales [15]. Soft lithography is still used today for microfabrication (nanofabrication), such as microfluidics and semiconductor production. There are four main steps in soft lithography method: design pattern, fabricate mask, fabricate PDMS stamp and fabricate micro- or nanostructures with the stamp. Compared to direct templating methods, soft lithography requires more procedures of transferring pattern copies several times, and needs the fabrication of the mask and the master, which increased the cost.

Direct templating, also known as hard templating, uses monodisperse particles as the sacrificial materials to produce porous polymers [1]. There are usually three major steps in this method: monomer penetrates into the voids of the monodisperse particles, in situ polymerisation, removal of particles. Silica colloidal particles and polystyrene particles are commonly used as the templates [16][17][18].

In 1994, François *et al*. discovered a simple approach to create a honeycomb morphology of polymer sheets using the self-organisation of water droplets as a template, which then became known as breath figure method [19]. This direct templating method started a one-step approach of making a porous polymer, and it is cheaper than lithographic patterning [4].

2.3 Breath figure method

2.3.1 Breath figure method introduction

Breath figures refer to the water droplet patterns obtained by vapour condensation on cold surfaces, which was first studied by Lord Rayleigh in 1911 [20]. Rayleigh's study of BF on solid surface discovered that the condensed water is in the form of small lenses and it is believed that the number and thickness of the lenses depends on the cleanness of the glass [20]. Making use of the condensation of water vapour on cold surfaces, porous polymer films can produced by dissolving polymers in a highly volatile solvent that is exposed to a high humidity gas flow. According to Figure 2.1 (a), when the solvent evaporates, it will provide the temperature difference for water droplets to condense on the surface; In Figure 2.1 (b), the water droplets condense on the surface and form close packed pattern during their growth; (c) the water droplets sink into the solution of polymer; (d) after the solvent and water evaporate, the imprints of the droplets are left in the polymer film.

In earlier studies about BF on solid surfaces in 1990, it shown that there are three stages of the growth of BF: Initial stage: the droplets are isolated and the surface coverage is low, the droplets radius (R) changes as $(R) \propto t^{1/3}$; Crossover stage: the growth in this stage is characterised by a high surface coverage and drastic increase in the grow rate; Coalescence-dominated stage: the suggested value of high surface coverage constant is 0.55 (on solid substrates), noticeable coalescence of droplets happens in this stage which highly increases the radius of the droplet $(R) \propto t$ [21]. A few years later in 1996, a dynamics of BF formation on volatile liquid surfaces was investigated, which opens a stimulating opportunity to study the relationship between BF formation and fluid properties [22]. During that study two fluids were compared: benzene and chloroform, and to capture BF, about 5% $_{w/w}$ of polystyrene (PS) was added to the fluids. The properties of benzene and chloroform are shown in Table 2.1, they

have comparable values for surface tension, viscosity and enthalpy of vaporisation but significantly different vapour pressures. The same three-step growth was observed, but the development of average diameter for benzene is (D) $\propto t^{0.3}$ at the first stage and (D) $\propto t^{0.95}$ of the third stage, while the order of t is uniform of 0.5 for chloroform reflecting the role of coalescence over the entire time domain [22].

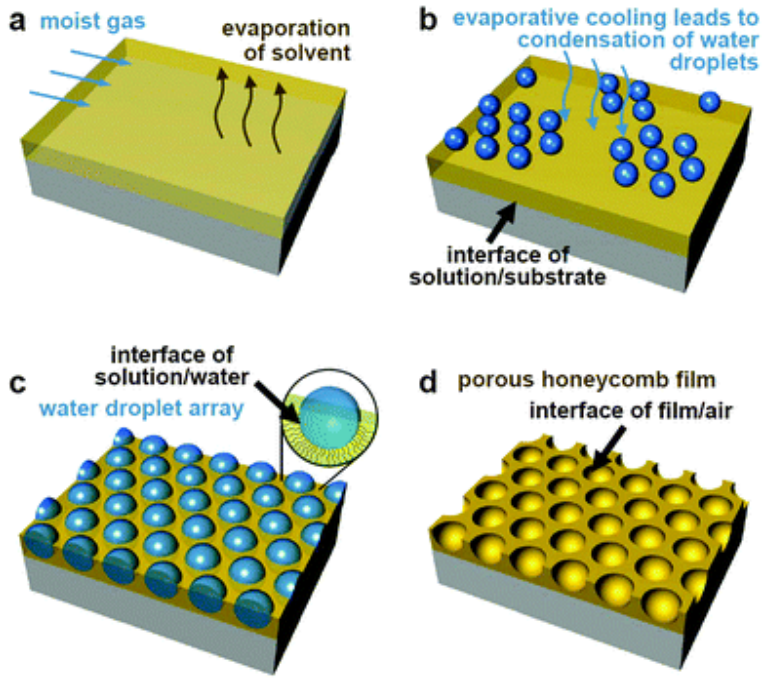

Figure 2.1 Schematic illustration of breath figure array formation on polymer solvents and the capture of imprints [23].

Table 2.1 Physical properties of benzene and chloroform [22].

	Benzene	Chloroform
Density (ρ)	0.88 g/cm^3	1.48 g/cm^3
Surface tension (σ)	28.20 mN/m	26.67 mN/m
Coeff. of viscosity (μ)	0.60 mPa s	0.53 mPa s
Enthalpy of vap. (ΔH_{vap})	33.83 kJ/mol	31.28 kJ/mol
Vapor pressure (P_{vap})	13.8 kPa	28.5 kPa
Expansion coeff. (β)	1.237×10^{-3} K^{-1}	1.273×10^{-3} K^{-1}
Mol. sp. heat (C_p)	136.3 J/mol K	114.2 J/mol K
Thermal conductivity (k)	0.141 W/m K	0.117 W/m K
Molecular wt (M)	78.11	119.38

2.3.2 Breath figure mechanism

Since the first study published by François *et al*. with star-shaped polystyrene (polystyrene-polyparaphenylene [PS-PPP]) of insoluble PPP core surrounded by PS shell in carbon disulphide (CS_2) [19], the fabrication of honeycomb structured polymer films using BF approach has received extensive interest due to the simple, inexpensive [24] and robust mechanism of pattern formation [25].

The mechanism is not understood in detail yet, and there may not be a single general applicable mechanism for BF formation [26]. However, Stenzel *et al*. reported the major affecting factors on the quality of ordering and pore size are relative humidity (RH), airflow and concentration of the polymer [25]. There are two well-developed mechanisms explaining the formation of close-packing arrays in absence of coalescence. The first is based on the thermocapillary effect combined with Marangoni convection [22][27][28]. The model proposes that the presence of surface current plays a role in the formation of breath figure, which is shown in Figure 2.2.

The surface current might not only be caused by the air flow and convection, but also by local variation of superficial tension (Marangoni convection) [19]. Srinivasarao *et al*. reported the thermocapillary effect in breath figure pattern formation [27]. The schematic graph for the formation of porous structure developed by Srinivasarao *et al*. is shown in Figure 2.3. It was stated that the convection current and air flow plays an important role in forming hexagonal arrays. The droplets fail to coalesce due to thermaocapillary convection, as the surface is colder than the droplets due to evaporation and latent heat of condensation, which provides the temperature gradient and causes the convective motion in and between the droplets and the underlying liquid. This lubricating air film suppresses the coalescence of the drops [27]. The key points to note in this mechanism are the role of convection is just to induce flow at the surface, and drops are believed to pack before sinking, with thermocapillary convection giving them a cushion of air until that point. Srinivasarao *et al*. also gave another hypothesis that the evaporating solvent leaving the surface kept the droplets apart, as long as the time of interaction between drops is less than that for vapour to escape the crevice between droplets [27]. For this mechanism it is believed that the droplets are first packed then sink into the solution.

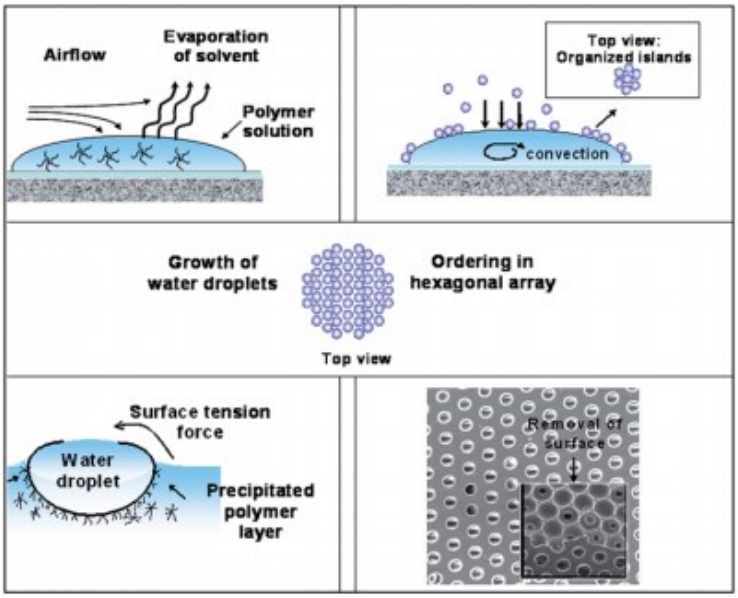

Figure 2.2 Mechanism of formation of honeycomb structured porous polymer films [29].

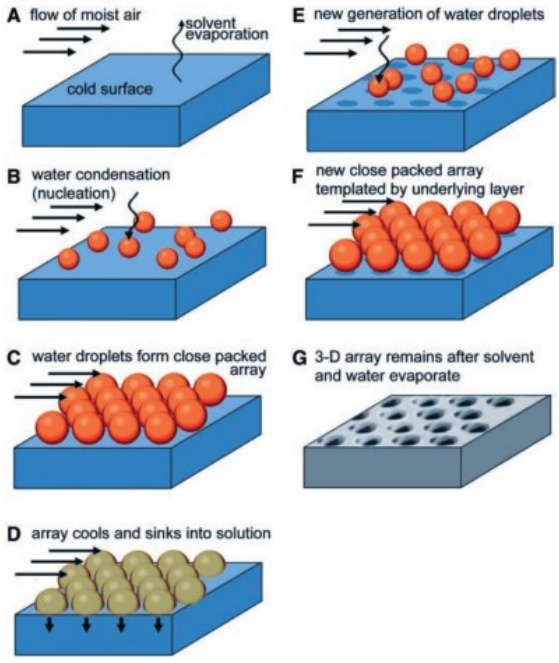

Figure 2.3 A model for the formation of the structure in polymer films. (A) The moist airflow and temperature difference are required. (B) Evaporation of solvent cools the surface and triggers the nucleation and growth of droplets. (C) Due to the convection current arising from the evaporation and airflow across the surface, the water droplets pack into hexagonal array. (D)-(F) Hypothesize that the ordered array sinks into the solution, thus leaving surface of the

solution free for the nucleation and growth of moisture for another array. (G) When all the solvent is evaporated, the film is left with the pores [27].

The second mechanism is proposed by Maruyama *et al* [30]. In this case, it is believed that the Marangoni convection drags droplets from the surface into the solution and sends them to the edge of the evaporating polymer solution, and the droplets pack from the edge inwards like hard spheres. As demonstrated in Figure 2.4, with the evaporation of the solvent, water condenses on the solution surface and with the convection within the solvent they starts to flow to the edge and started to pack from the edge to the centre. This mechanism shows the thought that the drops sink into the substrate first then pack.

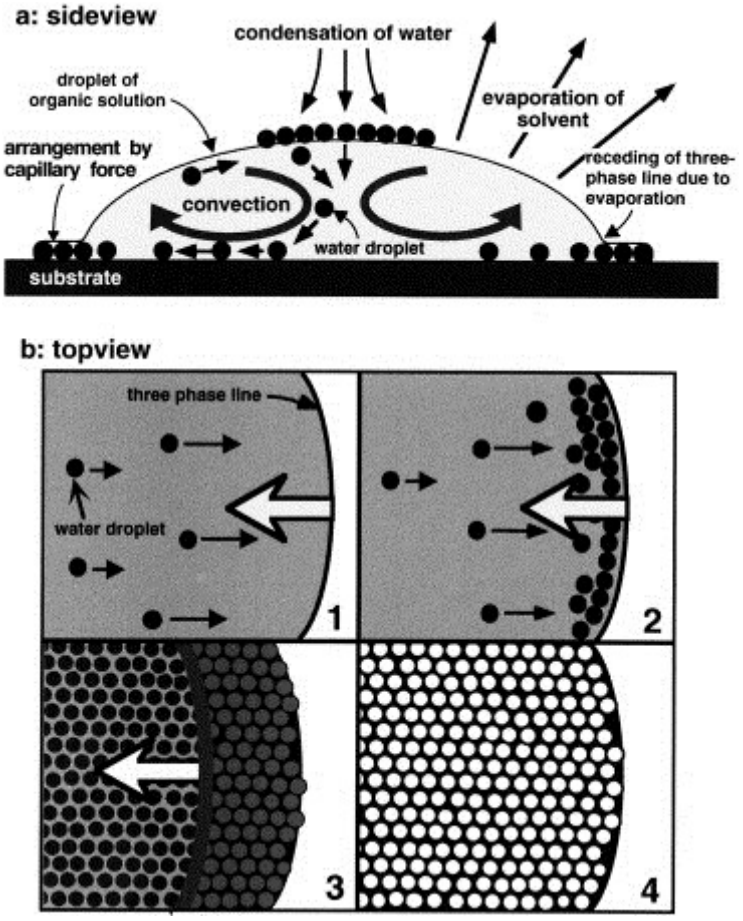

Figure 2.4 Formation mechanism of honeycomb structure under the surface of the polymer solution [30].

2.3.3 Breath figure materials

The choice of polymers and solvents can also affect the quality of the porous film. Initially it was thought that only the star-shaped polystyrene architecture could create the honeycomb structure [19][31][32]. Then the linear polystyrene with carboxyl end groups were proved to be viable to produce ordered honeycomb structures [33]. This indicates the significance of the amphiphilic characters of the polymers in forming honeycomb structure via BF method. Other polymers have since proven successful such as polystyrene-polyfluorene block copolymers [34], polystyrene [35], poly (methyl methacrylate) (PMMA) [36], poly (styrene-butyl acrylate-acrylic acid) [37], cellulose acetate butyrate (CAB) [38] [39], poly(phenylquinoline)-block-polystyrene (PPQ_mPS_n) [40], rod-coil block copolymer poly(2,5-dioctylocy-p-phenylene vinylene)-b-polystyrene ($DOOPPV_{3.2k}$-b-PS_{12k}) [41] and linear carboxylate terminated PS [27]. A tabulated review of results is presented in Table 2.2.

Table 2.2 Researches of different polymers and solutions.

Polymer	Concentration	Comments	Size of pores	Ref.
PS-PPP	2-100 g l^{-1} CS_2	First study Multilayer formed	4 μm	[19][31]
PS	1 % w/w toluene chloroform ($CHCl_3$) carbon disulphide (CS_2) tetrahydrofuran (THF)	Only occurs in toluene and $CHCl_3$ solutions, indicates the effect of solvent is significant	2 μm	[35]
PPQ_mPS_n	0.1-10 mg ml^{-1} CS_2	$PPQ_{10}PS_{300}$ best performance	2 μm	[40]
$DOOPPV_{3.2k}$-b-PS_{12k}	10 mg ml^{-1} CS_2	Photocrosslinking	2-3 μm	[41]

carboxylate terminated PS	1-50 mg ml^{-1} CS_2, benzene, toluene	Faster airflow smaller pore size (linear correlation)	2-3 µm	[27][42]
PMMA	5-30 % $_{w/w}$ sodium dodecylbenzenesulfonate	Irregular porosity	0.004-0.302 µm	[36]
polystyrene-polyfluorene	2 mg ml^{-1} CS_2	After thermal treatment show ordered aggregates π-conjugated blocks in the same position of the cavities formed by water droplets	2.2 µm	[34]
poly (styrene-butyl acrylate-acrylic acid)	5 % $_{w/w}$, 10 % $_{w/w}$ and 20 % $_{w/w}$ silica contents	Drying temperature and colloidal silica particles contribute to the formation of the porous surface	0.187-0.280 µm	[37]
CAB	1.5 % $_{w/w}$ THF and $CHCl_3$	Spin coating of CAB Higher humidity larger pore size Lower rotation speed larger pore size Greater water contents in THF larger pore size	0.25-1.5 µm	[38]
Cyclic polystyrenes	_____	Cyclic polystyrenes are prepared via atom transfer radical polymerization and azide−alkyne	1.28 -2.30 µm	[43]

poly(3-hexylthiophene)-block-poly(methyl methacrylate)	5 mg ml^{-1} CS_2	P3HT-b*-PMMA/NTf_2^- Ionisable clicked diblock copolymers Multiple layers	0.520 μm	[44]

As can be seen from Table 2.2, the size of the pores produced in the PS based polymers are on the order of a few micrometres. When using PS, only experiments in $CHCl_3$ and toluene have been successful and so the solvent chosen is also important in the formation of breath figure structures. There is some evidence showing that the molecular weight of the polymers is affecting the size of the pores [45]. Control of the air flowrate can affect the size of the pores. PMMA shown irregular size and porosity of the final structure. However it was concluded recently that the role of polymers is simply to template the droplets and has very little effect on the packing mechanism [46], but the humidity, air flowrate and the choice of solvent revealed a significant influence on the porosity.

2.3.4 Breath figure humidity

In addition to the polymer and solvent, relative humidity is another fundamental influencing factor. Han *et al.* has carried out the research using PS of different molecular weight (1970k, 223.2k, 29.3k) with a concentration of 1% $_{w/w}$ and four different solvents were used (toluene, chloroform, tetrahydrofuran, carbon disulphide) [35]. Their results reveal a strong linear relationship between the humidity and pore size which is shown in Figure 2.5. Pore size distribution and error bars are not available and so detailed interpretation is not feasible.

Also in research by Kim *et al*., the breath figure pattern produced with CAB in THF shows that the pore size is larger when casting under a higher humidity. As can be seen from Figure 2.6, the film produced under 80% RH has larger pore sizes compared with the 65% RH one. This shows that the size of the pores can be changed by varying relative humidity, nevertheless, the relative humidity is difficult to control precisely, it is usually attempted using nitrogen or air through a flow meter [35] or simply using a breaker with hot water [38]. This is considered as

one of the hindrances which prevent this technique being put into manufacturing, as the control of humidity is difficult and the chamber can only be designed in lab scale.

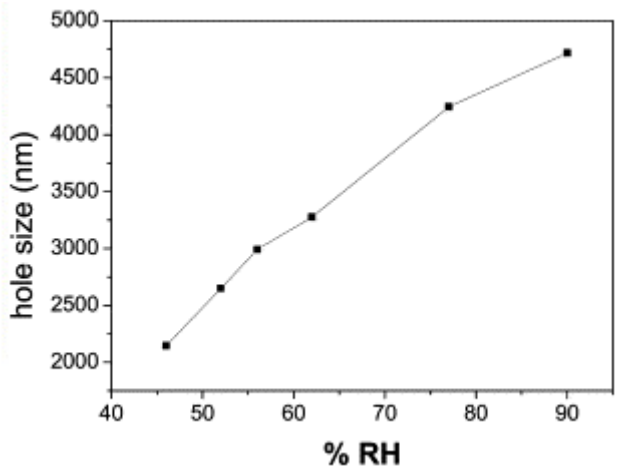

Figure 2.5 The correlation between the relative humidity and the size of the pores [35].

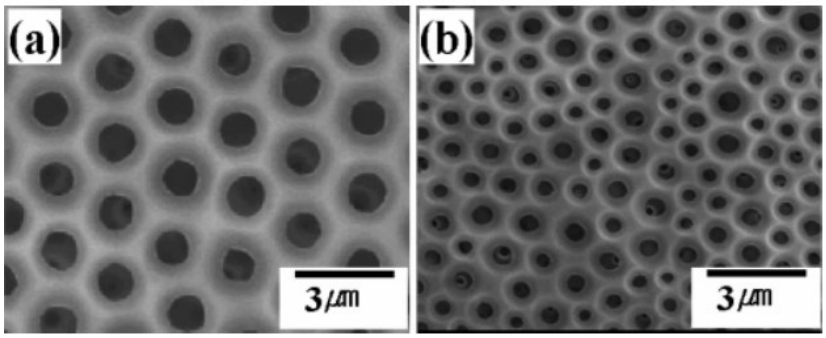

Figure 2.6 SEM images of breath figure patterns prepared by direct evaporation of CAB in THF under (a) 80%; (b) 65% RH [38].

However, research into improvement of the chamber to cast BF method was attractive for better observation of drop growth and more strict control of relative humidity. A custom-made transparent polycarbonate box setup was developed to design an advanced environment enable tracking of BF on polymer surface with improved anti-fogging treatment, and control and study the role of relative humidity in BF formation [47].

2.3.5 Breath figure applications

These porous membranes with highly-ordered porous structures are of interest for use in chemistry and life science. Some of the examples of applications are noted below.

Polymer films produced by BF method cam be used as templates. For instance, Galeotti *et al*. reported the usage of porous liner PS films produced by BF method to produce PDMS stamps to print biological materials [48]. PDMS is poured directly onto the porous sheet produced and peeled off. The schematic diagram of producing the PDMS stamps is shown is Figure 2.7.

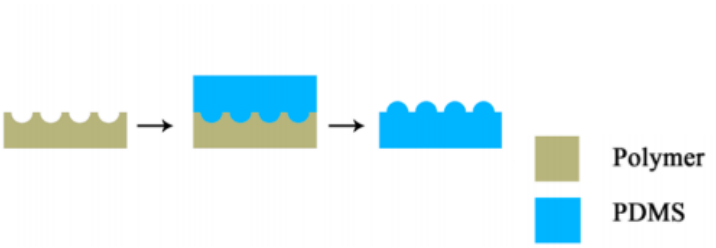

Figure 2.7 Schematic diagram of PDMS stamps produced using porous polymer film as template, adapted from [49]

Functionalised porous polymeric films can be used as sensors. Wan *et al*. used phenylboronic acid (PBA) to functionalise Polystyrene-block-poly (acrylic acid-co-acrylamido-phenylboronic acid) film for glucose sensing [12]. They reported that the PBA groups aggregate on the surface of the pore which promotes the contact between PBA and glucose [12].

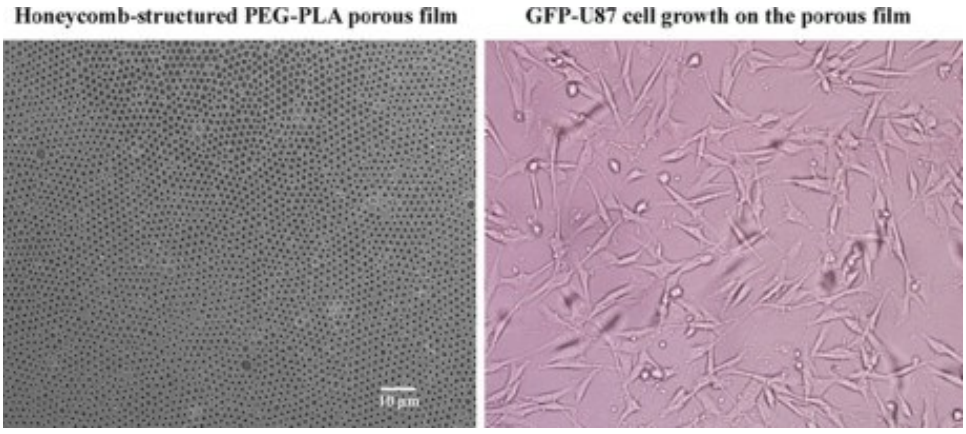

Figure 2.8 Growth of GFP-U87 cell on PEG-PLA porous film produced by BF method [45].

The applications of cell scaffolds attracts increasing attentions in recent years. Shimomura *et al*. and Zhu *et al*. developed a poly (ethylene glycol)-block-poly (lactic acid) (PEG-PLA) porous film which shown the successful growth of GFP-U87 cells in Figure 2.8 [45]. PEG-

PLA is a type of biodegradable polymers, the porous film can also have a potential application in controlled drug delivery [50].

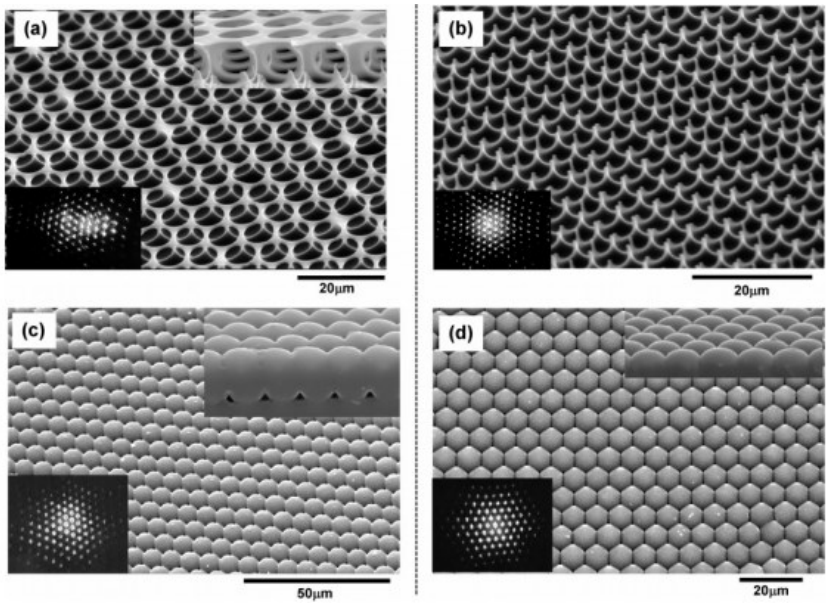

Figure 2.9 SEM images of porous polymer films (a) a honeycomb film (b) pillar structure (c) spherical MLA (d) hemispherical MLA [51]

Microlens arrays (MLA) are an important component of optical telecommunication, displays and solid state lighting [49]. The spherical and hemispherical MLAs produced by moulding a top layer of PDMS onto the BF pattern and peeled off is demonstrated in Figure 2.9. In Figure 2.9, (a) is the original porous film produced (b) is the structure left when the surface of the film is removed (c) (d) is the complementary structure in PDMS. A summary of some of the key applications reviewed are summarised in Table 2.3.

Table 2.3 Applications of BF method produced porous polymeric films

Applications	**Materials**	**Comments**	**Ref.**
		Templates	
PDMS stamps	Linear PS	The moulds of PDMS is used to printed biological molecules, such as DNA and proteins	[48]

In situ polymerization of polymer polyaniline (PAni)	Polycarbonate	Soak BF film in aniline solution for 24h place the film in oxidant solution and polymerise with PAni Produced electrically conductive honeycomb structure	[52]
SiO_2 honeycomb structure	PDMS-b-PS	Cross link PS composition with UV irradiation without destroying the spatial morphology Ceramic micro pattern through mixing precursors	[53]
Optical devices			
Microlens array (MLA)	PS	Projection images from hemispherical MLAs are sharper than those from spherical MLAs	[51]
Separation			
Yeast filtration	polysulfone	Surfactants are important to stabilise water droplets Additive method can cause chemical modification Dip-coating combined with BF	[54]
Cell culture			
Cell adhesion scaffold	PS	Dip-coating and direct casting Adsorption of protein May be applicable to design biomedical surfaces	[11]
Cell adhesion scaffold	PEG-PLA	PEG segments migrated to the water/organic interface	[45]

		Suitable for GFP-U87 cell growth	
Cell adhesion scaffold	Polystyrene-b-polybutadiene-b-polystyrene (SBS)	Photochemical cross-linking Lung cancer cell line A549 Solvent concentration affect structure	[55]

2.3.6 Breath figure development and challenges

To pattern different polymers, the operation conditions can vary dramatically, which makes this method empirical and difficult to scale up into manufacturing [55]. As the BF method is based on the temperature difference between the liquid and the environment to initiate the condensation of water onto liquid surface, the temperature difference is created by the evaporation of the solvent. To provide sufficient temperature difference while enabling polymer dissolution, the solvents used are usually classified as 'harmful', which is not compatible for pharmaceutical or biological applications and is also very challenging and expensive for high throughput industrial scale fabrication. Due to the limited selection of solvents, the polymer that can be patterned using this method is also limited, because only soluble polymers can be patterned. Another challenge is that the pore size depends on a lot of variables such as the solvent's enthalpy of vaporisation, local humidity, air flowrate and polymer molecular weight. Therefore, the size of the pore is difficult to control with this method. In addition, to functionalise the polymers, there are generally complex post-fabrication treatments noted in the literature above. Finally, in BF method the condensed water droplets are used as the templates, therefore the functional groups that can stabilise on the surface of the pores are always hydrophilic.

Recent research was conducted trying to solve these problems with the BF method. The BF method was combined with other techniques such as using the linearly polarised light to post-process the porous structure and reshape the honeycomb pores formed [56]. This combination provides more choice in the design of porosity than the original BF method. Research into simplifying the complex pre-treatment of polymers for functionalisation also shows that it is

feasible to replace the humid air by pumping air through aqueous aniline hydrochloride solution then use the breath figure method, and polystyrene with benzoyl peroxide mixture in chloroform was used as the substrate, finally forming polyaniline functionalised pores [57]. In the BF method, the content of droplets is water and loading of materials into the pore is difficult. An in-situ encapsulate of TiO_2 nanoparticles in the pores formed by breath figure method was reported by adding titanium butoxide onto the polystyrene surface in chloroform solution, then the titanium butoxide react with the water droplets to form TiO_2 [58]. However, there is a significant challenge in using such complex chemical approaches for each required application.

Based on this section of the literature review, this research needs to focus on a direct form of droplet deposition to replace the BF method to pattern different materials. Complimentary liquid drops and surfaces should be explored with suitable surface tension balances and solubility. The self-organisation needs to be explored to find a way of driving packing without rapid evaporation, which is a highly dynamic system and difficult to control. There are different ways to deliver droplets to a substrate directly, such as inkjet printing and spray. Although a continuous production technique of spinning and using glycerol as a template to pattern polymers has been developed [59], the size and pore arrangement cannot be controlled properly. Inkjet is an example of a relatively mature technique with repeatable droplet sizes and easy controllability. Therefore it is chosen as one of the main research techniques. The review will look briefly at this technique in the following section.

2.4 Inkjet printing

2.4.1 Inkjet printing introduction

A lot of techniques fall under the generic title of inkjet, as the most basic feature is the liquid is transported from a nozzle through a gap and delivered to the destination substrate [60]. It has great value for printing as well as the potential to act as a manufacturing element.

Inkjet printing encompasses repeated production of droplets of ink and deposition to the desired location [61]. This technology has been developed over many years. In 1749, Jean-Antoine

Nollet's experiments illustrated the influence of electrostatic forces on drop streams, which is the early experiment investigating the generation and operation of droplets [62].

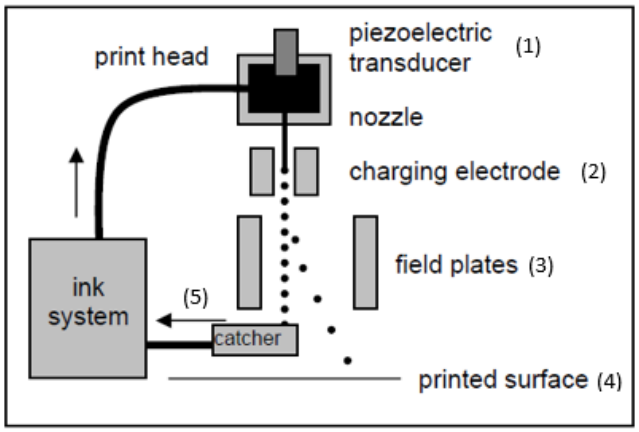

Figure 2.10 Schematic diagram of a continuous inkjet printer, adapted from [62].

There are two main categories of inkjet printing: continuous inkjet (CIJ) and drop-on-demand (DOD). In CIJ, liquid is forced out of the nozzle and due to surface tension the liquid tends to split into several drops. These drops are generated continuously through a constant vibration or pulse delivered to the nozzles, while some of the drops are selected by charging and deflection. As can be seen from Figure 2.10: (1) when the printhead starts to deliver drops, the piezoelectric transducer starts to move and generates lateral oscillation within the liquid stream. As the oscillation travels along the stream, it is amplified and the stream breaks into drops at the end; (2) then the drops are charged by the electrode nearby; (3) when the charged drops pass through the electric field deflection happens; (4) the drops are delivered to the desired location on the substrate; (5) those drops not deviated are collected by a gutter and recycled. Droplets are charged by applying potential on the electrode and an opposite electrical charge can be induced on the surface, therefore the liquid must be conductive.

Compared with CIJ, DOD only generates drops at the required places of deposition, therefore it is largely dependent on an actuation component to push certain amount of liquid out to form the drop and reach the substrate at a desired velocity. Without drop selection and deflection system, DOD system nozzles can be placed closer to the substrate, which gives more positional accuracy. Two major actuation mechanisms are thermal actuation and piezoelectric actuation. Figure 2.11 demonstrated the mechanism of a thermal actuator. When the actuator is triggered

by the printing signal, the heater starts to heat up the liquid inside cause rapid vaporisation of a small amount of ink next to it and the vapour of the ink expands to form a cavity, which pushes the same amount of ink out of the orifice of the nozzle and forms the drop under surface tension.

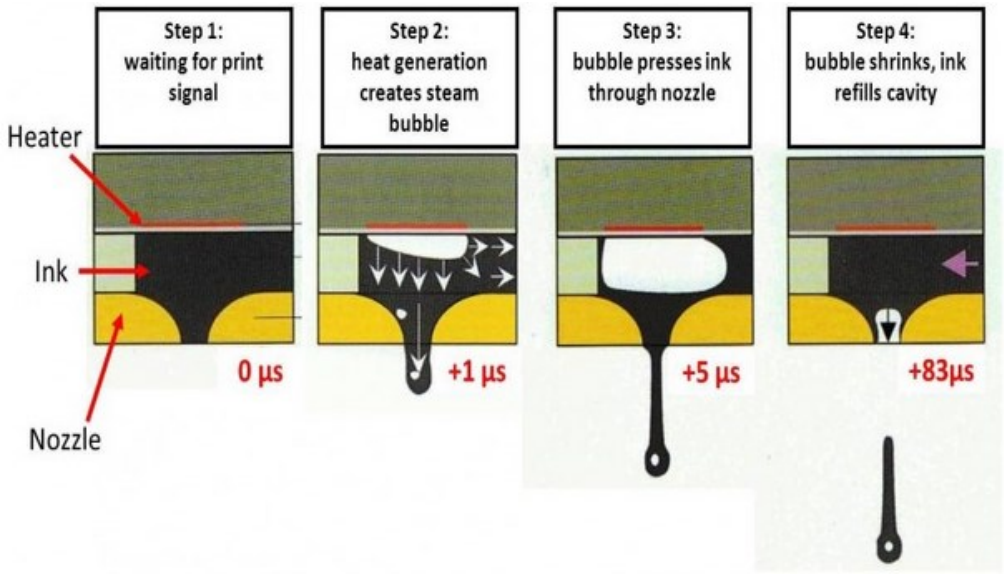

Figure 2.11 The mechanism of thermal actuation; the heater produces the ink vapour to provide energy required for drop formation [63].

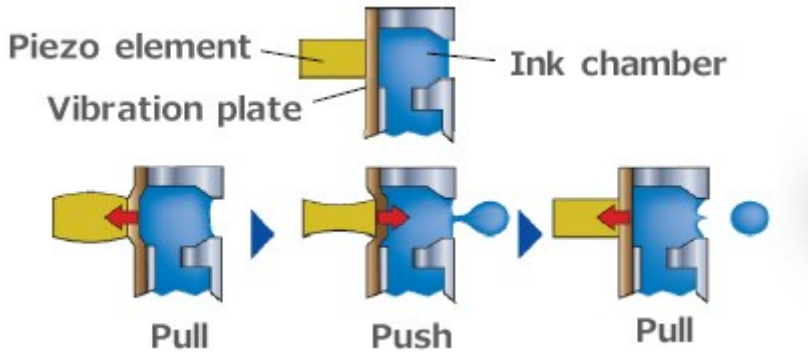

Figure 2.12 The mechanism of piezoelectric actuation; a piezo element is vibrating to provide acoustic energy for drop formation [64].

The piezoelectric actuation based inkjet printheads are similar to the thermal actuated ones, while the heater inside the printhead is replaced by a piezo element (shown in Figure 2.12). It expands to draw more ink into the chamber then pushes certain amount of ink out and forms

the drop. Piezoelectric is the materials' ability to change shape at the presence of electric fields, and depend on the relative orientation of the applied field. Lead zincronate titanate (PZT) is a type of ceramic that has a strong piezoelectric effect when exposed to heat and strong electric field during production, and forms electric dipoles [61]. When an electric field is applied in the same direction, it gives the material a charges, and will expand along that direction and contract in the orthogonal direction.

2.4.2 Inkjet applications

Inkjet can replace a variety of conventional methods of printing in a large number of commercial applications [60]. Castrejón-Pita *et al*. have developed a diagram showing the classification of printing businesses in 2013, which is illustrated in Figure 2.13.

The most well-known application of inkjet printing is the desktop printer. In addition, during the last few decades, it has also been developed for additional applications, such as product coding, large-area graphics, and mailing shots [62]. Most recently, a great number of novel applications have arisen based on inkjet printing, for example, pharmaceutics [65], drug delivery systems [66] [67], electronics [62] [68] and solar cells [69]. Some of the reviewed applications are displayed in Table 2.4.

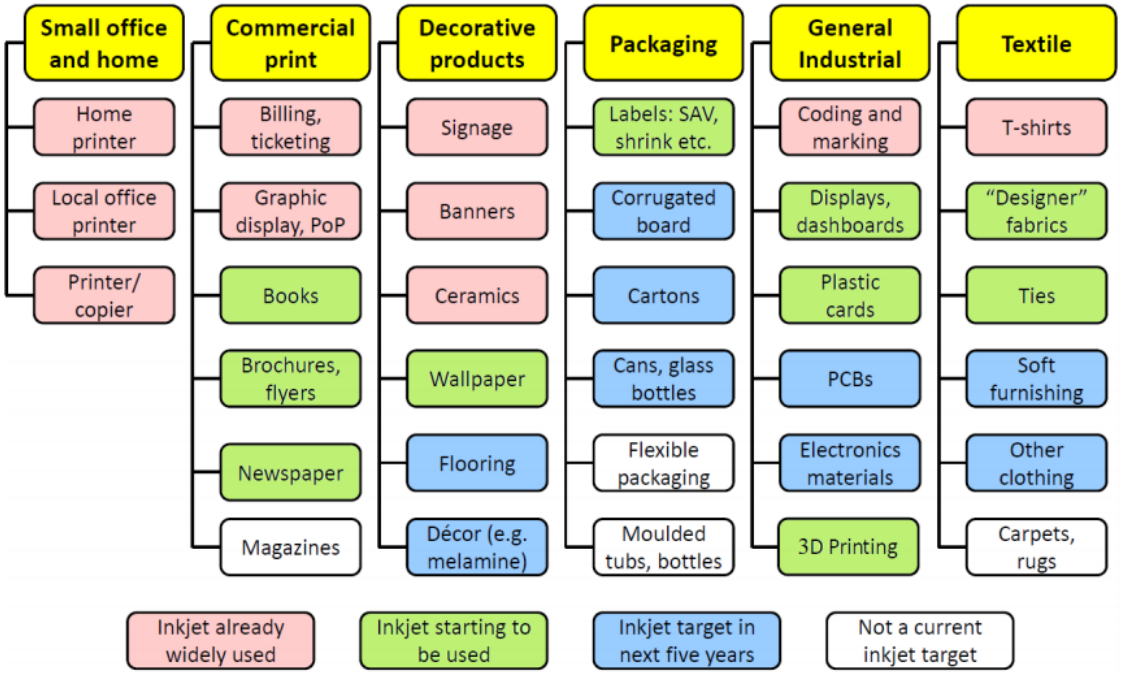

Figure 2.13 The print applications [60]

Table 2.4 Inkjet applications review

Applications	Materials	Technique	Comments	Ref.
Drug carrier	Paclitaxel (PTX)-loaded poly(lactic-co- glycolic acid) (PLGA) inks	Piezoelectric inkjet printer (Dimatix, Santa Clara, CA)	The release rate was dependent on the geometry, mainly the surface area, with a descending rate order of honeycomb > grid, ring > circle Inkjet printing advantages: simplicity, arbitrary geometries, low usage of raw materials, low cost and	[67]

			flexibility in shape change	
Electrochromic devices	Water soluble multi-wall carbon nanotubes in polyaniline printed onto polyethylene terephthalate(PET)	DOD	Potential (voltage) variation lead to colour change	[68]
Medicine formulation	Felodinpine and polyvinyl pyrollidone (PVP) dissolved in ethanol-dimethyl-sulfoxide (DMSO)	Piezo driven dispenser 90 µm orifice	DMSO increase solution boiling point Felodipine-PVP dots produced after the solvent evaporates	[70]
High through put technique	Bovine serum albumin (BSA) printed onto PDMS coated glass slide	Inkjet microchip	On flat surface small region due to poor wetting Surface reaction system Nanoliter droplets Compared to the conventional 96-well microtiter plate, shortened the reaction time necessary for the enzyme-substrate reaction and reduced the sample volume	[71]

Solar cell	photoactive organic materials poly(3-hexylthiophene) (P3HT) and [6,6]-phenyl C61 butyric acid methyl ester (PCBM) of bulk heterojunction (BHJ) organic solar cells (OSC) on transparent indium tin oxide (ITO) coated glass substrates	Fujifilm Dimatix DMP- 2831	Compatibility to various substrates, no-mask patterning solvents, and, reduction in waste products Investigated the impact of P3HT regioregularity on the performance of bulk heterojunction solar High regioregularity P3HT (98%) is not suitable for printing	[72][73]

2.4.3 Inkjet potential and limitations

Compared with CIJ, DOD does not require a complex setup with electrodes and electric fields. It has attracted increasing interest as a novel approach for functional pattern fabrication due to the simple design, low cost and reduced number of steps when compared with traditional photolithography techniques [74] [75]. Owing to these noticeable advantages, DOD has gradually become an extensively used manufacturing and also research tool [68].

Reliability and consistency is the key to all the printing processes [61]. The level of reliability required depends upon the application. Inkjet technique has long been suffering from the formation of a smaller drop which follows the main drop. The smaller drop is called a ‘satellite’. To increase the reliability, several approaches were developed to eliminate satellites, the detailed methods used in this research are discussed in Section 4.2.1. Except for satellites, when the nozzle is not being used, the surface status of the nozzle will change [61]. Another problem with DOD is the drops are not generated continuously, therefore sometimes it may stop printing due to blockage or malfunction of the printhead. However, regular cleaning can help improve the stability. Another failure, termed nozzle-plate flooding, usually occurs at high printing

frequencies and is due to the surplus liquid blocking the nozzle. Recovery is possible by stopping the printing and cleaning [61]. Reliability is also affected by the ability of the printer to start and stop as the dried ink inside the nozzle will change the printing behaviour [60]. Therefore, it is essential to avoid leaving inks inside the nozzle after printing. Hence cleaning is vital for a number of reasons to maintain the reliability of inkjet technique.

2.5 Challenges and research questions

The BF method of templating polymer films operates at ambient conditions and can be controlled to form a wide range of porous structures and surface functionalities. However, there are significant manufacturing challenges that have prevented this from reaching the market. As mentioned earlier, the solvents used are usually harmful, pore size is sensitive to air flow and humidity, which is difficult to control, and the functionalization of the material needs complex treatment. This research tackles these problems by combining top-down techniques for liquid deposition (i.e. inkjet printing) with the same bottom-up self-organisation processes (at micron-scale by ordering drops and nanoscale by encapsulating materials in drops). The research aims firstly, to control and simplify the system to understand the force balances and interfacial phenomena and secondly, to deliver a new, simple and scalable engineering solution to translate this technique to the manufacturing of materials with controlled surface properties. In this research, a DOD piezoelectric actuated inkjet system was chosen as a droplet deposition tool. Compared with the drop growth mentioned in Section 2.3.1, inkjet printing is more reliable in terms of controlling the droplet size and position. Also, for the growth of breath figures, the template is water droplets only, while the contents of the drop can now be anything printable. This should lead to easy modification of the surface of the porous structure. Another reason of using inkjet technique instead of breath figure method to pattern polymer sheets is the solvent used in breath figure method is often harmful and not biocompatible. This is because of the volatility and solubility required. Using inkjet as the deposition technique can solve this problem as a broader set of materials can be employed. Also, it has hoped that the pattern formed by inkjet printing could be designed freely instead of being restricted only to the honeycomb structure produced by BF method.

Research questions arising from the literature review and developed during this research include:

1) Can direct deposition of liquids (inkjet printing) be used to make porous materials?
2) To what extent can the pore morphology and the surface properties be controlled?
3) How can we produce stable monodisperse, stable rafts of droplets suitable for templating by the inkjet printing technique?
4) Can we control the ratio of the opening to the internal diameter of the pores?
5) What is the relationship between drops/substrate properties and the impact behaviours?
6) What are the mechanisms of self-organisation for the droplets deposited on liquid surfaces?
7) Can this new level of control give a better understanding of the self-organisation to switch between different packing modes (for example hexagonal or square arrays), or reduce coalescence/overlap?

Chapter 3 Experimental design

3.1 Experimental design introduction

The research questions were presented in Chapter 2. In order to answer all the research questions, the challenge in this reserach was categorised into five sections, each contributing to the overall goals. As shown in Figure 3.1, the five sections in this research are drop ejection, drop impact, drop stability, drop self-organisation and applications. In this chapter, a brief introduction is provided to these 5 research aspects in terms of the materials used during their analysis, the specific properties of importance, the apparatus used during experimental research and experimental methodology. The details of the most important experimental developments are presented in the remainder of this chapter, while the results from these studies are disscussed in detail in subsequent chapters.

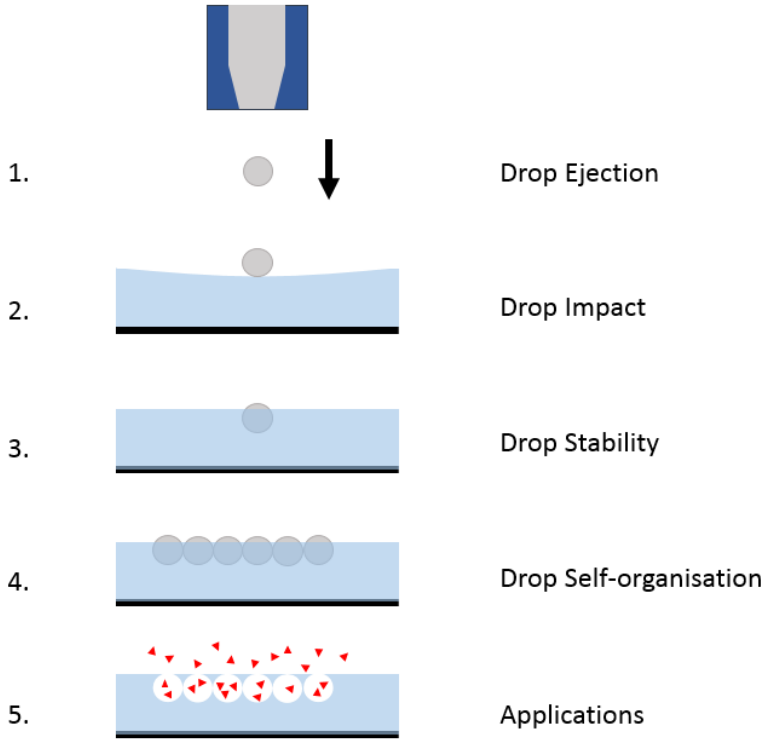

Figure 3.1 Schematic graph of research sections, including drop ejection, drop impact, drop stability, drop self-organisation, and applications.

Drop ejection

This part of the research tackles finding a suitable waveform for printing different materials. This needs to optimise drop generation by observing drop ejection (volume and velocity) and preventing satellites (small drops breaking off from the main printed drop) during printing, thus tackling the first question in research question 2. This also shows the capability of the inkjet printing technique to produce monodisperse droplet templates for polymer templating. Different printing systems were used to test small scale (single nozzle) printing stability, and scaled up multiple-nozzle printing (16 nozzles). This research includes ink formulation, surface tension and viscosity measurements, and waveform design. A home-built imaging system existing in research group that was modified and adapted for the high speed imaging observations. Also there were two additional set-ups purpose-built for this research and two printing research tools that are commercially available (Fisnar robot testing system, Dimatix Materials Printer) was developed and utilized to show printability and a scale-up pathway.

Drop impact

Drop impact research investigates the impact behaviour of droplets of differing properties onto fluid surfaces. Different impact behaviours were observed for droplets landing on different liquids. One of the conspicuous phenomena is the bouncing of droplets back from the surface into the air. Consequently this part of the research aims at finding the underpinning reasons for droplet bouncing with the intention of removing this impact behaviour when printing for applications. This tackles research question 4, as bouncing droplets will cause defects in final products, as missing pores or leading to irregular packing. The drop-on-demand single nozzle high-speed imaging system is used to capture the impact behaviour of each single droplet under different printing conditions.

Drop stability

After droplets are printed and stabilised in the air/substrate interface, surface tension plays a key role in the contact angle for micron scale droplets; and hence determines the porosity and the quality of the final product. This section aims at answering the second question of research question 2 to make a more stable methodology for making a template. Additionally,

considering high throughput printing of droplets onto substrates in large scale manufacturing, drops printed onto the surface may make contact with drops already on the surface. Single drop stability with contact angle measurement as well as two-drop contact behaviours were studied using the drop-on-demand single nozzle high-speed imaging system. The objective is to answer the first question of research question 3 and the second question in research question 1.

Drop self-organisation

According to the results from drop stability studies, spacing between droplets plays a vital role to keep drops separate. As a result, to achieve stable structures (no coalescence) in high throughput printing, drops were printed far apart from each other, and after the whole pattern was printed, convection currents were used to drive droplets to self-organise into diverse patterns. This addresses the first question of research question 1. During this research, it is also found that apart from controlling the contact angle, the final produce could be controlled through tuning of rheological. The rheology and convection studies were conducted to explore research question 5 and 6 with a rheometer, DMP and convection imaging system.

3.2 Experimental rig design

3.2.1 Fisnar robot testing system

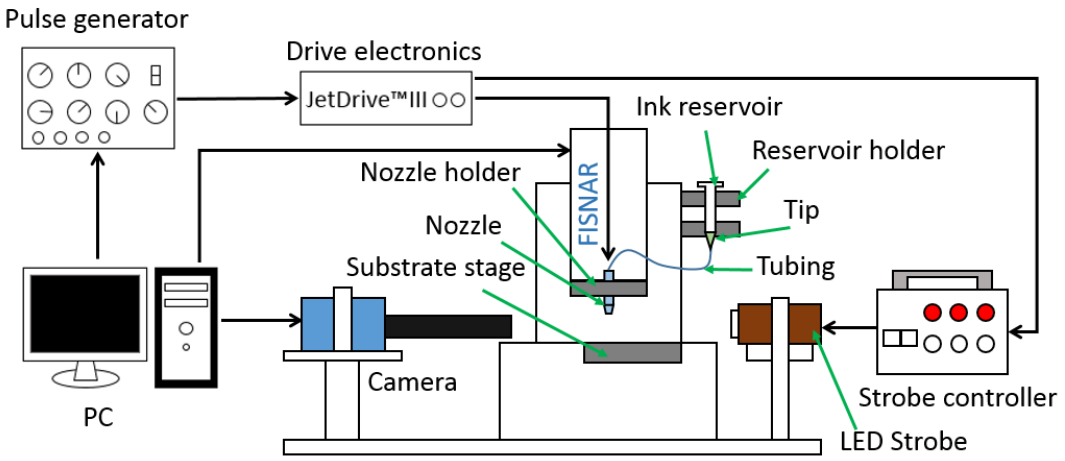

Figure 3.2 Schematic graph of Fisnar robot testing system.

As shown in Figure 3.2, the Fisnar robot based inkjet system was developed specifically for this project for the initial exploration of ink printability, waveform design, observation of drop formation, and pattern programming. The Fisnar robot (F4200N, Fisnar Inc., USA) is a compact benchtop 200 × 200 × 50 mm working area 3-axis (x, y, and z) robot, designed originally for integration with viscous material dispensing applications. The camera (model number: GC1290, Prosilica Inc., Canada) and an LED strobe are used for the observation of drop ejection and the printing waveform design. The software of the camera gives the command to the camera to start capturing at a certain frequency. This signal is also sent to the pulse generator, which can create the specific electrical pulse for the nozzle to print. The drive electronics can generate the predesigned waveform using the PC software and trigger the nozzle to print at a controlled voltage and frequency. The nozzle (MJ-AB-01-80-8MX, serial number B12-80-01 and B12-80-02, both are of 80 μm orifice size, MicroFab, USA) used in this system is similar to the ones used in the drop-on-demand single nozzle high-speed imaging system, just without the metal guards around the glass tube at the printing end. The drive electronics also directs the signal to the LED strobe allowing the flash to be generated at the same frequency as the jetting of the nozzle. As a consequence, the camera images one drop at a time; although the camera is capturing continuously; it is imaging different drops with every frame. The key assumption of this system is the drops are generated in a stable way therefore all the individual drops are identical in terms of jetting performance, for example, diameter and speed. This assumption relies on highly steady printing performance, but nozzles may intermittently malfunction due to disruptive printing, unstable pressure, and printhead fatigue. Stray print and ejection termination is largely on account of particles clogging the nozzle and air bubbles trapped in the nozzle. Pressure variation causes meniscus changes and can lead to print failure as well, thus a pressure regulator is required for the printhead to control the meniscus level. In this system, a barrel (a 5 ml syringe with the plunger removed) is used as the ink reservoir, a fitting tip is connected to the needle hub of the barrel and the specific delivering tubing (C-Flex tubing from Sigma-Aldrich, I.D. × O.D. 1/32 in × 3/32 in, Cole-Parmer Instrument Company, USA) is joining the tip and the nozzle, which is illustrated in Figure 3.2. This reservoir is fixed on a custom-built frame, which is attached to the Fisnar robot, and the relative height of the barrel to the orifice of the nozzle is modifiable. Accordingly, the meniscus in the nozzle is compensated by the gravitational force of the ink in

the reservoir and can be adjusted by altitude elevation. The possibility of status change of the nozzle surface should also be considered when irregular printing happens; this is discussed in detail in the previous chapter and Chapter 4 about the reliability of inkjet printing. While using this observation system, a container and the extraction system replace the substrate stage to catch waste ink. The substrate stage is for patterning, the software for the Fisnar robot helps programming the movement of the robot arm where the nozzle holder is attached and the substrate stage can move continuously. The maximum path speed is 500 mm/s in x and y direction and 200 mm/s in z direction with a resolution of 0.001 mm/axis; also the robot arm can support a point-to-point motion. As the printing of the nozzle and the motion of the robot arm is controlled separately, subsequently the pattern is defined by the movement speed and the printing frequency.

3.2.2 Drop-on-demand single nozzle high-speed imaging system

The drop-on-demand single nozzle high-speed imaging system, illustrated in Figure 3.3 and Figure 3.4, is designed and constructed for drop ejection, drop impact, and drop stability study. This set of rigs were partly adapted and modified from previous research group members. The main components are the imaging system, dispensing system, digital control system, pneumatic control system, and mounting system. The imaging system enables visualisation of the drops and produces the images for data analysis. The dispensing system is responsible for drop generation, providing ink storage and continuous supply. The digital control system regulates the signal flow within the system to stimulate drop ejection and camera imaging. The pneumatic control system is critical in inkjet printing technique, which is utilised for fine-tuning of the pressure, for the purpose of retaining the liquid interface in the nozzle flush. These systems are shown in Figure 3.3, and the elementary components of each system and the connections are revealed in Figure 3.4.

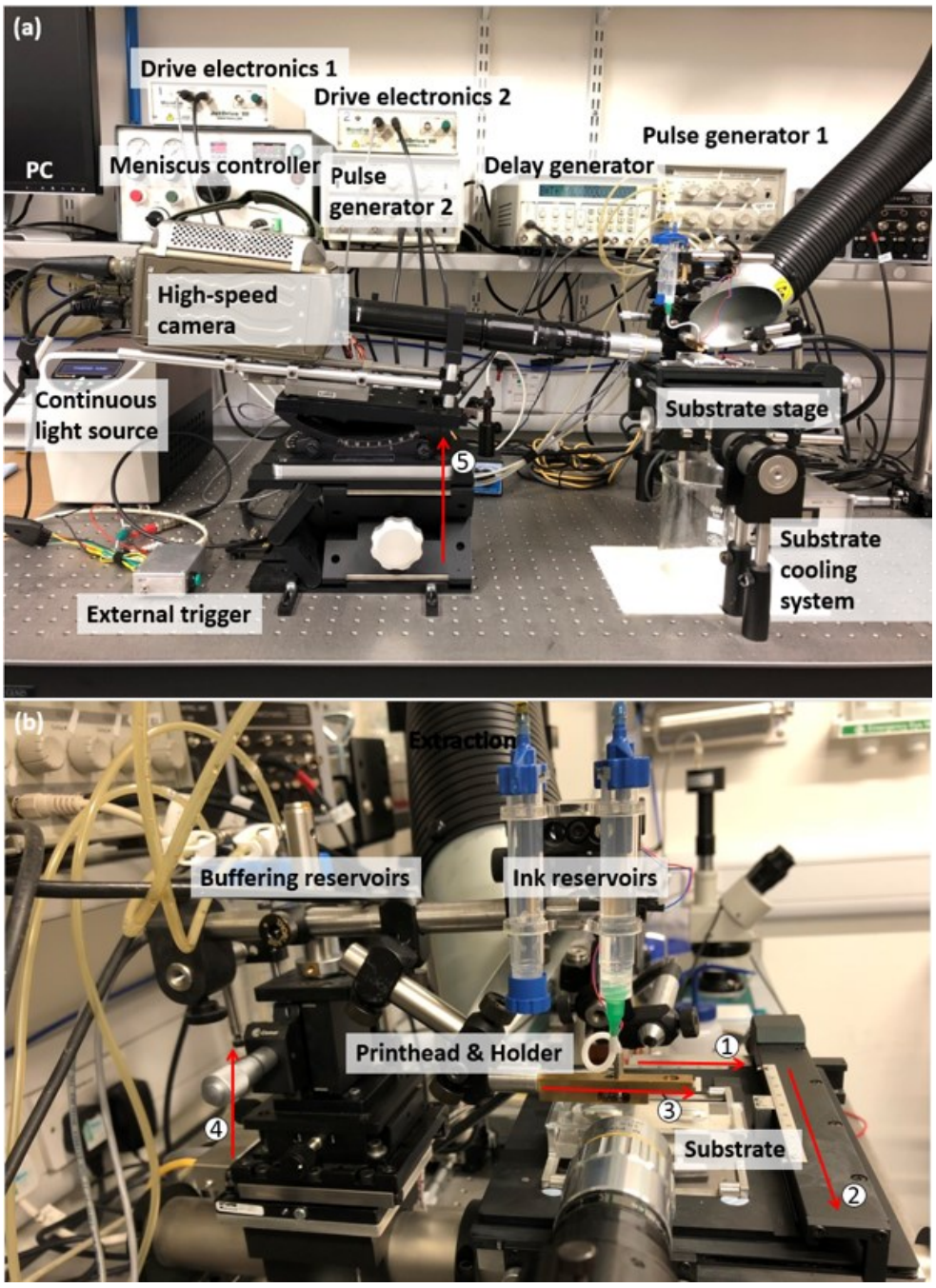

Figure 3.3 Photography of the drop-on-demand single nozzle high-speed imaging system. (a) The overall arrangement of the system (b) Detailed nozzle and substrate stage. Red lines indicate the movements. (1) is the substrate manual movement in x direction. (2) is the substrate in y direction. (3) is the printhead holder controlled by PC software in x direction. (4) is the printhead manual movement in z direction. And (5) is the manually adjustable camera height in z direction.

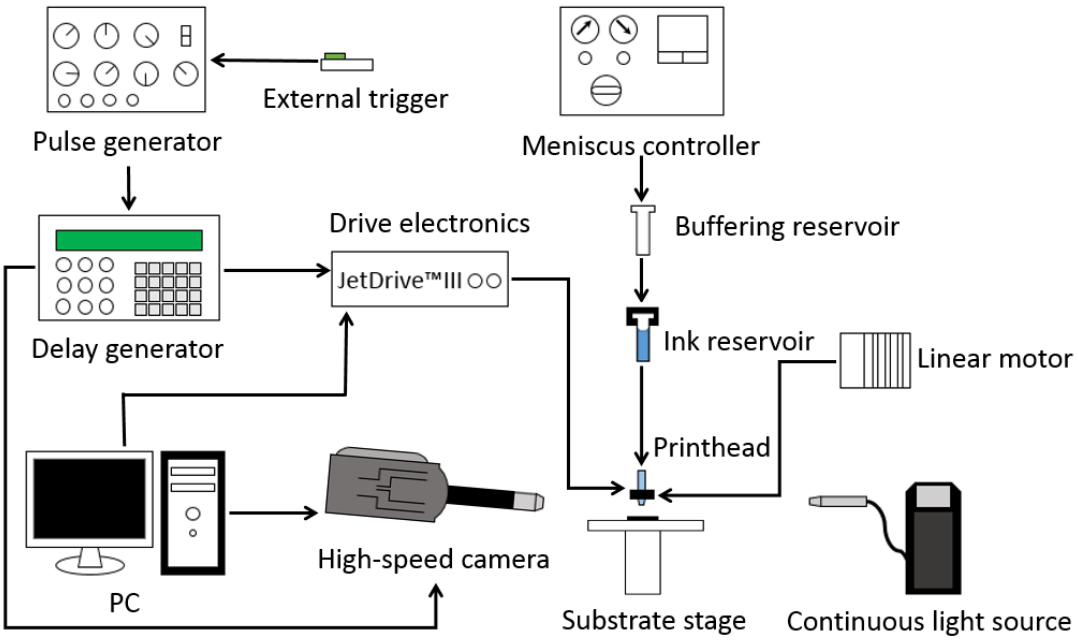

Figure 3.4 Schematic graph of the essential apparatuses of drop-on-demand single nozzle high-speed imaging system and signal flow within the system.

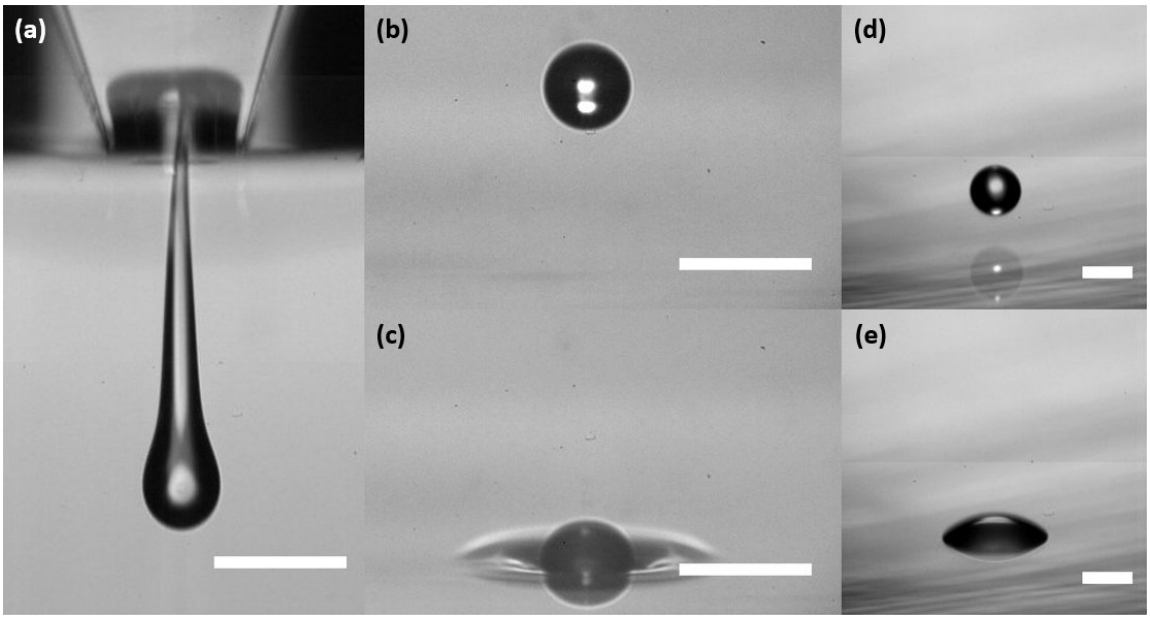

Figure 3.5 Typical images captured by the drop-on-demand single nozzle high-speed imaging system. (a) Drop ejection of 50 % mass fraction glycerol water solution from 80 μm nozzle. (b)-(c) Drop travelling in the air, and impact on octyl acetate surface. (d)-(e) Drop impact on glass slide. Scale bars are all 100 μm.

The imaging system includes a camera (Phantom v7.3 high-speed camera, USA) to capture videos and a high intensity continuous light source (PhotoFluor II, 89 North®, USA) to provide even illumination for image acquisition. The camera has a full frame 4:3 aspect ratio complementary metal oxide semiconductor (CMOS) sensor, composed of 800 × 600 pixels, and can imaging at 6699 frames-per-second (fps, 3 gigapixels-per-second) at full resolution. The maximum imaging speed is 222,222 fps under standard capturing mode. The speed of capturing images is determined by the resolution, there is an upper limit of imaging speed for a fixed resolution, but the speed can be adjusted within this range set by that resolution. Phantom v7.3 also has a high light sensitivity for imaging with a 22 microns pixel size. This camera is attached to a lens coupler (M26 × 36T), and two magnifying lenses Navitar 12 × (Navitar, USA) and M plan Apo 10 × (Mitutoyo, Japan) enable imaging of micron-scale droplets. Figure 3.5 demonstrates the typical images that the Phantom v7.3 can take, the ejection and impact behaviour of droplets is viewable and the contact angle of the droplets can be measured form the images, which paves the way for the research of micron level drop ejection, drop impact and drop stability.

For the same setup, the high-speed camera in Figure 3.3 (a) can switch to a HPV-1 Shimadzu camera (Shimadzu Scientific Instruments, Inc., USA, this camera is supplied by EPSRC), controlled by a specific camera controller, it can record at 1 mfps creating high-definition image at a resolution of 312 × 260 (80000 pixels per image), but only producing 100 frames in one capture. A high power flash (serial number SI-MSFH-500, Specialised Imaging, UK) together with a flash control unit (CU-500, adapt electronics, UK) is as a substitute for PhotoFluor II (the continuous light source in Figure 3.3), which provides extremely intense flash, and the energy is 500 J during 2 ms for HPV-1 Shimadzu camera. This strobe is connected to the delay generator to make certain the camera is capturing within the time of the flash. This ultra-high-speed camera has been used for obtaining some of the results for the drop impact study.

The dispensing system, consists of single piezoelectric nozzles MJ-ABP-01-xxx series (xxx denotes orifice diameter in microns, MicroFab, USA) shown in Figure 3.6, and ink reservoirs (disposable syringe barrel 3cc, Nordson, USA). The connection tubing is the same as the one used in the Fisnar robot testing system. The MicroFab nozzles used to generate droplets are

low temperature dispensing devices, which are compatible with a great variety of materials listed in Table 3.1 under room temperature. For the reservoir, the maximum operating pressure is 100 psi (7.0 kg/cm^3), and the temperature limit is 100 ºF (38 ºC).

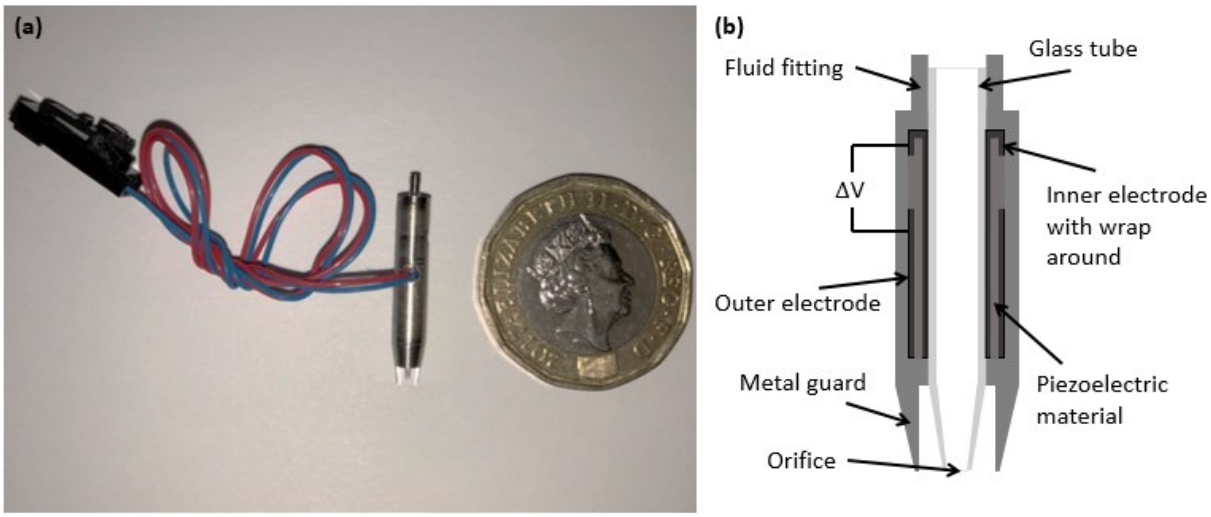

Figure 3.6 MicroFab printhead. (a) Photography of MicroFab nozzle MJ-ABP-80-8MX (serial number B17-88-04, 80 μm sized nozzle). (b) Schematic graph of the inner structure of the nozzle.

Table 3.1 MicroFab nozzles compatible materials [76]

Materials	**Examples**
Organic Solvents	Alcohols, ketones, aliphatics, aromatics, dipolar solvents
Aqueous Buffers	Nucleic acids, proteins, cells
Other Biologicals	Amino acids, lipids, biodegradable polymers
Electronic Materials	Fluxes, photoresists, epoxies, polyimides, electroactive polymers, cyanoacrylates, organometallics
Particle Suspensions	Pigments, latex spheres, metal nanoparticles, Teflon, phosphors, ferrites, zeolites

Other	Sol-gels, thermoplastics, thermosets, acrylics, >1M salt solutions, photographic developer, fuels, aqueous adhesives, odorants

The inner structure of the piezoelectric nozzle is illustrated in Figure 3.6 (b) in detail. The main constituent of the nozzle is a glass tube tapered to a sub-millimetre diameter orifice at one end, and connected to the ink reservoir at the supply end. This glass tube is surrounded by an annular piezoelectric actuator, the actuator has an inner electrode and an outer electrode. The inner electrode wraps around on the outer surface in order to get easy electrical connection. Figure 3.7 reveals the typical waveforms for printing. Figure 3.7 (a) is the simplest 'unipolar' signal that can generate a drop from this nozzle. Figure 3.7 (b) is a 'bipolar' waveform, the asymmetric negative trapezium can reduce the formation of a satellite. The voltage is applied to the inner electrode, while the outer electrode is grounded. When a voltage difference is applied to the nozzle, an electrical field is generated between the inner and outer electrodes initiating radial expansion and axial contraction of the actuator, depending upon the polarity of the voltage applied, and vice versa. More comprehensive descriptions of drop generation with inkjet technique are in Chapter 2 and Chapter 4.

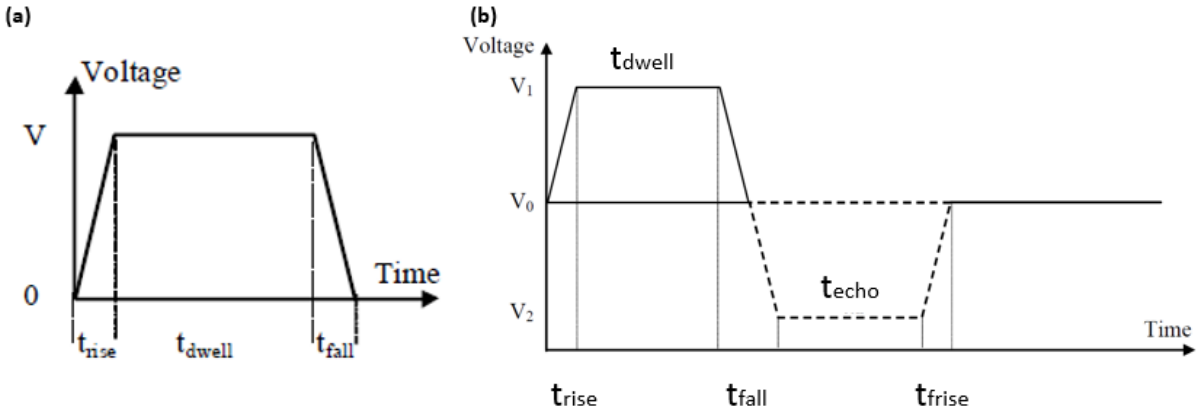

Figure 3.7 Typical electrical signals tailored to the nozzle. (a) Simplest waveform for drop generation. (b) Asymmetric trapezium waveform to minimise satellite. [77]

The digital control system determines two ways of printing, one is the internal trigger via the software the other is the external trigger printing. A PC, delay generator, pulse generator, MicroFab jet driver, and an external trigger constitute a complete control system providing the

specific waveform for drop jetting. The Windows based PC is used to run the software PCC-2.14b (PCC 32-bit) for video capturing, MF JetServer™ software for waveform voltage, shape and printing frequency design, and Easi-V software for nozzle holder positioning. The internal trigger is the MF JetServer™ software (details in Chapter 4), which can define the waveform and start printing directly. Another way to control drop ejection and capturing videos at the same time is to use the external trigger. The external trigger is connected directly to the pulse generator. Then a short pulse is produced allowing simultaneous image capturing. The delay generator separates the signal from the pulse generator, one signal goes to the drive electronics for printing the drop the other is sent to trigger the camera. Usually the non-delayed signal is for printing and the time for camera to start capture is a few hundred microseconds behind, as there is a postponement for the jetting due to the specific waveform and the time required for the drop to travel to the substrate. The function of the drive electronics is to generate the waveform revealed in Figure 3.7 to the nozzle and start printing. This external trigger control system enables capturing complete videos of drop deposition.

The pneumatic control system is a homemade meniscus controller, which is connected with a vacuum pump and compressed air, and its outlet is attached to the reservoir of the ink, controlling the meniscus so it is flush with the orifice of the nozzle. The liquid/air interface position varies because of the surface tension and ink wettability difference; the meniscus may stay inside the glass tube or wet and cover the orifice surface. Both situations may result in jetting cessation as the actuation cannot offer enough energy to move the liquid out of the glass tube or to counter the surface tension of the ink trapped around the orifice surface. Under control mode, the pressure can be manually changed and maintained at the set level. Once turned to the manual mode, purging through the nozzle can be carried out to balance the back pressure to remove clogs in the nozzle. There is an empty buffering reservoir in between the meniscus controller and the ink reservoir to counteract reflux due to strong backpressure to prevent damaging the pump.

The mounting system gives the support for the camera as well as the nozzle, and aligns the imaging system with the nozzle. The camera is fixed on a linear stage (to adjust the focus) on a tiltable stage (± 15º, to adjust the angle of the camera), and the height of the camera can also be adjusted on this stage. The stage is mounted on a breadboard (PBH51513, 1500 × 750 × 60

mm, M6 Taps, Thorlabs, USA) in line with the sample stage, which holds the substrate and the cooling/heating Peltier element. This optical table can help minimise the influence of vibration. On the same breadboard, there is also a mounted linear motor stage (MX80L, Parker Automation, UK), with an attached nozzle holder. The motion is controlled by Easi-V software on PC to get the nozzle to the correct standoff distance to get in line with the camera and the light source, and a linear stage is in position to make the height of the nozzle is adjustable. The substrate stage can be moved in both x and y direction manually within the range of 50 μm in x direction and 70 μm in y direction.

3.2.3 Dimatix Materials Printer (DMP-2800, Fujifilm, USA)

Dimatix Materials Printer (DMP), displayed in Figure 3.8, is a different system from the drop-on-demand single nozzle high-speed imaging system. It is a commercial piece of research equipment using inkjet technology.

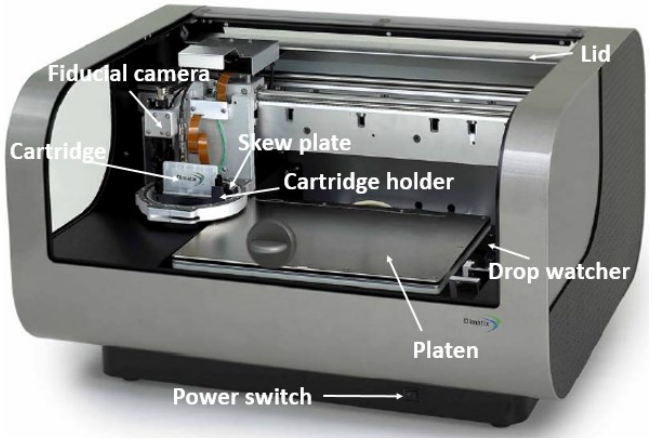

Figure 3.8 Dimatix Materials Printer DMP-2800

DMP uses refillable piezo-based jetting cartridges with a syringe filling system, which can load approximately 1.5 ml liquid each time. The printhead of the cartridge has 16 nozzles in a row at 254 μm spacing, and the size of the drop is about 10 picolitres. DMP is fully controlled on PC using software Dimatix Drop Manager (DDM). Fiducial camera enables tracking the printed patterns, while the drop watcher provides inspection of jetting.

The advantage of using DMP for printing is the pattern can be designed freely with the Pattern Editor function of this printer. The dimensions for the pattern is the total area to print to verify that the total area is no larger than your substrate. In general, printing is required on a single substrate, but it is possible to place several smaller substrates on the platen and jet on all of them at once. The pattern is designed for each line of droplets the starting point, number of drops and the centre-to-centre spacing between each drop. Multiple layers of droplets can be designed and the delay between each layer can also be defined.

Another way of designing the pattern is to import a bitmap file into DDM. Then the BMP image can be converted to the pattern directly. Before importing BMP image, the resolution can be selected and the image is processed into a pattern with this set drop spacing.

3.2.4 Convection imaging system

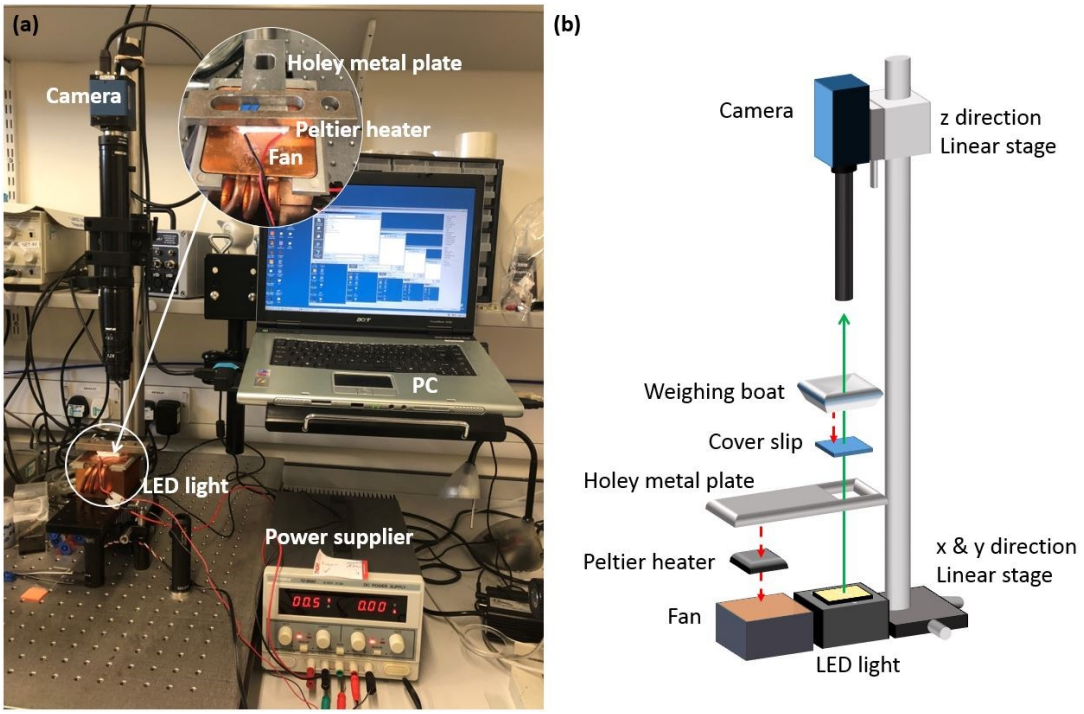

Figure 3.9 Convection imaging system. (a) Photography of convection imaging system. (b) Schematic demonstration of the imaging part of the system.

As noted in Chapter 5, self-organisation is achieved through convection currents. This system was entirely designed and constructed by myself. It was important to find a route to quantifying

the convection, and specifically the flow at the upper surface of the fluid substrate. Figure 3.9 (a) shows the convection imaging system for the convection study. The Prosilica camera (model number: CV1280C, Prosilica Inc., Canada) can capture images at 24 fps on Windows platforms, and it is connected to a PC using software Prosilica Viewer (Prosilica Inc.) to display the view of the camera on the screen. This software cannot capture the video directly, thus VirtualDub (Copyright© 1989-1991 Free Software Foundation, Inc., USA) is set to the screen capture mode to collect the videos of convection. This camera is mounted on a linear stage with a stand to make the camera stable in the vertical direction, and the linear stage can move in z direction to adjust the focus of the camera, which is on the same breadboard (PBH51513) as the Phantom v7.3 high-speed camera. The stand with two linear stages in x and y direction are used to change the position of the camera to target the desired area for capturing convection driven drop self-organisation phenomena. The glass-bottomed weighing boat, holey metal plate, LED light, and the Peltier heater are the main elements of this system. Glass-bottomed weighing boat and holey metal plate are designed specifically for the convection study, allowing the light form the LED to go through so that the camera can focus on the PDMS surface and capture the convection motion. As Figure 3.9 (b) demonstrated, a 10 mm × 10 mm hole is cut out of the weighing boat's bottom, and the cover slip is stuck on the bottom by applying sufficient amount of PDMS (mixed with cross-linker) then put into oven at 80 ºC for 2 h to solidity. The holey metal plate is clung to the Peltier heater with a heat conductive paste, and the Peltier is connected to a power supplier (dual output DC bench power supply 32 V, 3A 72-8690, Tenma, CPC, UK) to heat up the PDMS and activate convection, and it also provide power for the LED light.

3.3 Image processing technique

All of the custom-built set-ups noted above capture images of droplets. It is important to have a reliable method for calculating droplet volume, velocity and contact angle from such images and so image processing is required.

3.3.1 Image acquisition

With these imaging system, data can be collected as videos, either taken by the high-speed camera can be saved as image series using Cine Viewer software (software revision: 2.5.744.0) and convection videos can be processed by VirtualDub. Then the images can be analysed by using the software ImageJ (1.51j8, National Institutes of Health, USA) to extract basic information like diameter and centre position of the droplets. ImageJ gives the best results when processing 8-bit images, therefore images from convection study and microscope images need to convert to 8-bit image first, using the grayscale filter function in VirtualDub software or convert with ImageJ.

As can be seen from Figure 3.10, image (a), (b), (e), and (f) were cropped, the original resolution is 512 × 384 (pixels) , while image (c) and (d) were captured as 256 × 256 (pixels) originally. When capturing video to gain raw images for data analysis, it is always better to get more information in each frame, therefore higher resolution. Nevertheless, as introduced in the drop-on-demand single nozzle high-speed imaging system, owing to the limit of the camera, there is a significant trade-off between high resolution and high imaging speed. For example, image of 512 × 384 (pixels) can be captured at each 66 μs, while the 256 × 256 (pixels) ones has an imaging interval of only 47-48 μs. Thus, for diverse research objectives, the resolution can be altered to find the optimal capturing conditions. The 512 × 384 (pixels) is the most commonly used resolution to attain sufficient level of detail especially for the drop impact behaviour and remain high-speed imaging.

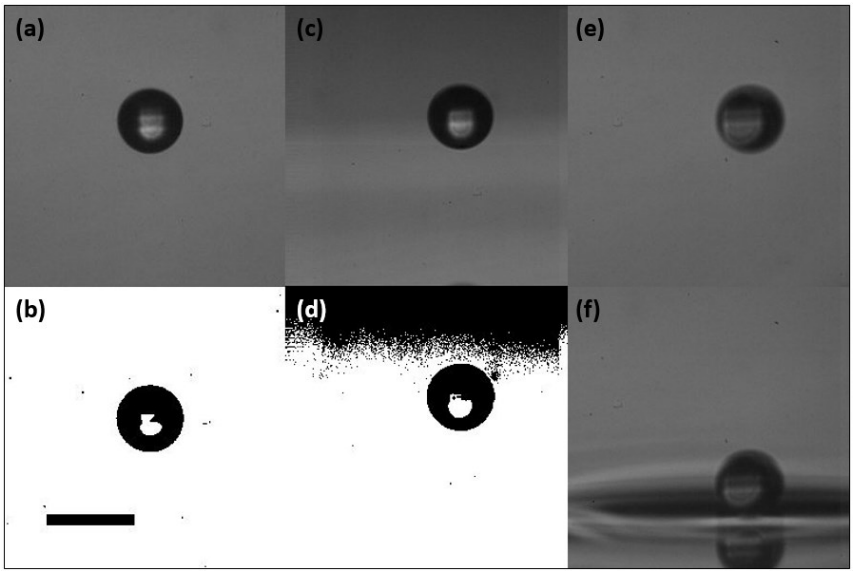

Figure 3.10 Comparison for different illumination and resolution. (a) Fine focused 50 % mass fraction GW drop (b) Threshold method 'Moments' applied to (a). (c) Uneven illumination of a drop. (d) The same threshold method applied to (c). (e) Same drop content but out of focus. (f) The same drop as the one in (e) impact on octyl acetate. Scale bar 100 μm.

To acquire these videos, illumination is inevitable and closely related to the quality of the final images. According to Figure 3.10 (a)-(d), illumination in image (a) is relatively evenly distributed, while thresholding, in image (b) with dark object and bright background is clear. Image (c) appears to be unevenly illuminated, and in segmented image (d) the boundary of the object and the background is difficult to define, which introduces unavoidable errors into the results or even cause failure of particle analysis. Although the noise can be removed by background subtraction with a background image or changing thresholding method, there are still issues with uneven illumination. Hence, it is important to get even illumination for imaging.

Comparing Figure 3.10 (e), (f) and (a), drops in (e) and (f) are out of focus, as a result, there may be errors in the measurements. In addition, the droplet in (e) and (f) is too close to the edge of the image, so that the information of drop impact on the liquid surface, the formation of the ripple, is not complete. Clearly, getting a fine focused object and correct positioning also need to be considered in video capturing.

3.3.2 Scale of images

Calibration is brought into image processing, bridging between the pixels in the images captured by the camera and the real world distance (in microns). The images of a calibration wire (for drop-on-demand single nozzle high-speed imaging system) and a calibration grid (for convection imaging system) were captured at the same magnifications as the videos, which are displayed in Figure 3.11. The width of the calibration wire is 22 μm.

While processing images, first measure the pixels for the calibration wire and grid in the image of the same magnification as the video, then use the 'set scale' function in ImageJ software to set the scale according to the measurement (in pixels/μm) and set to global so that all the images about to process afterwards are set at the same scale. In the meantime, the data of droplet properties output values are changed to μm automatically after the scale is set.

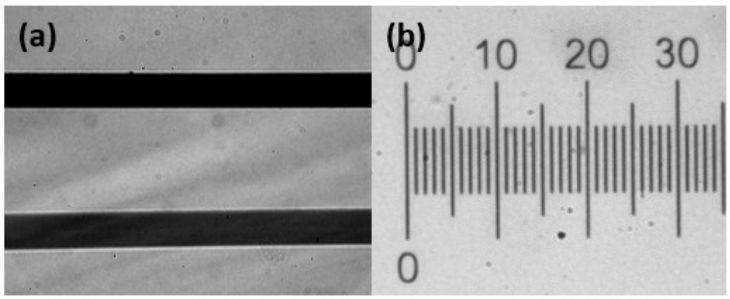

Figure 3.11 Images of (a) Calibration wire fixed on a glass slide for drop-on-demand single nozzle high-speed imaging system, the width of the wire is 22 μm. The upper black stripe is the image of the wire, the lower one is the reflection. (b) Calibration grid for the convection imaging system, shown from 0 μm to 350 μm, the whole calibration grid is 100 × 0.01=1 mm.

3.3.3 Thresholding methods

Thresholding is a technique for image segmentation, usually two classes of pixels, which works by setting a specific cut-off value and the pixels greater than the value are considered one class while the pixels less than this value are in the other class. To measure the size of the drop, threshold is applied to the image, which is demonstrated in Figure 3.10 and in Figure 3.12. In

this case, pixels greater than the set value is turned into the black 'foreground' and the lower ones are changed to the while 'background' for the purpose of particle analysis. Then use the particle analysis plug-in to measure the diameter and to find the centre of the drop, the displacement can be calculated from the centre movement of the drop and the imaging frequency is known, therefore the velocity of the droplet traveling at can be calculated.

While doing thresholding, manual measurement should be avoided, as it provides low reproducibility, high user bias and high intra-/inter- user variability [78]. There are 17 types of Global Auto Thresholds implemented in ImageJ software, which are all completely reproducible. Four examples are given in Figure 3.12 for different thresholding options of one image. It is noticeable that the segmentation of the image varies as different thresholding method is applied. Default and Moments segment this image with clean outline of droplets, while Percentile has more noise around the drop and the Intermodes method cannot provide information for post-processing. In Figure 3.13 a more evenly illuminated image is segmented with all of the 17 methods. According to Figure 3.13, except for Mean, RenyiEntropy, Shanbhag and Yen, all the other methods gave a clear boundary between the background and the droplet. This shows the significance of even illumination.

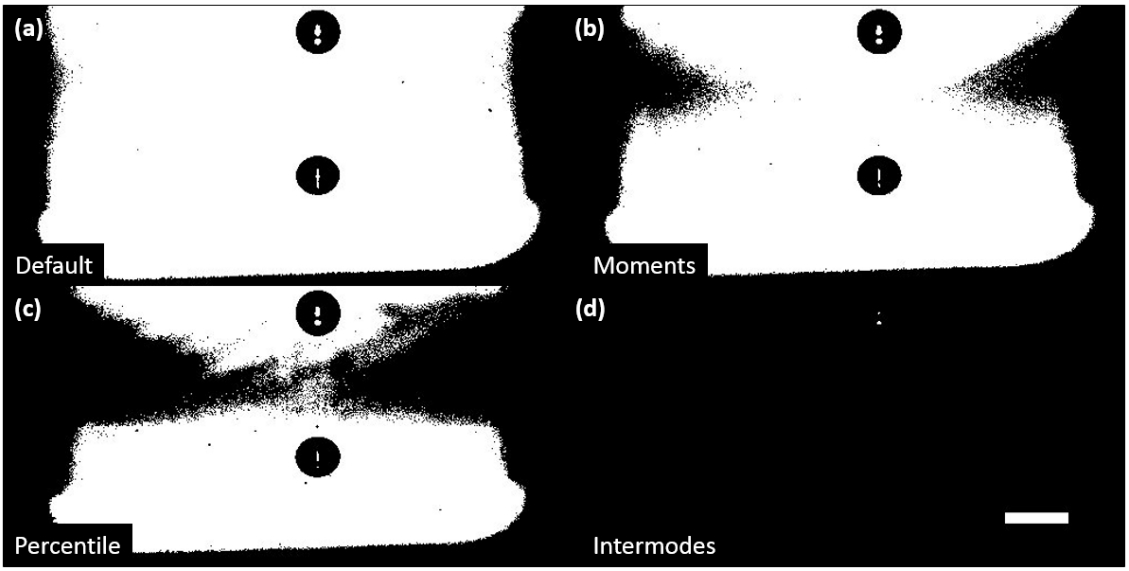

Figure 3.12 Four examples of different threshold options of the same image of drop impact, the drop is 50 % mass fraction water glycerol solution and the substrate is octyl acetate. (a) Default (b) Moments (c) Percentile (d) Intermodes. Scale bar 100 μm.

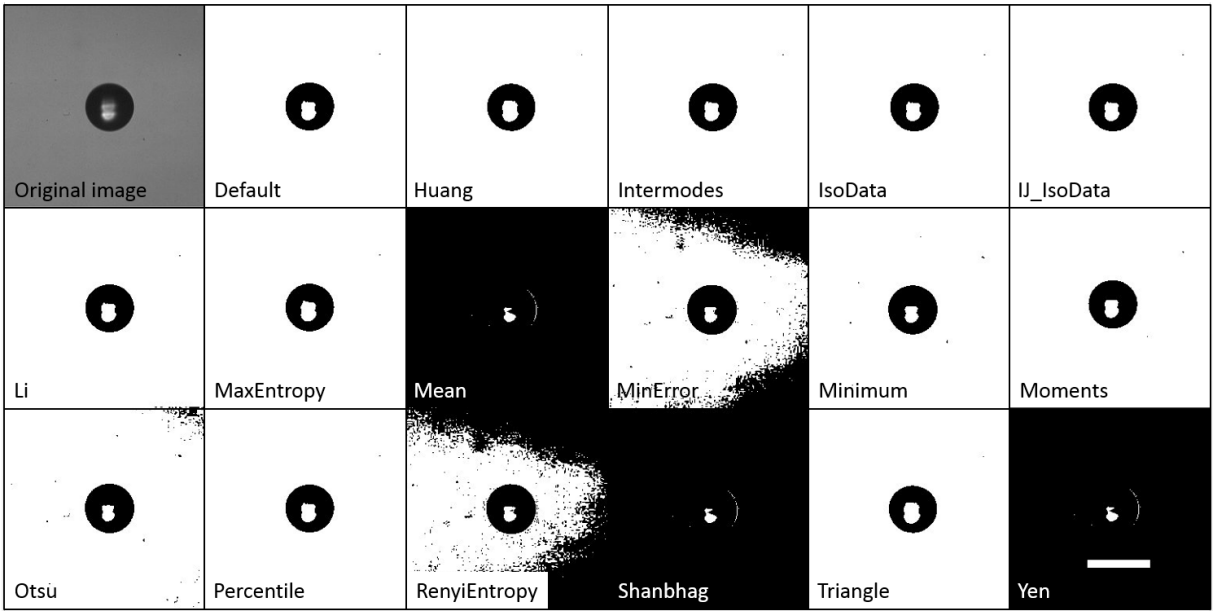

Figure 3.13 All the threshold methods in ImageJ software done to the same drop in the air image. Drop content is 50 % of mass fraction glycerol water solution. Scale bar 100 μm.

3.4 Uncertainties in image processing

Camera limitation

First of all, the frame rate and the capture length of the camera give rise to the inevitable systematic uncertainties. As mentioned earlier in section 3.3.2 the drop-on-demand single nozzle high-speed imaging system, the camera used in this system is a Phantom v7.3 high-speed camera, USA) with a full frame 4:3 aspect ratio CMOS sensor of 800 × 600 pixels, and can imaging at 6699 fps at full resolution. This camera has a significant trade-off between the resolution and the capturing speed. The maximum imaging speed is 222,222 fps, but at the minimum resolution 20 × 20 pixels. It is always optimal to capture as much information as possible, but the speed of video capturing also determines the data that can be extracted from the images. With lower resolution, the information captured is less than high resolution, but a higher capturing speed can capture more details for a changing process especially for impact studies. Therefore the resolution is usually defined as 512 × 384 (pixels) to capture videos at approximately 15000 fps to get optimum capturing, but there is still a limitation of the imaging

speed. The other camera: HPV-1 Shimadzu camera can capture images at 1 μs interval, but the resolution is fixed at 312 × 260 and it can only take 100 frames in one capture. For this camera the only thing can be changed to obtain desired images is the delay. By changing the delay of both the camera imaging and the strobe flashing, the whole process of drop impact can then be captured within the time of flash.

Calibration wire

The calibration wire used is shown in Figure 3.11 (a), which is a 22 μm wire in width. This calibration wire has been used for some previous researches within the group, and the width of the wire was measured by capturing the video of both the wire and the calibration grid under the convection imaging system. The width of the calibration wire measured was 22.667 μm. The variation is negligible for the measurement of drop size, thus the calibration wire is considered as 22 μm. Systematic error for the width change of different part of the calibration wire is assumed to be insignificant compared with the random error from user judgement and measurement bias. The calibration grid was used to determine the random error by repeating measurements, and the final estimated random error is ± 1 %.

Thresholding determination & drop measurement

The uncertainties are introduced in image processing while choosing the thresholding. As discussed in previous section, the thresholding method is chosen by comparing all the methods in ImageJ software. Determining the threshold method, user bias is unavoidable (random error), as long as the method is chosen and applied for one batch of measurement, then it is consistent and easily comparable with other methods. Therefore it is assumed the interpretation difference between each user is negligible for a chosen thresholding method. More uncertainties introduced when using the HPV-1 Shimadzu camera, as the light source is a high power flash, the illumination was different in each image, which led to some difficulties in choosing the thresholding method while processing images.

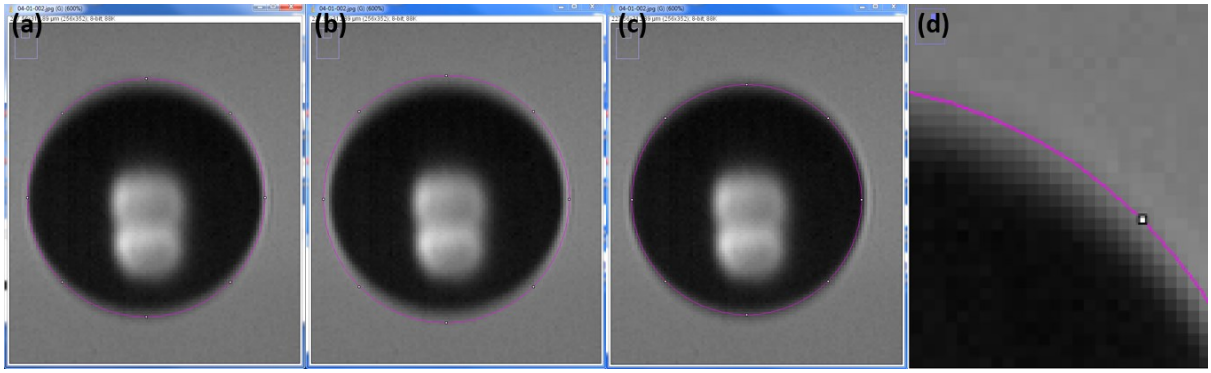

Figure 3.14 Manual drop size measurement. (a) Estimated size. (b) Drop with outline. (c) Drop without fuzziness. (d) Zoomed in image of drop edge. The drop in the image is 72.90 µm ± 2.92 µm.

Additionally, thresholding method itself contains certain level of uncertainties, Due to the limitation of imaging and illumination fuzziness around the drop cannot be fully eradicated. Also the back light makes the outline of the drops brighter than the background, threshold cannot adjust to capture the outline. Therefore the determination of the drop from captured images introduces systematic error as well as random error. According to Figure 3.14 (a), in ImageJ, assuming the drop is a perfect sphere a circle was drawn manually for the best estimated drop, and the diameter of the drop was measured. Comparing this measured drop diameter with the threshold measured value, the difference between these two values is less than 0.001 µm, and as a result, the systematic error from thresholding method is assumed to have no effect on the drop size measurement. Figure 3.14 (d) reveals the fuzziness around the edge of the drop. The random error is estimated by counting in all the outline of the drop and eliminate all of the fuzziness around the drop to find the maximum deviation from best estimation, as shown in Figure 3.14 (b) and (c). The estimated error is approximately ± 3 %.

3.5 Materials

3.5.1 Drop related research

Referring to Figure 3.1 drop related researches are drop ejection, drop impact, drop stability. These researches comprise experiments of inkjet printing of droplets and the image capturing,

therefore different liquid as ink for printing and several substrates were chosen for impact studies. To capture the behaviours of the drop, the drop-on-demand single nozzle high-speed imaging system introduced in section 3.2.2 was the main system for inkjet printing and imaging. Details of methods are covered in each result chapter. Materials used are analytical reagent grade water from Fisher Scientific, and glycerol (99 + %, extra pure from Acros Organics) to prepare glycerol water (GW) solutions of different concentration used for printing. Table 3.2 displays the properties of glycerol water solutions from 20 wt. % to 70 wt. %. The surface tension of the solutions are measured with a bubble pressure tensiometer (SITA pro line t15, SITA, Germany). The viscosity of the solutions are measured with a viscometer (Viscolite 700, Hydramotion, UK).

Table 3.2 Properties of glycerol water solutions

wt. % of glycerol	Viscosity (cP)	Density (g/cm^3)	Surface tension (mN/m)
20	1.7	1.050 (23.5°C)	70.4 (23.3°C)
30	2.2	1.075 (23.5°C)	70.7 (24.0°C)
40	3.6	1.098 (23.3°C)	69.8 (21.1°C)
50	6.3	1.129 (22.9°C)	69.2 (22.7°C)
60	9.5	1.156 (25.9°C)	68.4 (25.9°C)
70	20.4	1.184 (25.1°C)	68.1 (25.1°C)

Density and viscosity of GW solutions are plotted as in Figure 3.15 to show the change correlated to the concentration. According to Figure 3.15 (a), the density of GW solution increased from 1.050 g/cm^3 at 20 % mass fraction to 1.184 g/cm^3 at 70 % mass fraction, and showed a linear relationship between density and concentration. Hence the density can be easily estimated from the graph with other concentrations, also for extreme conditions, the density of glycerol solutions can be considered as the same. Figure 3.15 (b) is the plot of viscosity against concentration, the viscosity of GW solution rise with higher glycerol concentration, also it is manifest that the viscosity ramped drastically from 9.5 cP for 60 % solution to 20.4 cP for 70 % solution. This high viscosity solution is not suitable for inkjet printing therefore GW solutions over 70 % of mass fraction did not prepared. In table 3.2, the surface tension of the solution roughly decreases with concentration increment, thus this series of GW solutions can be considered as viscosity change with surface tension unchanged.

Octyl acetate of 99 + % purchased from Acros Organics is a type of organic solvent, which was used as the substrate in drop impact researches aiming at compare the impact behaviours with PDMS, as organic solvents are mostly used in BF method for dissolving polymers and providing temperature difference. The surface tension of octyl acetate measured with the tensiometer is 26.8 mN/m, and the viscosity is 1.3 cP.

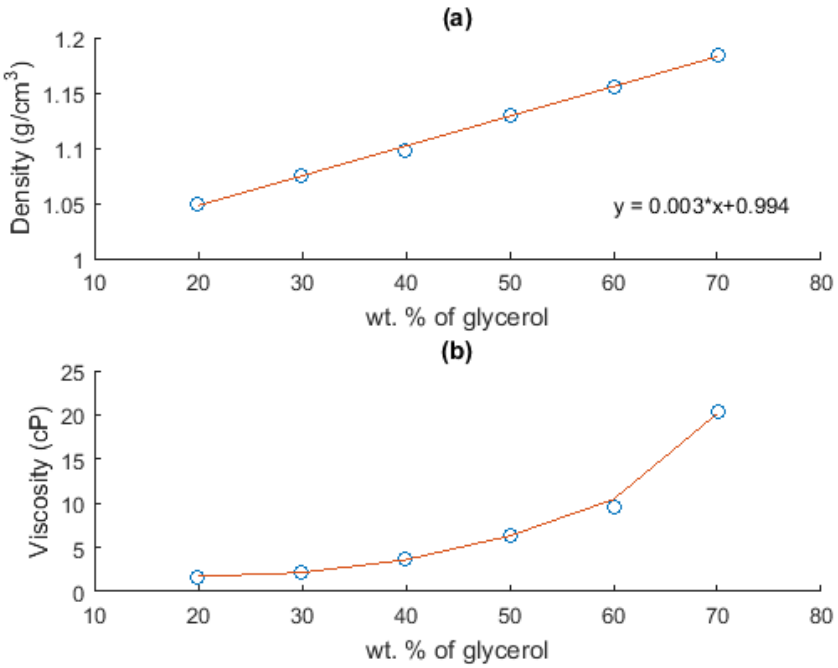

Figure 3.15 Plot of glycerol/water solution density and viscosity. (a) Density in g/cm^3 against increasing mass fraction of glycerol with a linear fit equation R^2 value is 0.9984. (b) Viscosity in centipoise against increasing mass fraction of glycerol.

3.5.2 Patterning related research

Expect for droplets researches to understand the fundamental theory, the final objective is the utilisation of inkjet printing technique to produce porous polymers, therefore the studies on drop self-organisation and drop capture were also conducted. In these researches different polymers were used, especially PDMS is the main focus to do the patterning. The PDMS used in this research is the Sylgard® 184 silicone elastomer kit from Dow Corning. This kit consist of two parts of liquids, one is the elastomer base the other is the curing agent. The elastomer base is the clear PDMS, after mixed thoroughly with the curing agent, it can cures to a flexible elastomer, and the applications are introduced in Chapter 2. PDMS is flowable under room temperature, but highly viscous. The viscosity of the base is 5100 cP (5.1 Pa·s), after mixed with the curing agent at 10 to 1 ratio, the viscosity loweres to 3500 cP (3.5 Pa·s). The surface tension is approximately 19 mN/m. Once mixed PDMS starts to cross-link, this product allows

room temperature and heat cure. Under 25 °C, the curing time is 25 h. Heat curing time depends on the temperature, 2 h at 80 °C, 35 min at 100 °C, 20 min at 125 °C, and 10 min at 150 °C. PDMS cures faster at higher temperature, but when patterning PDMS, the convection drives the self-organisation of droplets on the surface, with too high the temperature, the drastic convection could drag the droplets into the liquid and form multiple layers, in the case of making single layer porous structure, 80 °C is chosen for PDMS curing, also in some biological applications room temperature curing is necessary. DMP was used for print patterned droplets onto PDMS. The observation of the samples were done by using the Olympus BX51 microscope in IfM building and the Nanoscience building in Cambridge. The SEM images were taken by using the ZEISS scanning electron microscope (SEM) in the Nanoscience building. With all these experimental apparatus and the methods described in this chapter, the research was conducted, and the results and findings of this project will be discussed in the following chapters.

Chapter 4 Single drop generation, impact behaviour and stability

4.1 Single drop generation, impact behaviour and stability introduction

As a first step towards replacing condensation of water droplets with direct deposition, it is important to study the generation, impact and stability of these micro-scale droplets at a solution/air interface. As this approach has not previously been attempted in the literature, the goal of the research is twofold, firstly to build a knowledge base about the behaviour of drop-solution interactions and secondly to deliver evidence as to its repeatability and therefore suitability to replace condensation in this porous polymer fabrication technique.

Prior to this impact and stability analysis, the first step is to provide confidence in the ability to deliver a controlled droplet volume and velocity at a sufficient print frequency. As noted in Chapter 2, small droplets that break off the main drop are known as satellites. These are common in industrial inkjet printing and have varying levels of importance on the final product. For example, in Continuous Inkjet Printing, there are small satellite drops that can form a mist. This can be problematic as it can cause a build-up of material within the printhead. In Drop-on-demand (DOD) printing, the satellite may recombine with the main droplet on the surface if the speeds are compatible and the direction is not too affected by the local aerodynamics. Also in DOD printing, small satellites may be acceptable for graphical applications, where the eye does not see such defects. However, for a detailed analysis of drop impact single drops of a tuneable size and velocity are important to achieve.

As shown in Chapter 2, with precise regulation of humidity and air flowrate, with the BF method it is feasible to generate condensed droplets of the same size and they are capable to close pack into hexagonal raft, finally forming highly repeatable pores over the polymer surface. Different sizes of the droplets can initiate irregular pattern of packing, as illustrated in Figure 4.1, this is the simulation result from a study of convective self-organisation [1], and it is noticeable that the particles cannot pack closely with two sizes. In Chapter 2, Figure 2.6 also raised the challenge in achieving well-ordered porous structures caused by polydispersity and

so failure in self-organisation. Hence, aiming at acquiring ordered porous structures with simplified operation and extra rigorous quality control, this research takes advantage of the inkjet printing technique to generate monodisperse droplets that can be used as templates for self-assembly of hexagonal close packed patterns, as well as precise regulation of the dose of deposition.

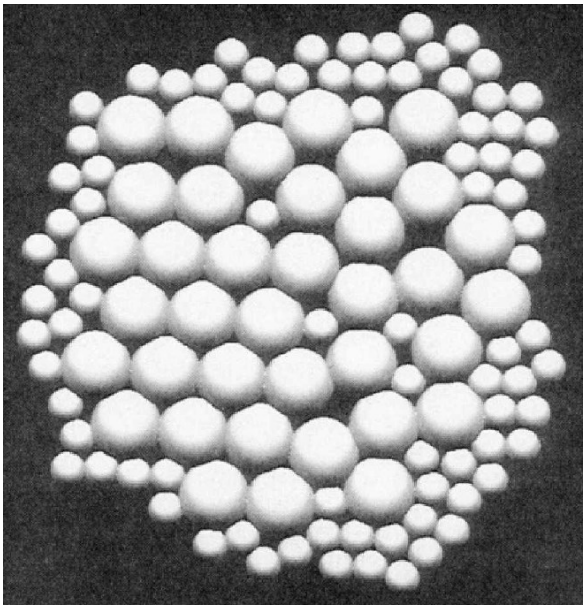

Figure 4.1 Simulation for packing of drops of two different sizes (Rsmall/Rlarge = 0.5) [79].

In this chapter, as introduced in Chapter 3, single droplet generation was investigated using the DOD MicroFab single nozzle with the high-speed imaging system to capture the video of drop generation, followed by image processing. When significant areas of patterning were required, the stability of drop generation with the FujiFilm Dimatix Materials Printer (DMP) was studied. Specifically, drop size and drop velocity were studied under different printing conditions (different ink, different voltage, and different sized nozzle). The waveforms of single droplet printing developed for MicroFab nozzles is displayed in Section 4.2. As a one-step direct templating technique, the goal will be to deliver the droplets to the surface of a polymer solution. The experiments observe the impact behaviour of a single drop on the polymer solution. To enable a close comparison with the BF method, droplets were printed onto an organic solvent with similar properties to those used throughout the BF literature (octyl

acetate). To explore further the opportunities of cross-linking the polymer rather than capturing droplets through polymer entanglement, the experiments include printing to PDMS. Results of drop impact behaviours on different substrates are discussed in section 4.3 regarding ink viscosity, surface tension, drop size, different substrates and in terms of the dimensionless numbers involved. Finally, after this drop printing is fully validated, the positioning of where the droplets stabilise with regard to the solution surface is discussed to provide a more reliable fabrication of the final material.

4.2 Drop ejection

4.2.1 Drop ejection introduction

In the BF method, the drop templates are formed by random condensation. As noted above, when replacing condensation by inkjet printing, the stability of inkjet printing needs to be tested. For inkjet printing, as noted in Chapter 3, it is vital to identify the correct waveform to get the material to print reliably at the required frequency. For Newtonian inks, two physical properties of the ink: surface tension and viscosity, determine the behaviour of the drops printed and hence the required waveform. As we are depositing micron-scale drops onto a liquid surface, which is very rarely examined in the literature, the size and velocity of the droplets will also be important parameters. The test fluid printed throughout this thesis is water mixed with glycerol. As introduced in Chapter 3, glycerol water (GW) solutions are very useful for maintaining similar surface tension values as with standard water-based inks, while enabling the viscosity to be tuned. This water-based ink is also an important model for biological applications. The printing stability of this ink was tested and revealed in the following section.

MicroFab single nozzle printheads are the main tools used to examine how the drops are generated. GW solutions introduced in Chapter 3 were used to explore the printing performance with a range of nozzle sizes, to enable generation of drops of different sizes and velocities. Also, larger nozzles enable higher viscosity inks to be printed. Understanding the printing behaviour is extremely important for the control of drop impact behaviour, also for this inkjet-aided system of porous polymer production. The DMP system was used for the generation of monodispersed arrays of droplets. Both systems are examined in the next section in terms of the theory of droplet generation, to validate the behaviours observed.

4.2.2 Drop ejection: formulation and validation of behaviour

While the general theory of inkjet printing is introduced in Chapter 2, the specific details of drop ejection with MicroFab nozzles is introduced here in detail, as the key technique used for the fundamental analysis of liquid-liquid interactions throughout the thesis. The MicroFab nozzle MJ-ABP-01-xxx series structure is shown in Figure 3.6 and the main components are the capillary, inner electrode, outer electrode, and piezoelectric material. A typical waveform applied to the nozzle is shown in Figure 3.7. This is the simplest waveform that can generate a drop, referred to as a positive trapezium. The amplitude of the 'dwell' is generally understood to govern the velocity of the drop and the duration of the 'dwell' is responsible for the size of the drop [80][81]. The detachment of the drop from the nozzle is dominated by the following 'echo' [82]. The change in voltage will trigger the pressure variation of the liquid inside the capillary. During the rise time, the voltage ramps up from resting status to a maximum value, and this change of voltage from low to high level causes the inner surface of the capillary to expand outward, therefore providing a low pressure (lower than resting pressure) inside the capillary. The negative pressure starts to propagate at the speed of sound to both ends of the glass tube. At the supply end the wave reflects back as a positive pressure wave (higher pressure than resting pressure). After the rise time, is the dwell time where the voltage keeps at high level for a chosen period of time, where the whole structure of the nozzle is steady (no compression or expansion). This allows the reflected positive pressure wave to travel to the middle of the capillary when the fall time starts. Then follows the fall time, in reverse to the rise time, the structure compresses during the decline of the voltage. This inward motion of the capillary reinforces the reflected positive pressure wave, which reduces the voltage required for printing and also maximise the velocity of the drop generated. As this positive pressure wave moves to the orifice end of the nozzle, the acoustic energy is converted into kinetic energy under the impedance mismatch (constant pressure boundary condition), which initiates the emerging of drop from the orifice. Finally, when another negative pressure wave reaches the orifice, fluid starts to pull back. A sequence of images captured of a single drop are shown in Figure 4.2. Figure 4.2 (b) is at the stage where the fluid starts to pull back and then it breaks into a single drop, as shown in Figure 4.2 (c).

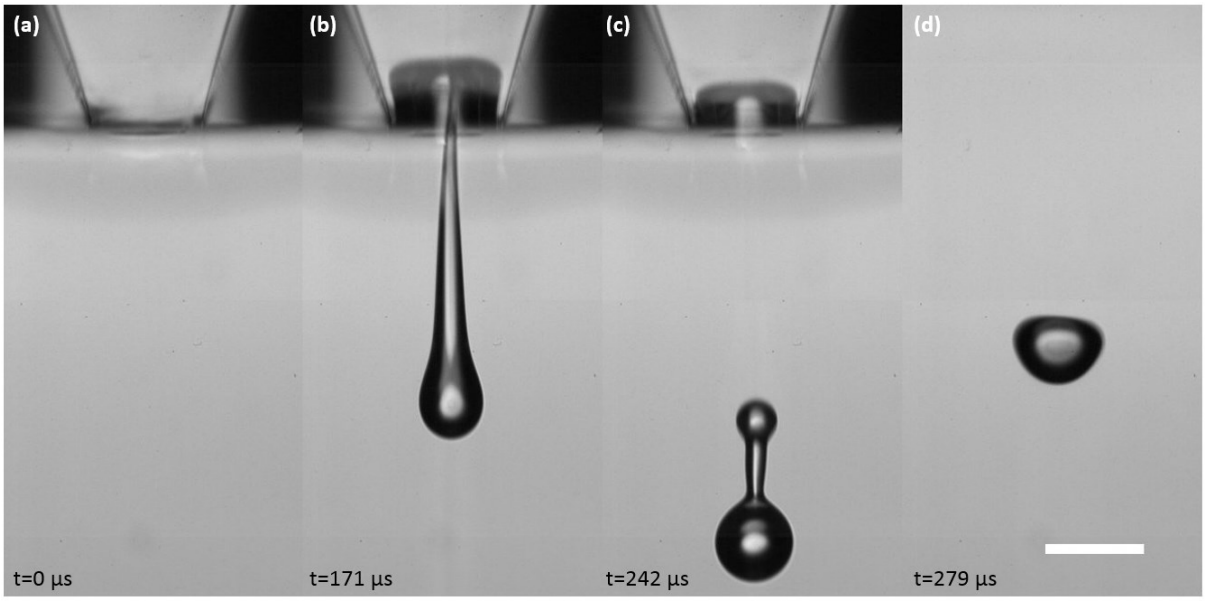

Figure 4.2 Drop ejection sequence of a drop from a MicroFab 80 µm nozzle. (a) Nozzle orifice at steady stage ready for printing. (b) Drop ejected from the orifice with an elongated tail, and sucked back due to negative pressure. (c) Drop broke from the orifice, and satellite formed. (d) The satellite re-joined the main drop and formed one single drop. Scale bar 100 µm. The time shown in the figure is the time passed after the trigger.

Figure 4.2 (a) illustrates the rest state of a printhead orifice, which is set for printing. It is noticeable that the level of the ink inside the nozzle is flush with the orifice. This is controlled and adjusted by the pneumatic control system. Excessive backpressure will draw the liquid level inside the nozzle, and insufficient vacuum will result in the formation of a liquid 'pool' outside the orifice that covers the whole orifice surface. Under both circumstances, the actuation of the nozzle will not be able to provide enough energy to form a jet. As demonstrated in Figure 4.2 (c), there is beading of the filament as it collapses back into the droplet. This is portion of the droplet that can break into a satellite. Due to the limitation of the camera field of view, it is not feasible to capture a high resolution image of the nozzle and the final drop formed, therefore Figure 4.2 (d) was captured by manually moving the camera downward with the mounting system, and imaging a second droplet printed using the same settings. The beaded filament is pulled back by the surface tension and coalesces with the main drop in Figure 4.2 (d).

The behaviour of this fluid filament decides the formation of satellites, as this is where the neck will break. Recoil of the tail occurs because the two spheres attached to the liquid thread are asymmetrical, and with a high pressure at the pinch-off end [81]. The merging of the bead into the main drop can transform the surface into drop oscillation, as shown in Figure 4.2 (d), whereas breakup of the neck leads to satellite formation. Surface tension and viscosity dominate the printing performance of the ink, surface energy is the free energy change when the surface area of a medium is raised by a unit area [83]. Energy is consumed when new surfaces are created, therefore the tendency of keeping the droplet at minimum energy level allows the droplet to maintain its lowest surface area state, which is a sphere. Viscosity arises from collision of neighbouring particles that moving at various velocities and therefore can also be treated as the resistance of drop contraction via surface tension [61]. The following dimensionless groups take these properties into account and are introduced here to help characterise the printability of the ink. The Reynolds number (Re) is the ratio between inertial and viscos forces, which is defined by:

$$\mathrm{Re} = \frac{\rho d V}{\eta} \quad (4.1)$$

Where ρ is the density of the liquid, d is the diameter of the drop, V is the velocity, and η is the viscosity. The Weber number (We) is the ratio between inertial force and surface tension, which is closely related to the bouncing behaviour of the droplets. We is denoted by:

$$\mathrm{We} = \frac{\rho d V^2}{\sigma} \quad (4.2)$$

Where σ represents the surface tension of the fluid. The Ohnesorge number (Oh) is:

$$\mathrm{Oh} = \frac{\sqrt{\mathrm{We}}}{\mathrm{Re}} = \frac{\eta}{\sqrt{\sigma \rho d}} \quad (4.3)$$

Oh is disparate compared with Re and We, as the velocity is eliminated from the equation, therefore the external forcing dynamics is not relevant. It is however essential in understanding the shape and size of the droplets [84].

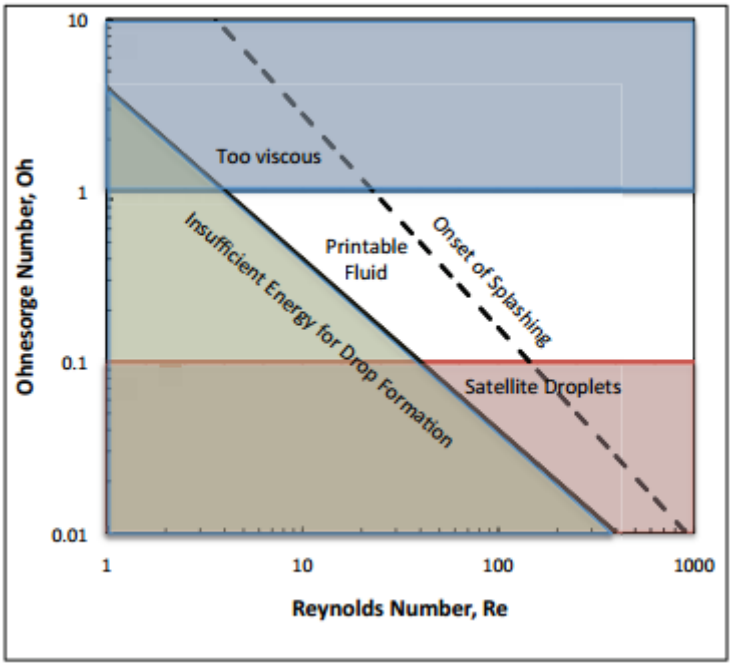

Figure 4.3 Schematic diagram of operating regime for stable operation of DOD inkjet printing [85].

The detailed relationship between these dimensionless groups and the final formation of the drops is shown in Figure 4.3. In the blue zone the fluid is too viscous, while in the red zone the satellites form. In the green triangle zone, the energy applied is insufficient to induce drop formation. Only the white zone in the middle between the solid and dash lines is the most suitable printing condition. In summary, Re is the ratio of inertia to viscous forces, We is the ratio of inertia to surface tension forces, while Oh is the ratio of Re and We which reflects the printability of the fluid, represented by the central region of Figure 4.3.

Previous studies of glycerol/water solution filament breakup show that the breakup of a free cylindrical liquid filament with spherical end caps is closely related to the length of the liquid filaments [81] and Ohnesorge number (Oh) [86]. At low Oh the drop ejection from a nozzle can form a large drop followed by filaments similar to Figure 4.2 (b), at this stage, the surface tension plays a significant role in the jetting behaviour [82]. The length of the liquid filament increases with the driving voltage, and the longer liquid threads, the more satellites it can form. At higher Oh, the viscous forces take the dominance, and end-pinching can be observed [87]. There are several models of prediction for the end-pinching, one is the end-pinching stops when

Oh < Oh* (0.005 < Oh* < 0.01) [88], the other is Oh < 0.1 with sufficient filament aspect ratios (ratio of length and radius) the threads will pinch off near the end [89], and the second model fits glycerol water solutions better. This basic theory is used with the data of GW solutions in the Chapter 3 to estimate the Oh to help with prediction of printability. Calculations are initially based on the estimated diameter of the droplets, as it is commonly expected the drop diameter will be approximately the diameter of the nozzle. These initial calculations are displayed in Table 4.1.

Table 4.1 Oh for glycerol water solutions

wt. % of glycerol	Oh (50 µm)	Oh (80 µm)	Oh (120 µm)
20	0.03	0.02	0.02
30	0.04	0.03	0.02
40	0.06	0.05	0.04
50	0.10	0.08	0.06
60	0.15	0.12	0.10
70	0.32	0.25	0.21

In Table 4.1, it is seen that solutions of higher concentrations of glycerol have higher viscosity therefore higher Oh, but the rise in diameter of the droplet reduces the Oh. For glycerol solutions of less than 40 % of mass fraction, it is easier to generate satellites during printing. This guides the work as it will mean significant waveform tuning to try and reduce the likelihood of satellite formation.

There are several other possible sources of satellite formation, some are attributed to the properties of the fluid, and some are as a result of operational problems. If the dispensed fluid has low viscosity, the energy pressure waves mentioned earlier for drop ejection may provide enough energy to print another drop, which is the main origin of a low velocity satellite. In contrast, while printing polymer solutions or any other viscoelastic fluid, the drop is usually followed by a long thin tail. The tail may then become unstable and break into several small

drops or contract into one satellite (e.g. Rayleigh instability). As a consequence, the viscosity and surface tension are the fundamental considerations required for a meticulous design of dispensing fluids. With respect to the operation of printing, if the voltage is too high, a large amount of liquid will be ejected that is another cause of satellite formation.

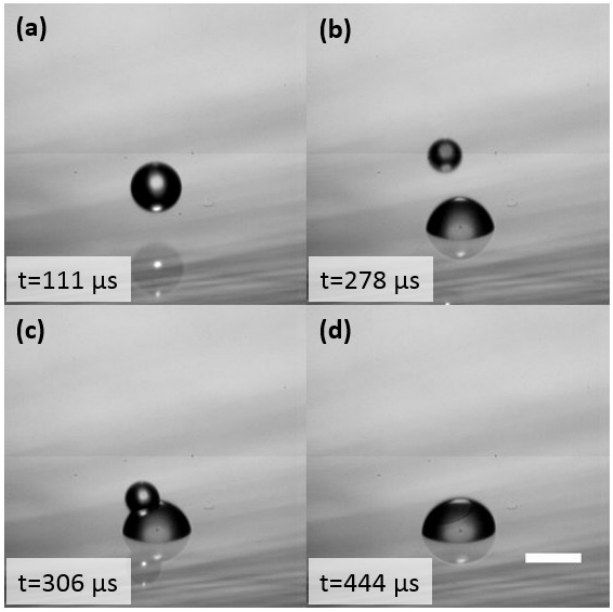

Figure 4.4 Satellite formation. (a) The main drop. (b) The satellite and the main drop already on glass slide. (c) The satellite collides on the main drop. (d) Form one single drop. Scale bar 100 µm. The time shown in the figure is the time in the video.

Figure 4.4 illustrates printing of one single drop onto a glass slide, during initial validation experiments. The main drop lands 111 µs after the start of the waveform and is followed by a lower velocity, smaller satellite. In this situation, the substrate was kept motionless, therefore the satellite following the main drop trajectory can encounter and coalesce with the main drop. If the substrate is moving to the right (or the printhead moving to the left), the satellite may land on the left of the main drop, which may disturb the next drop in the print. For the research reported in this thesis, this is anticipated to lead to defects in the template generated. As the work to study impact and stability as a replacement for the BF technique has not been attempted in the literature, it is essential to keep the experiments as controlled as is feasible and so avoid satellites, even if they follow the same trajectory.

4.2.3 Drop ejection: control of size and velocity

As introduced in Chapter 3, the simplest waveform for printing is a positive trapezium, and to remove satellites, a negative trapezium is required. The most often used wave form is demonstrated in Figure 4.5. This is used for the vast majority of printing in this research, with minor modifications to each constituent parameter.

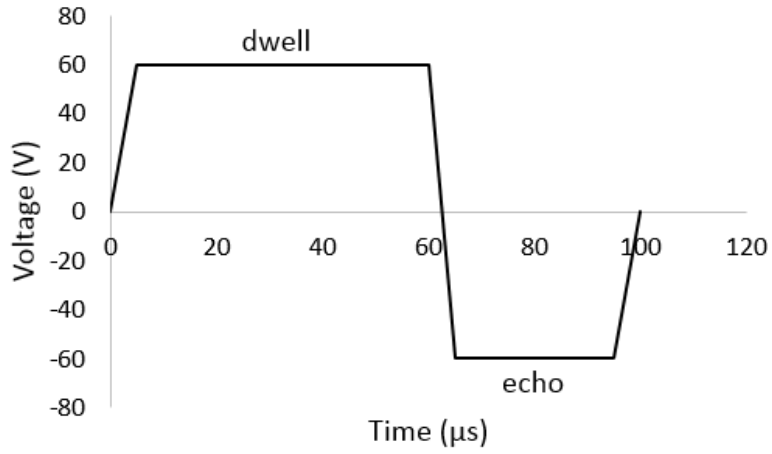

Figure 4.5 Typical printing waveform for glycerol water solutions using MicroFab nozzles.

The rise and fall time were both 5 µs for these MicroFab nozzles. The voltage for ‘dwell’ and ‘echo’ can be changed to find suitable voltage for printing and getting the desired size and velocity of the drop. The ‘dwell’ and ‘echo’ time can be adjusted, as longer ‘dwell’ time can produce larger drops at the same voltage, and the ‘echo’ time is usually half of the ‘dwell’ time. The voltage of ‘dwell’ has an upper limit for MicroFab nozzles which is 140 V. Initial observations from the experiments is that within the printing voltage range, higher voltages can lead to relatively large droplets, however the size of the drop is mainly dependent on the size of the nozzle. Also high voltage can lead to the formation of satellites, and there is a lower limit for different solutions to print. The ‘echo’ is the negative voltage of ‘dwell’, which is set to get rid of the satellites during printing.

Using this waveform, GW solutions were printed with different sized nozzles: 50 µm, 80 µm and 120 µm to test what is the full breadth of the droplet scales that can be addressed with these techniques.

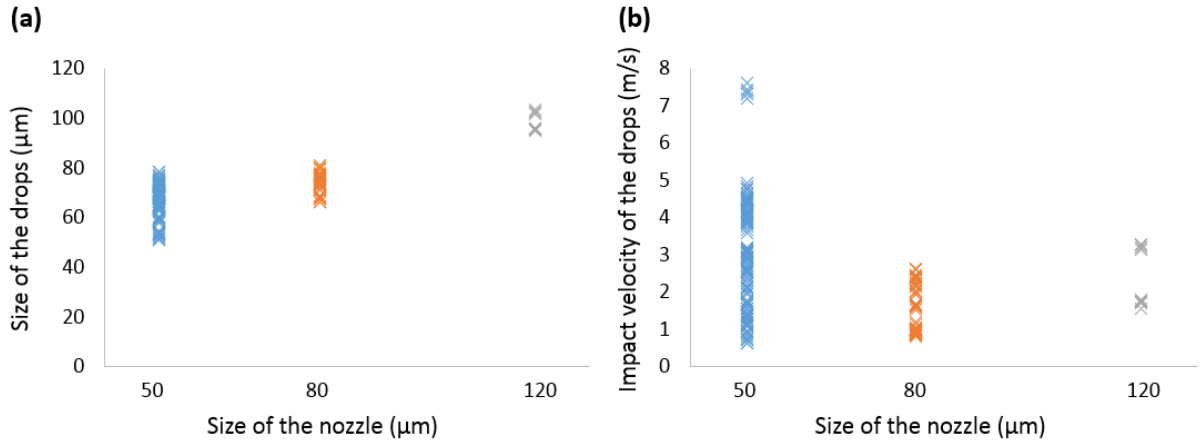

Figure 4.6 Droplets (a) size and (b) impact velocity distribution for 50 µm, 80 µm and 120 µm nozzles.

As shown in Figure 4.6 (a), the size of the droplet, indicating the diameter of the drop, is closely related to the size of the nozzle. For 50 µm nozzle the size of the drop was ranged from 50.8 ± 1.5 µm to 74.3 ± 2.1 µm. Drops printed from 80 µm nozzle varied between 67.5 ± 1.8 µm and 80.2 ± 2.4 µm. With limited printing due to the challenge of ensuring single drops with the 120 µm nozzle, the size captured was within 94.8 ± 2.7 µm to 103.6 ± 3.0 µm. While there is clear overlaps in terms of the achievable drop diameters, these results show that the size of the nozzle limits the accessible size of the drops that can be targeted. In summary, larger drops can be generated from larger orifice sizes. A second critical parameter is the velocity of the droplet. Most often, this is measured as a drop exits a nozzle. However, for this work, it is far more important to understand the impact velocity (velocity of the drop landing on the substrate), as droplets ejected from the nozzle and travel in the air, the velocity decays, and the impact velocity determines the drops' performance of collision, therefore impact velocity was analysed. Interestingly, according to Figure 4.6 (b), the size of the nozzle did not have a significant impact on the impact velocity of the drops. However, it is anticipated (as noted above) that the ejection behaviour can be changed by altering the printing waveform, and so this was examined in more detail. The same nozzles were set at a fixed height above the substrate, then the next part of the research was conducted, documentation of the effect of viscosity and nozzle dimensions.

Parameter set 1: 30% GW solution, 2.2 cP, 50 µm nozzle

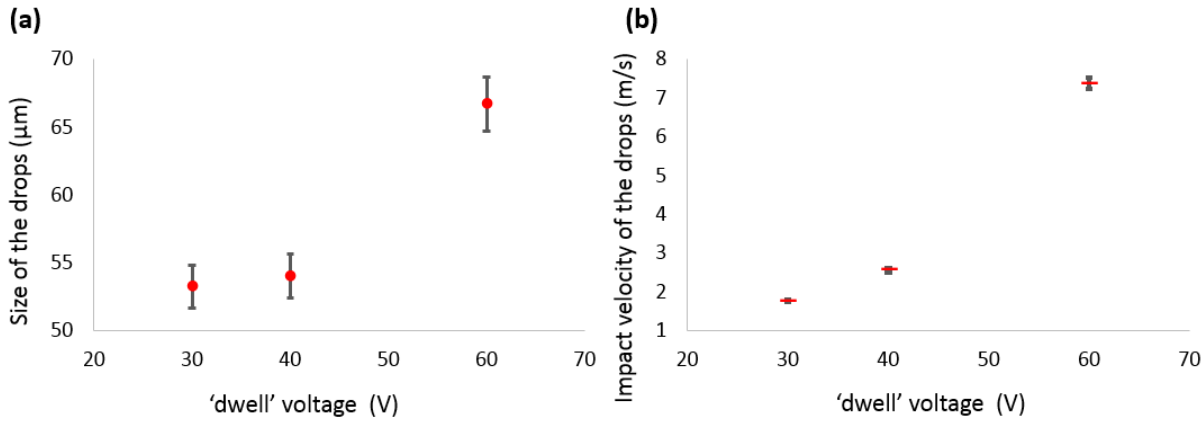

Figure 4.7 Droplets of 30 % GW solution printed with 50 µm nozzle. (a) Size change with 'dwell' voltage. (b) Impact velocity change with 'dwell' voltage.

Droplets were printed changing only the maximum voltage of the waveform. These results were all acquired from 50 droplets printed under each different voltages. While the level of change in size was smaller than observed when changing nozzle dimensions (as shown in Figure 4.6), the size of the droplets can still clearly be tuned through the change in maximum printing voltage. Interestingly, there is a very significant control over the velocity by tuning the maximum waveform voltage. An example is shown in Figure 4.7 (a), where the size of the drop increased slightly from 53.3 µm to 66.7 µm with the rise of printing voltage from 30 V to 50 V, and as shown in Figure 4.7 (b), the impact velocity of the droplets can be dramatically increased by approximately 6 m/s (1.8 m/s to 7.4 m/s) by an increment of 30 V in the 'dwell' voltage.

As inkjet printing literature is rarely transferrable because of slight variations in equipment setup, conditions of printing and use of different nozzles, it was important to map out the parameter space available for consistent printing using the range of nozzle dimensions, and the range of viscosities for each nozzle dimension that is printable. The changing ranges of the size and the velocity of the droplets are also important for studying the impact behaviours of droplets later in this research. Specifically, the following section will report on three additional concentrations of GW solutions for three different sizes of nozzle.

Parameter set 2: 50% GW solution, 6.3 cP, 50 µm nozzle

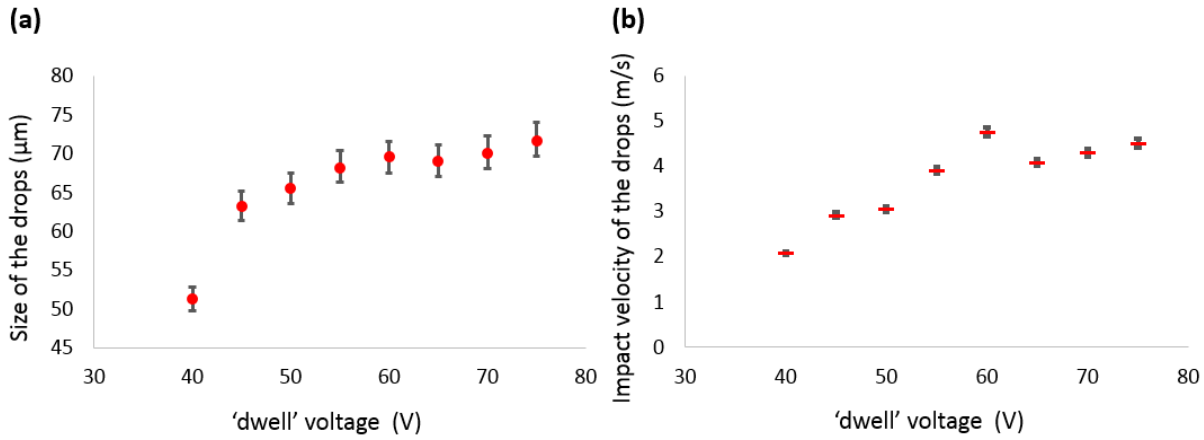

Figure 4.8 Droplets of 50 % GW solution printed with 50 µm nozzle. (a) Size change with 'dwell' voltage. (b) Impact velocity change with 'dwell' voltage.

The viscosity of 30 % mass fraction GW solutions is 2.2 cP (0.0022 Pa·s), while 50 % mass fraction GW solutions has a higher viscosity of 6.3 cP (0.0063 Pa·s). With increased viscosity the minimum voltage required for printing increases. The lower limit for 30 % GW is close to 30 V, while for 50 % GW is approximately 40 V, and the higher limit of printing also increased the tested voltages that is compatible to print 50 % GW are much higher than 75 V, but other parameters need to be changed, therefore in this study only till 75 V was examined and plotted.

Similar to the size change in Figure 4.7 (a), Figure 4.8 (a) also shows the increment of drop size from 51.3 µm to 71.9 µm with the voltage lift from 40 V to 75 V, also there is a sudden change of the diameter from 51.3 µm to 63.3 µm at 45 V. However at 65 V printing voltage there is a slight decline in the droplet size from 69.6 µm at 60 V to 69.1 µm at 65 V. In Figure 4.8 (b), the velocity of the droplets also increased with the voltage, and experienced the same a slight drop in velocity at 65 V, the velocity at 60 V is 4.8 m/s but at 65 V is 4.1 m/s. After this fluctuation, the diameter as well as the velocity of the droplets increase again after 65V, and shown a more gentle increase, then it may indicate a levelling off of the ejection behaviour of 50 % GW after 65 V.

Parameter set 3: 60 % GW solution, 9.5 cP, 50 µm nozzle

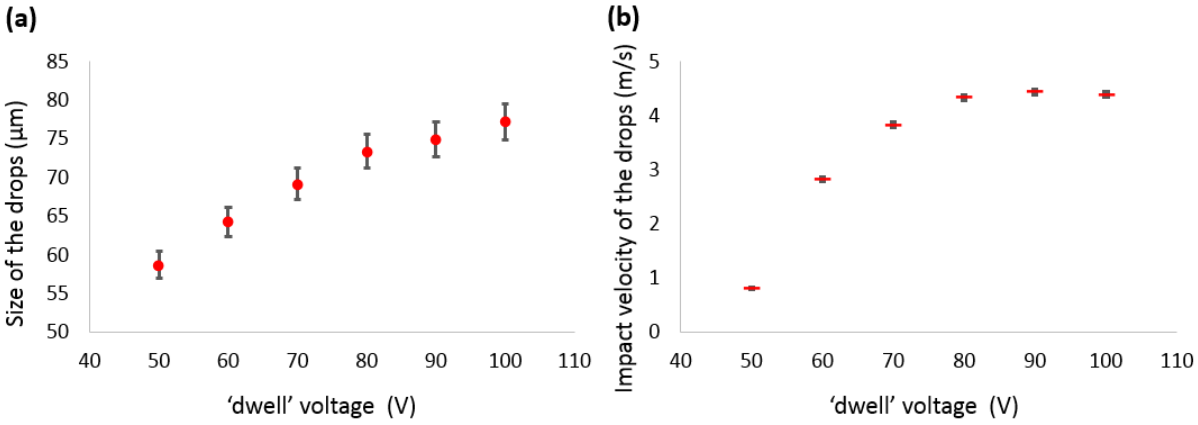

Figure 4.9 Droplets of 60 % GW solution printed with 50 µm nozzle. (a) Size change with 'dwell' voltage. (b) Impact velocity change with 'dwell' voltage.

The 60 % mass fraction GW solution has a viscosity of 9.5 cP (0.0095 Pa·s), which is more viscous than 50 % GW. The minimum voltage again increases, to 50 V, and the upper limit in this test is 100 V. The range of diameter is between 58.7 µm and 77.2 µm, and the velocity range is 0.8 m/s to 4.4 m/s at this parameter set.

As can be seen from Figure 4.9 (a), the size of the drops increased linearly with the increase of the printing voltage before 80 V, from 58.7 µm to 73.4 µm. After 90 V the increase of the size again begins to level off, and the same tendency of velocity change can be witnessed. As can be seen from Figure 4.9 (b), the velocity ramped up from 0.8 m/s at 50 V to 4.3 m/s at 80 V and remains steady around 4.4 m/s after 90 V.

After 100 V the printing of 60 % GW was not stable, satellites formed during printing. Often in the inkjet printing literature, this is not held as an important parameter, especially when examining printability of functional materials. However, for this application it is critical to avoid satellites as mentioned previously. As mentioned for 50 % GW, the waveform can be adjusted to find satellite-free printing, but not considered here.

Parameter set 4: 70 % GW solution, 20.4 cP, 50 µm nozzle

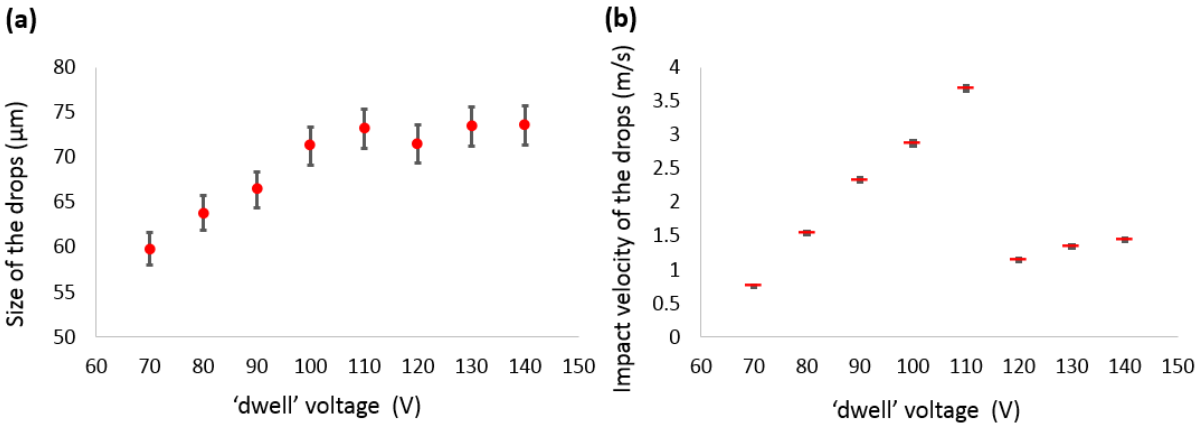

Figure 4.10 Droplets of 70 % GW solution printed with 50 µm nozzle. (a) Size change with 'dwell' voltage. (b) Impact velocity change with 'dwell' voltage.

The viscosity of 70 % mass fraction GW solution increased significantly, which is 20.4 cP (0.0204 Pa·s), therefore the voltage required for printing is much higher, as the minimum voltage is 70 V, and the upper limit reached the limitation of the MicroFab nozzle used which is 140 V, printing at this voltage for a high frequency and long-time printing can damage the nozzle. The range of the diameter is 59.8 µm to 73.6 µm, and the impact velocity range is 0.8 m/s to 3.7 m/s.

With the results mentioned above, and Figure 4.10 (a) and (b) demonstrates clearly a step in the increment of the diameter of the droplets and at the same step the velocity also stopped increasing. There is a threshold voltage, before and after this limit, the size and velocity can both rise with voltage growth. Nevertheless after this voltage the velocity reduced dramatically, and size of the drops fluctuated marginally. This may indicates there is a point within the printing range that the condition of the nozzle might change. At 110 V, the diameter is 73.2 µm, and velocity is 3.7 m/s, while at 120 V, diameter is 71.5 µm and velocity is 1.1 m/s. Then the diameter levelled off at 73.4 µm and 73.6 µm, and the velocity increased to 1.4 m/s. This shows an instability in the printing process under these conditions. The same study was carried out for the two remaining nozzle dimensions.

Parameter set 5: 60 % GW solution, 9.5 cP, 80 µm nozzle

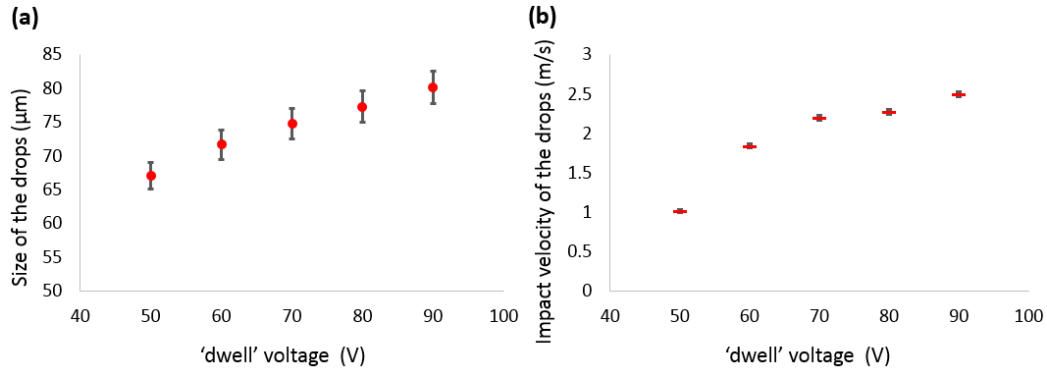

Figure 4.11 Droplets of 60 % GW solution printed with 80 µm nozzle. (a) Size change with 'dwell' voltage. (b) Impact velocity change with 'dwell' voltage.

It has already been shown that a larger nozzle can generate larger droplets. Comparing Figure 4.11 (a) with Figure 4.9 (a) at the same voltage, the size of the drops generated from the 80 µm nozzle is larger than that of 50 µm nozzle (viscosity is constant). However in comparison with Figure 4.9 (b), the velocity revealed in Figure 4.11 (b) is lower at the same printing voltage. In Figure 4.11 (a), the diameter almost changed linearly, but in Figure 4.11 (b), the velocity shows a decline in the speed of rise as well. Furthermore the increment of velocity over the range of printing parameters is from 1.0 m/s to 2.5 m/s, while in Figure 4.8 (b) is 0.8 m/s to 4.4 m/s. This means there is significantly more tuneability for the lower viscosity solutions.

Parameter set 6: 70 % GW solution, 20.4 cP, 80 µm nozzle

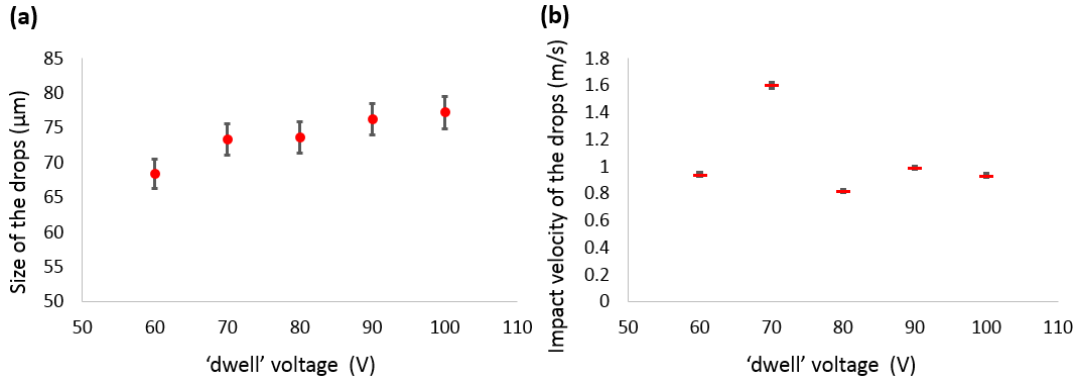

Figure 4.12 Droplets of 70 % GW solution printed with 80 µm nozzle. (a) Size change with 'dwell' voltage. (b) Impact velocity change with 'dwell' voltage.

The trend is again clear here that larger orifice sizes can reduce the voltage required for printing viscous fluids. Using 80 µm nozzle to print 70 % mass fraction GW solution the minimum voltage can reduce to 60 V. The gap is at 70 V to 80 V, where the diameter increased from 73.3 µm to 73.6 (but increased slower), and the velocity dropped from 1.6 m/s to 0.8 m/s. With a 120 µm nozzle, droplets diameter of 94.8 ± 2.7 µm can be generated at 50 V and 103.6 ± 3.0 µm droplets can be generated at 60 V. Comparing with Figure 4.10 (b), the range of variation in velocity is significantly more narrow, as shown in Figure 4.12 (b).

Comparison 1: 60 % GW solution, 50 µm nozzle and 80 µm nozzle

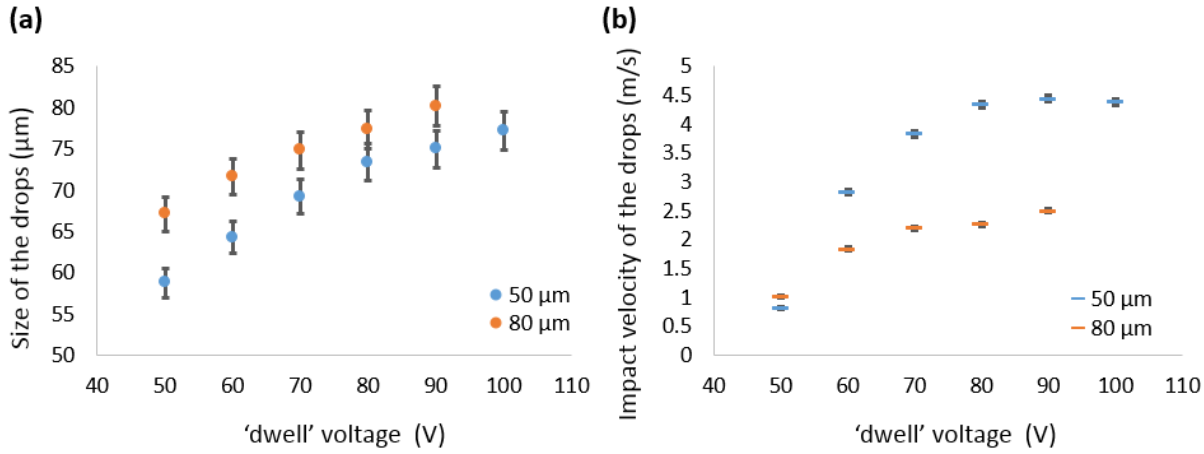

Figure 4.13 Comparison for 50 µm and 80 µm nozzle printed 60 % GW droplets properties.

Figure 4.13 (a) is the graph combining Figure 4.9 (a) and Figure 4.11 (a), to allow the comparison between the size of the drops of 60 % mass fraction GW solutions generated from 50 µm and 80 µm nozzles. It is shown firstly from this chart that at the same peak voltage and printing of the same liquid, the nozzle of greater the orifice size can produce droplets of greater diameter. Figure 4.13 (b) plotted Figure 4.9 (b) and Figure 4.11 (b) together, aimed at comparing the velocity of the drops of the same contents but generated from different sized nozzles. According to this diagram, at the initial onset of printing at 50 V, the velocity of the drop from 80 µm is essentially equivalent to that from 50 µm nozzle, which are approximately 0.8 m/s (50 µm) and 1.0 m/s (80 µm) but afterwards, this diverges rapidly and the velocity of drops from 50 µm is much higher than those from 80 µm. For example, at 90 V, 50 µm nozzle generated drop of 4.4 m/s while 80 µm nozzle printed at 2.5 m/s. For the same liquid, larger

orifice sizes are clearly generating larger but slower droplets. This is despite the effect of de-acceleration being more significant for smaller drops.

Comparison 2: 50 µm nozzle, 50 %, 60 % and 70 % GW solution

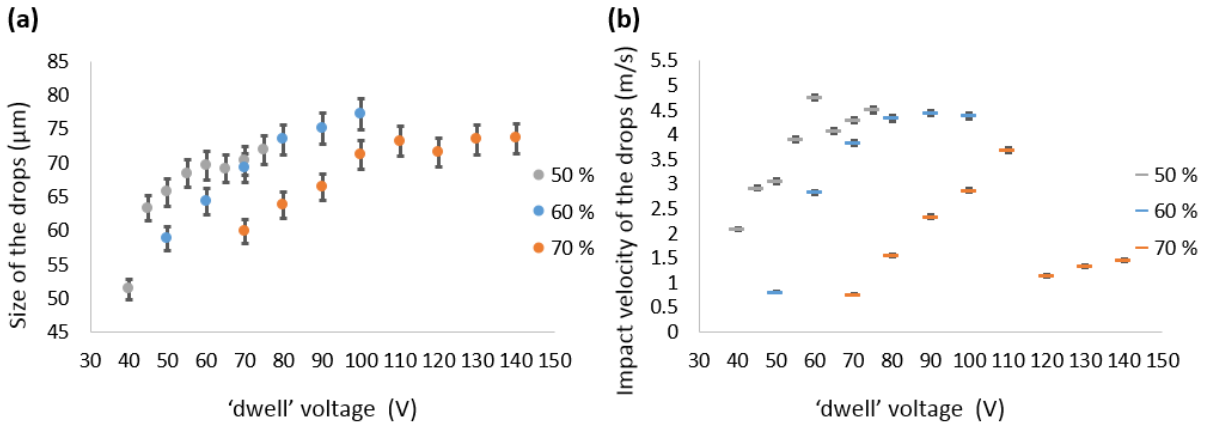

Figure 4.14 Comparison for 50 %, 60 % and 70 % GW droplets properties printed by 50 µm nozzle.

Figure 4.14 shows the comparison between different fluids (50 %, 60 % and 70 % GW solutions) printed with the same 50 µm nozzle. In Figure 4.14 (a), which is the combination of Figure 4.8 (a), Figure 4.9 (a), and Figure 4.10 (a), it is clear that at the same voltage, 50 % GW forms larger drops than 60 % GW, and 70 % GW. However, the lower viscosity solution has a broader range of drop sizes. The tendency of velocity is more complex than the diameter distribution, which is discussed earlier for each graph in Figure 4.8 (b), Figure 4.9 (b), and Figure 4.10 (b). Figure 4.14 (b) combines these diagrams and shows that the lower viscosity droplets are capable of reaching the higher speeds, while the higher viscosities can reach the slower drop impact speeds. These are essential parameters to understand for Section 4.3, where drop impact is examined.

4.2.4 Drop ejection: initial conclusions

Initial conclusions

It was noted at the beginning of this chapter that if the inkjet method is to be used as an alternative approach of drop generation to the condensation in the BF method, it is important to compare the level of control over drop size and the velocity as it impacts the surface. Breath

Figures have a very rapid initial growth and slow, steady growth law after that. However, as noted in the literature review, the growth by condensation can drive defects in the final material due to instabilities in the dynamic system. In inkjet printing, it is shown in the work presented here that the drop size can be precisely controlled by the choice in size of nozzle, the chosen formulation and the voltage of printing. This is equivalent to changing the relative humidity and air flowrate in the BF method. Each size of nozzle chosen limits the range of the drops' diameters achievable, but the maximum voltage of printing then finely tunes the size of the drop within the range. In general, the size of the drop increases with raising voltage, but there is a certain threshold where the printing performance begins to level out. However, an additional constraint is that the range of voltage that can be used may alter for different fluids and nozzle sizes, outside of which there is unstable drop ejection. The voltage chosen along with the waveform also determine the velocity of the drop. For the same printing fluid, a larger orifice size can form larger but slower droplets, also as the fluid is changed to one of increasing viscosity, the droplet speed is also reduced.

Relationship between nozzle diameter and solution viscosity

The range of the drop diameter measured by high speed, high magnification imaging for 50 µm nozzle diameter was 50.8 ± 1.5 µm to 74.3 ± 2.1 µm. A jump in size was seen for the 80 µm nozzle between 67.5 ± 1.8 µm and 80.2 ± 2.4 µm. With limited printing due to the challenge of ensuring single drops with the 120 µm nozzle, the size captured was within 94.8 ± 2.7 µm to 103.6 ± 3.0 µm, which shows that while there are clear overlaps in diameter ranges, it is straightforward to select a nozzle when targeting a size.

The fine tuning of drop behaviour for a specific nozzle showed that for 30 wt. % GW solution printed with 50 µm nozzles, a voltage rise from 30 V to 60 V maintains stable printing and allows fine tuning of drop diameter between 53.3 µm and 66.7 µm. However, the velocity was also observed to increase dramatically from 1.8 m/s to 7.4 m/s. With an increase in viscosity (for 50 wt. % GW solutions) printed with the same 50 µm nozzle, the range of stable printable voltages was wider than that of 30 wt. % GW, which raised from 40 V to 75 V. The diameter rise was nearly identical, varying between 51.3 µm at 40 V to 71.9 µm at 75 V. The velocity followed the same trend, accelerating from 2.1 m/s to 4.8 m/s with a shift from 40 V to 60 V,

but did not reach the velocities recorded at lower viscosities. This was echoed by a move again to a more viscous 60 wt. % GW solution. The diameter was ranged from 58.7 µm to 77.2 µm, and the velocity increased from 0.8 m/s to 4.4 m/s and levelled off. Increasing the viscosity of the printing solution significantly to 20.4 cp by printing 70 wt. % GW solution, the voltage required for printing also increased dramatically, as 140 V is the upper limit for MicroFab nozzles, which can still generate single droplet with this solution. The diameter increased from 59.8 µm at 70 V to 73.6 µm at 140 V. The velocity also rise linearly from 0.8 m/s to 3.7 m/s then dropped significantly to 1.4 m/s.

These results were again echoed with a shift to a nozzle diameter of 80 µm. Figure 4.12 and Figure 4.13 illustrate the comparison for different parameters. Figure 4.12 shown that for 60 wt. % GW, printed with 50 µm nozzle can create droplets of a wider range of diameter and higher velocity, but the size of the droplets are smaller than that of 80 µm nozzle. As Figure 4.13 revealed that lower viscosity droplets are at higher speeds, while the lower viscosities have slower drop impact speeds. Also lower viscosity droplets have larger diameter at the same printing voltage, but as aforementioned, smaller range of printable voltage. These results are summarised in Table 4.2.

Table 4.2 Summary of the results of drop ejection

Nozzle (µm)	wt. % GW	Printing voltage (V)	Diameter (µm)	Velocity (m/s)
50	30%	30	53.3	1.8
		40	54.0	2.6
		60	66.7	7.4
	50%	40	51.3	2.1
		45	63.3	2.9
		50	65.6	3.1
		55	68.4	3.9
		60	69.6	4.8
		65	69.1	4.1
		70	70.3	4.3
		75	71.9	4.5
	60%	50	58.7	0.8

Nozzle (μm)	wt. % GW	Printing voltage (V)	Diameter (μm)	Velocity (m/s)
		60	64.3	2.8
		70	69.2	3.8
		80	73.4	4.3
		90	75.0	4.4
		100	77.2	4.4
	70%	70	59.8	0.8
		80	63.8	1.5
		90	66.4	2.3
		100	71.2	2.9
		110	73.2	3.7
		120	71.5	1.1
		130	73.4	1.3
		140	73.6	1.4
80	60%	50	67.1	1.0
		60	71.7	1.8
		70	74.8	2.2
		80	77.3	2.3
		90	80.2	2.5
	70%	60	68.4	0.9
		70	73.3	1.6
		80	73.7	0.8
		90	76.2	1.0
		100	77.2	0.9
120	70%	50	95.7	1.7
		60	102.6	3.2

(Continued from page 75)

Drop design, find the desired printing condition

The range of the size of droplets that can be generated for different fluid viscosities is plotted in Figure 4.15 (a). The viscosities are related to the concentration of GW solutions. It shows that for an ink of 6.3 cP (50 wt. % GW) there is the widest range of droplet sizes that can be

generated on demand by inkjet printing. For lower viscosities, for example 2.2 cP (30 wt. % GW) there is a narrower range of sizes as it is limited by the size of the nozzle that can be used to print these non-viscous fluids in a stable manner. According to Figure 4.15 (b), there is a broad window of voltages (hence controlled volumes) where each can still allow targeting of a specific impact velocity. Voltages higher than 100 V are not considered for comparison as higher voltages have more restricted printing conditions (only for 70 wt. % GW), therefore limited results were acquired. The same is true for very low voltages (e.g. 40 V). Figure 4.15 (b) reveals that the impact velocity of droplets can be achieved at different printing voltages for different inks. As a result, it is easy to design the impact velocity by manipulating the printing voltage. This is important for enabling the studying of impact behaviour of drops on fluid surfaces.

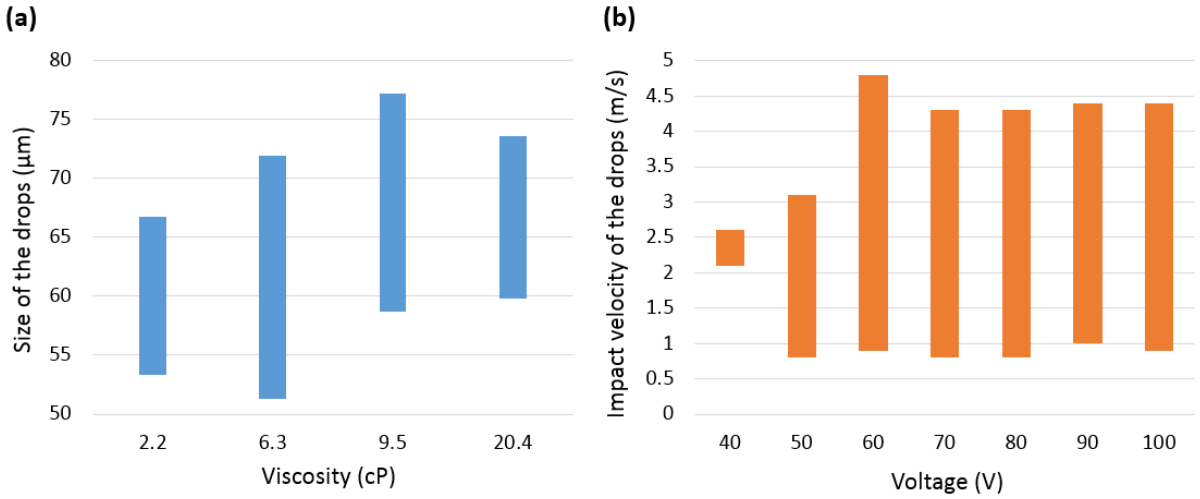

Figure 4.15 (a) Range of the size of the drops for different fluid viscosities across all nozzle diameters. (b) Range of the impact velocity of the drops for different printing voltages across all nozzle diameters.

These results show the printable range of GW solutions of different concentrations (different viscosities), presenting in detail the range of the diameter of the droplets that can be generated and the velocity of the droplets as they impact the fluid surface, which firstly gives the transferrable parameters for other users of MicroFab nozzles, and secondly gives the tuneable impact velocities and diameter of droplets needed for the next section examining impact on fluid surfaces.

4.3 Analysis of drop impact on liquid surfaces

4.3.1 Drop impact introduction

During the research into drop ejection, droplets were printed onto solid surfaces. Imaging focused on the ejection from the nozzle and the subsequent flight. However, a solid surface at the appropriate height was used to enable the estimation of impact velocity already reported. Printing of droplets into fluids is rarely examined and not at the level of detail required to validate a link to the BF technique. In this work, aiming at patterning polymers with droplets produced by inkjet printing, droplets required direct transfer to polymer substrates. To achieve this, the polymer could be dissolved in organic solvents, to directly mimic the BF technique. However, this still leads to the same challenges noted in Chapters 1 and 2 regarding solvent evaporation and control of humidity over time. Alternatively, the work can examine preserving fluid performance (molten, intrinsic fluid properties) for long enough to complete printing and patterning, and subsequently driving a crosslinking process. It is therefore important to analyse the behaviour of droplets impacting organic solvents, to link to the more heavily researched BF technique, and also a cross-linking polymer system. Here it is reported that droplets were printed onto cooking oil, as an available, safe initial material, octyl acetate as a link to the organic solvents used in the BF techniques, polydimethylsiloxane (PDMS) as a crosslinking polymer system, and also de-ionised water to investigate impact behaviours in miscible systems.

The next section of this chapter will therefore study the impact of drops on fluid surfaces, including collision behaviour and the contact angle of droplets in the air/liquid interface, to find a stable condition at which the droplets can be delivered and remain stable in liquids. This work considers only single drops, with the next stage of multiple drops examined in Chapter 5.

4.3.2 Drop impact: range of impact behaviours

Drop impact studies can be traced back as early as in 1870s, when Arthur Mason Worthington first studied the impact ‘pattern’ of milk, water, mercury and alcohol drops of around a few millimetres falling from different measured heights onto smoked glass plates. The marks left

by drop impact showed on the glass and were generally symmetrical with some showing cylinders of liquid arms [90][91]. Afterwards, not only the drop impact on solid surfaces, but also the collision on liquid surfaces were studied from the 1870s. The mechanism of coalescence was also studied and was considered fundamental for the growth of water droplets as it was believed coalescence happens immediately after liquids make contact with each other [92]. However, in 1879, Lord Rayleigh first found water could bounce back upon collision when the water drop vertically on a water surface. It was stated that the rebound phenomenon is owing to the air cushion trapped between the impinging drop and the liquid surface which inhibited true contact, and then coalescence [93].

Different behaviours were reported in the literature upon the collision of droplets on liquid surfaces and categorised into floating, bouncing, splashing and coalescence. The floating is the droplets stay above the surface of the pool without coalescence, this phenomenon relies on the cleanness of the surface [93]. Bouncing of droplets happens for different sizes of drops, mainly of a few millimetres in diameter. For the coalescence behaviour, usually a small crater can form and the drops submerge into the liquid quickly after contact, and form vortex rings. While splashing can create some secondary droplets, and recoil of the crown finally forms a jet and disturbs the surface of the liquid. These different regimes of impact behaviours of drops are shown in Figure 4.16 (a) and these studies were mostly done with water impact on water. In this research, floating and splashing were not captured, as for scale level droplets only bouncing and penetrating of the droplet into the liquid were observed.

Bouncing behaviour in the literature was studied with drop streams of larger than 4 mm drops, the momentum of the drop increased until a threshold condition, above which the rebound of drops stopped [94]. Because drops were printed onto the liquid substrate continuously, it was believed that the first drop decelerated and formed crater therefore the succeeding drops can have a partial crater, which can save them the energy to rebound [94]. Single drop bouncing behaviour was then investigated. It showed that water drops of 75 μm to 150 μm in diameter striking a plane water pool, and there is no sharp boundary separating different impact behaviours, only the possibility of one behaviour happening is larger than the other behaviours [95]. However the impact angle and the We enabled the generalisation of the data and showed the characteristic zones of different impact behaviours, which is shown in Figure 4.16 (b). At

low We the droplet coalesce with the pool and at modest We the drops may rebound and finally splashing can happen at high We [96][97][98][99].

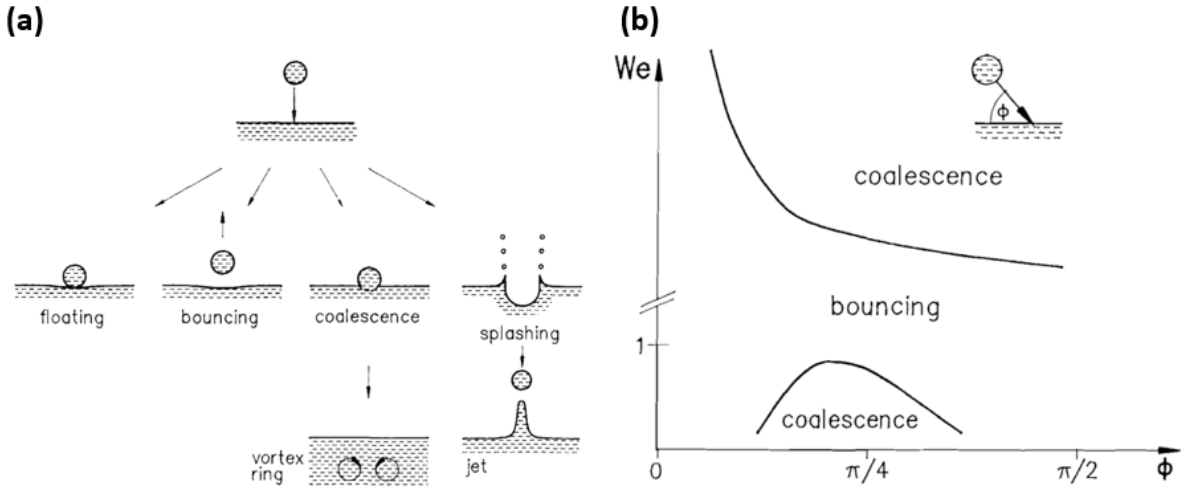

Figure 4.16 (a) Impact of a drop on a liquid surface: floating, bouncing, coalescence, and splashing. (b) Drop impact on liquid surfaces with different regions of bouncing and coalescence [96].

Bouncing of droplets was also investigated in this research, because it is the phenomena needs to be better understood to avoid defects when designing the inkjet printing based process. Also there is very little literature focused on understanding the micron-level droplet impact on liquid substrates. Therefore in this section of research, the threshold of droplets penetrating or rebounding from a vertical impact on different surfaces was investigated and the results are shown in the next section.

4.3.3 Drop impact: results and discussion

Impact on vegetable oil

At the beginning of the research, impact of droplets on vegetable oil was tested. A 50 μm nozzle was used with the 50 % GW solution and from 50 V to 70 V amplitude. This means from the earlier work that we expect a drop speed of on the order of 3.1 m/s to 4.3 m/s upon impact. The impact process is shown in Figure 4.17. Drops generated from the nozzle travelled through the air and collided on the oil surface and gradually submerge into the liquid, finally remaining stable at the oil/air interface.

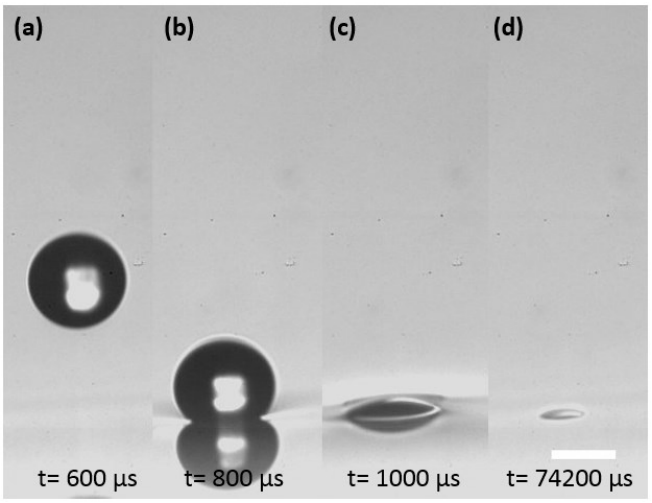

Figure 4.17 Drop impact on vegetable oil. (a) Drop in the air. (b) Drop impact on the surface. (c) Drop submerges into the substrate. (d) Drop finally stabilise at the interface. The time in the images is the time in the video. Scale bar 50 µm.

The submerged behaviour is the only phenomenon captured for droplets impacting the oil surface for any explored conditions. This is a very important result as it shows a similar submerging behaviour to the BF, remaining almost entirely below the surface, with a small spherical cap pinned at the water/air interface. It was critical to explore this in more detail with an organic solvent more closely linked to the BF literature.

Impact on octyl acetate

Octyl acetate was chosen as a solvent as its surface energies are very similar to solvents reported in the literature for BF techniques, without the same level of volatility that would lead to instabilities. A large study was carried out, examining all the impact behaviours of droplets properties shown in Table 4.2 Three different behaviours were identified using this approach, namely (i) penetration, (ii) bouncing and an intermediate behaviour that shows (iii) temporary non-coalescence (caught by the substrate). Only vertical (90° Ø) is considered for the testament, because final aim is to create stable droplets rafts, while other impact angles introduces more complexities.

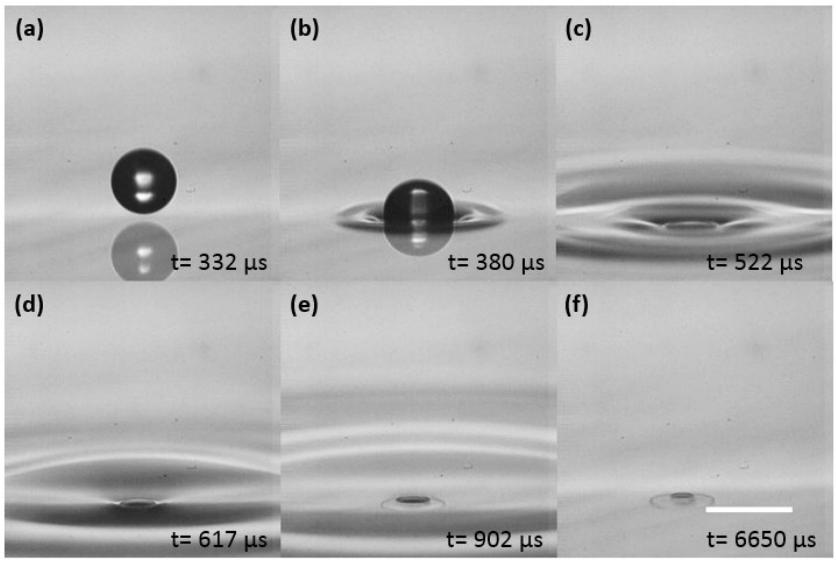

Figure 4.18 Drop impact and submerge on vegetable oil. (a) Drop in the air. (b) Drop impact on the surface. (c) Drop submerges into the substrate. (d) Surface recover. (e) Ripples decay. (f) Stabilise at interface. The time in the images is the time in the video. Scale bar 100 µm.

A representative example of the first behaviour is demonstrated in Figure 4.18. Droplets impact on octyl acetate to form a crater. This spreads as ripples and the surface then recovers. Similar to the drop at oil/air interface, it takes time for the droplet to finally stabilise at the octyl acetate/air interface with a fixed contact angle. This contact angle is explored further in section 4.4. It is important to note that through the full set of tests the drops did not penetrate the liquid and then continue into the bulk of the solution. This shows that there is excellent stability for the required packing in the droplet templating.

The second behaviour observed was that of droplet bouncing. This is revealed in Figure 4.19. This behaviour when printing onto a fluid surface has not reported for inkjet printing previously and so it was explored in more detail later in this section. The drop impact on the octyl acetate surface forms the same crater, but it is assumed that there is a layer of air in between which preventing the penetration of the droplet into the surface, and the drop is propelled back into the air.

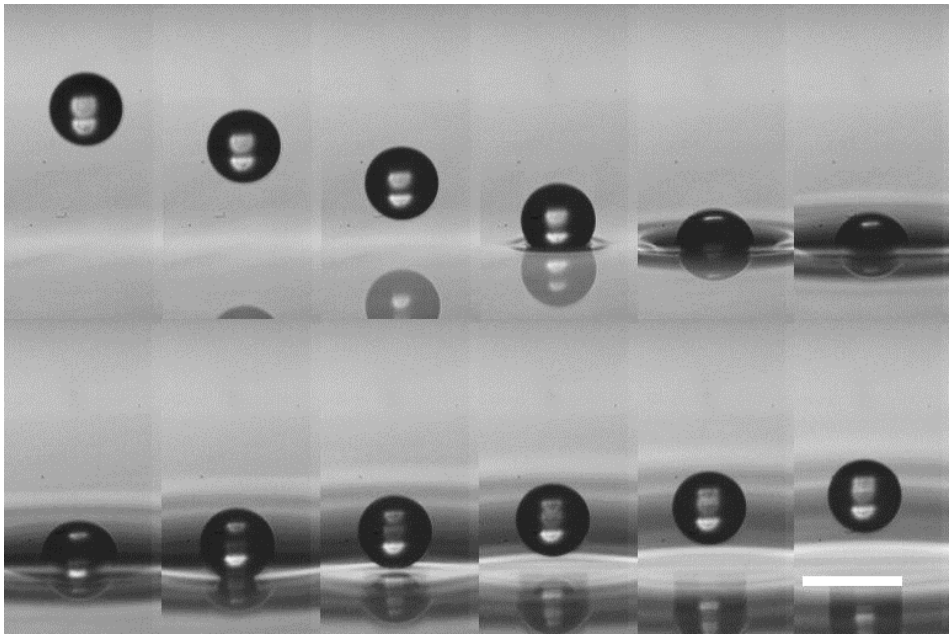

Figure 4.19 Drop bounce after collision on octyl acetate surface. Frame interval 48 μs. Scale bar 100 μm.

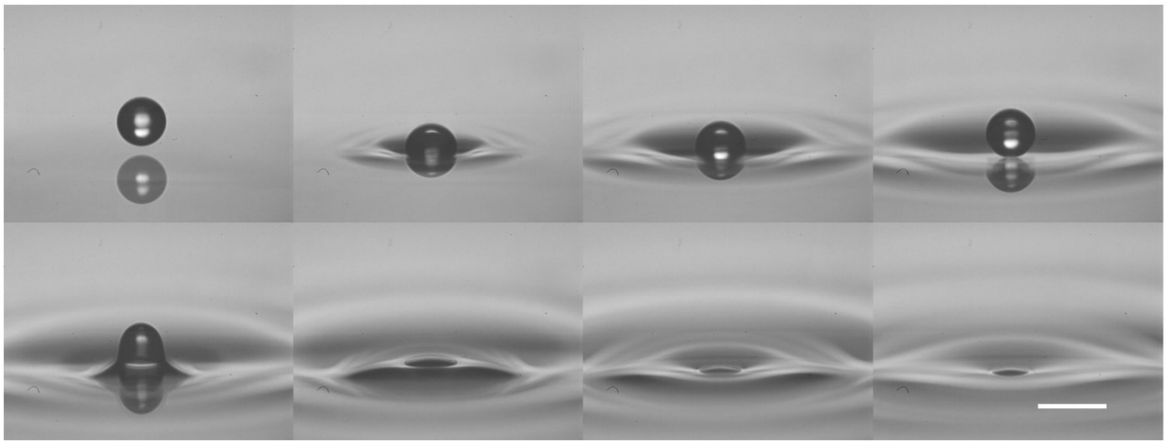

Figure 4.20 Drop tend to bounce but get caught by the substrate. Frame interval 87 μs. Scale bar 100 μm.

As demonstrated in Figure 4.20, a third and previously unreported behaviour was also captured. There is a tendency for the drop to rebound during certain conditions, but then the drop appears to be caught by the liquid substrate and it settles to a submerged state. Bouncing happens when there is air trapped between the drop and the substrate, there are two ways to overcome the air interlayer. The first one is because the drop approaches the substrate so close such that the

intermolecular forces can work to drag the drop into the substrate. The second one is the impact energy is sufficient to break down this air cushion [100].

Impact on water

While such a detailed set of experiments was not carried out, droplets of 50 % mass fraction GW were printed onto DI water for comparison. GW drops impact on water may coalesce with water, which is revealed in Figure 4.21 (d) after the ripple reset there is no drop pinning at the water/air interface. Interestingly, drop bouncing also happened on the water surface. A droplet of approximately 80.1 μm in diameter and 1.0 m/s rebounded upon collision. Droplets that could not rebound have an average size of 68.2 μm, and the velocity ranged from 0.9 m/s to 1.8 m/s. These results prove that the drop rebound is owing to the contactless condition, because once the drop of GW interact with water substrate directly, it would coalesce with the pool. In addition, the rebound velocity is close to the lower boundary of the range of the velocity tested, therefore the region of high possibility of bouncing is the low velocity or We region.

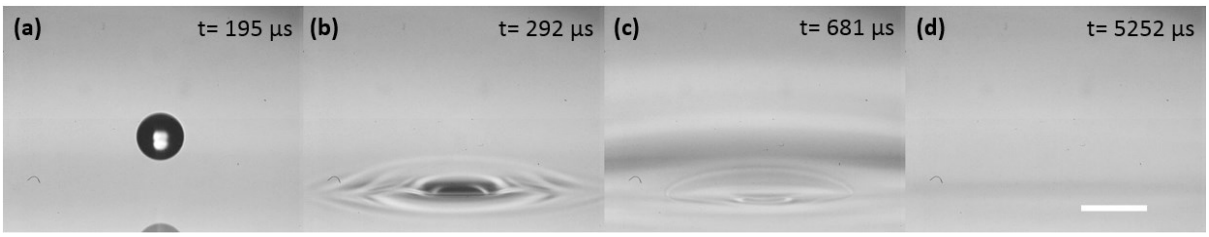

Figure 4.21 Drop impact on DI water. (a) Drop in the air. (b) Impact on water. (c) Expand and interface of GW and water. (d) Surface recover and drop coalesce with water. The time in the images is the time in the video. Scale bar 100 μm.

Impact on PDMS

In contrast to the impact behaviour of droplets on octyl acetate, droplet collision on PDMS resembles that on solid surfaces. The deformation of PDMS surface was not obvious, but as illustrated in Figure 4.22 (b) the drop was compressed to an ellipsoid geometry, then in Figure 4.22 (c) expanded and finally recovered above PDMS surface that is shown in Figure 4.22 (d).

Afterwards, the drop starts to submerge into PDMS. This process takes a much longer time than the drop in Figure 4.18, as PDMS is more viscous than octyl acetate.

It is clear from the large number of experiments above that droplet bouncing was observed most often on octyl acetate surfaces. Therefore the results of droplets impact on octyl acetate were analysed further to explore the threshold where the droplets tend to rebound. From 20 % to 70 % GW solutions were printed onto octyl acetate, bouncing were witnessed for 30 %, 50 %, 60 % and 70 %. Therefore it was assumed that the viscosity of the drop has minor influence on the bouncing behaviour. Instead, there was a focus on the parameters: diameter, impact velocity, Re, and We.

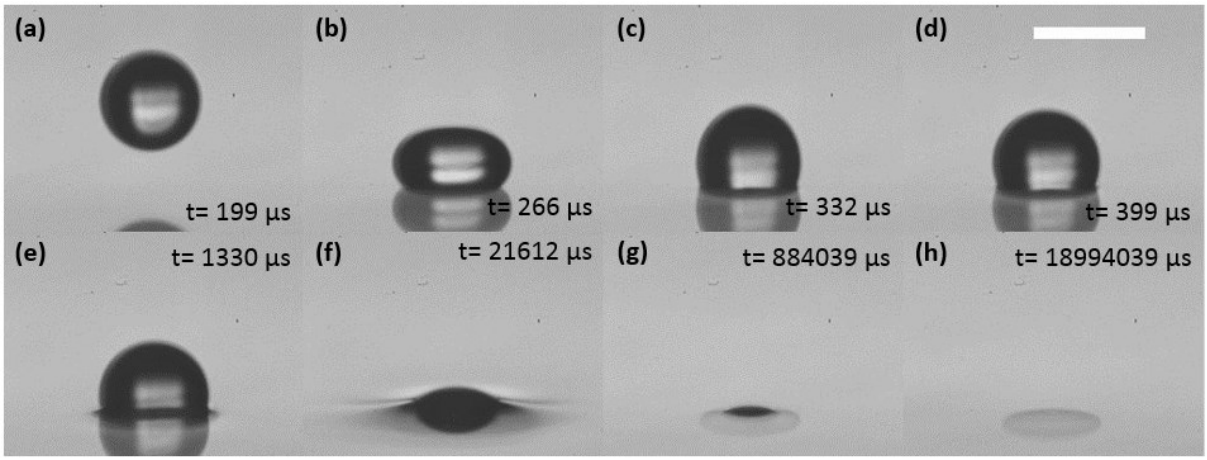

Figure 4.22 Drop impact on PDMS. (a) Drop in the air. (b) Impact and deform. (c) Expand in the upper direction. (d) Drop recover. (e)-(g) Gradually submerge into PDMS. (h) Final state. The time in the images is the time in the video. Scale bar 100 µm.

Diameter-impact behaviour

Experiments were analysed after ensuring only single droplets were created (i.e. no satellites) and that sufficient focus was achieved for the drop such that accurate diameters and velocities could be recorded.

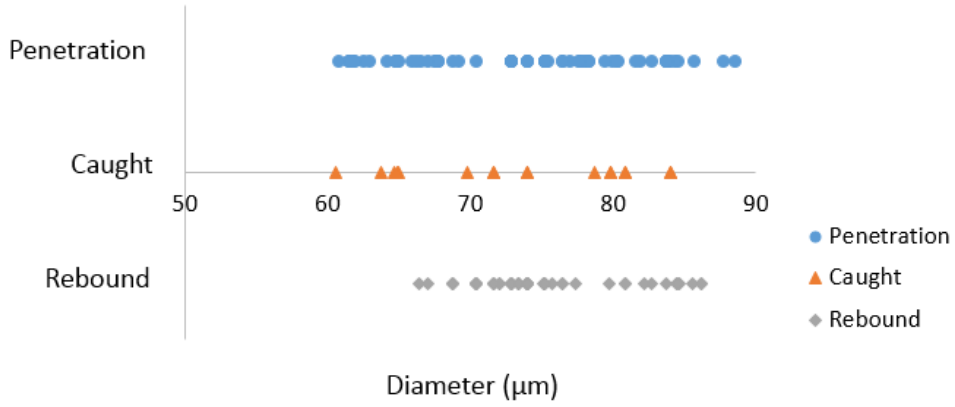

Figure 4.23 Diameter of droplets impact on octyl acetate change for three different impact behaviours.

According to Figure 4.23, the size of the drop was limited by the size of the nozzle used for printing, but with diameter smaller than 65 µm, there was no bouncing behaviour happened. As a result, the diameter of the droplets may not have a simple relationship with the impact behaviour, but droplets ranged from 66.4 µm to 86.1 µm bounced upon collision on octyl acetate, whereas drops below 66.4 µm never bounced. These results shown that larger droplets have higher possibility to rebound, smaller droplets cannot escape the substrate after impact. However, the size of the droplet is not the only determinant for this bouncing impact behaviour, as the range of the diameter spreads over a large range, and overlapped with the size of the caught droplets, therefore other parameters were also examined.

Impact velocity-impact behaviour

Figure 4.24 shows the relationship between the impact velocity and the impact behaviour of the droplets. There are droplets of velocity greater than 3 m/s but at this point upwards they always penetrate the sample, therefore the axis was cut to show more details. Rebound behaviour gathered around the velocity between 0.5 m/s and 1.2 m/s, which is a relatively low velocity range. Most drops 'caught' by the substrate had a velocity of around and below 0.5 m/s. Hence, the bouncing region can be defined as 0.5 m/s to 1.2 m/s where the possibility of rebound is the greatest amongst three impact behaviours and less than 0.5 m/s the drop can easily get caught by the substrate, when above 1.2 m/s the droplet is highly likely to just penetrate the substrate surface and pin at the interface. The droplets have an impact behaviour

shown in Figure 4.17 usually have high velocity, while impact behaviour in Figure 4.18 occurred at low velocity and Figure 4.19 sometimes require even lower velocity than the rebound one.

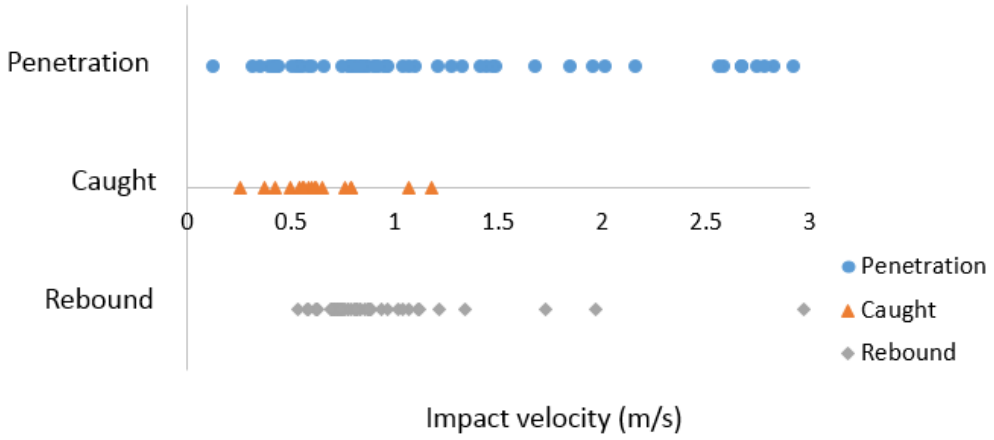

Figure 4.24 Impact velocity of droplets (less than 3) impact on octyl acetate change for three different impact behaviours.

Re-impact behaviour

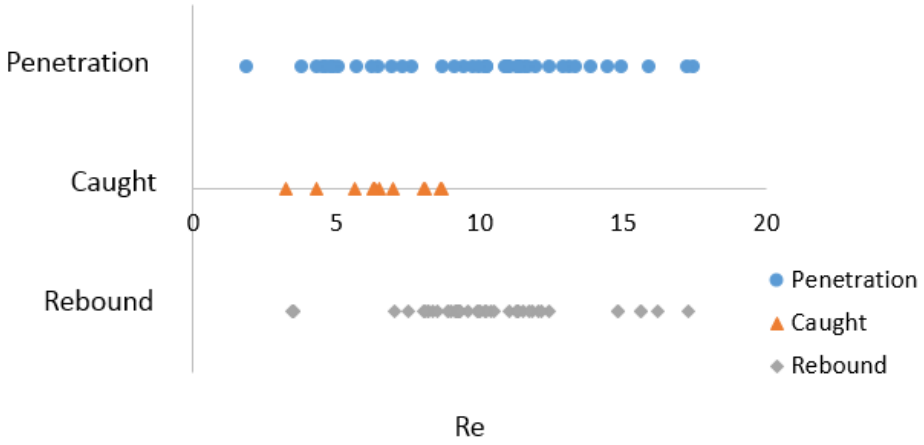

Figure 4.25 Re of droplets (less than 20) impact on octyl acetate change for three different impact behaviours.

Similar conclusions can be seen from Figure 4.25, which displays the effect of Re of droplets on their impact behaviours. There are droplets of Re greater than 20 but these no longer rebound, therefore the axis was cut to show more details. Droplets of low Re, there is no

significant rebound behaviours, and between 3.2 and 8.7 some droplets will possibly experience some non-coalescence but then be caught by the surface. Also, high Re is stable for printing, however from 8.1 to 12.2 there appears to be a likelihood of droplet bouncing. Few points of higher Re over 15 also have bouncing happened.

We-impact behaviour

In section 4.3.2, the literature review showed that the We has a close connection with the droplets impact behaviour. There are droplets of We greater than 3 but these never show bouncing, therefore the axis was cut to show more details. Low We number and high We number prevent droplets from escaping the substrate, 0.3-1.2 is the region of bouncing. Nonetheless, the region does not have sharp boundaries to justify which impact behaviour is going to happen at certain We. Then log We against log Re was plotted to have a clearer view of the rebound region. It is quite obvious in Figure 4.27 that the rebound behaviour lies between the caught region and the penetration region. Penetration can always happen, but the mid-region has a very high possibility of droplets bouncing.

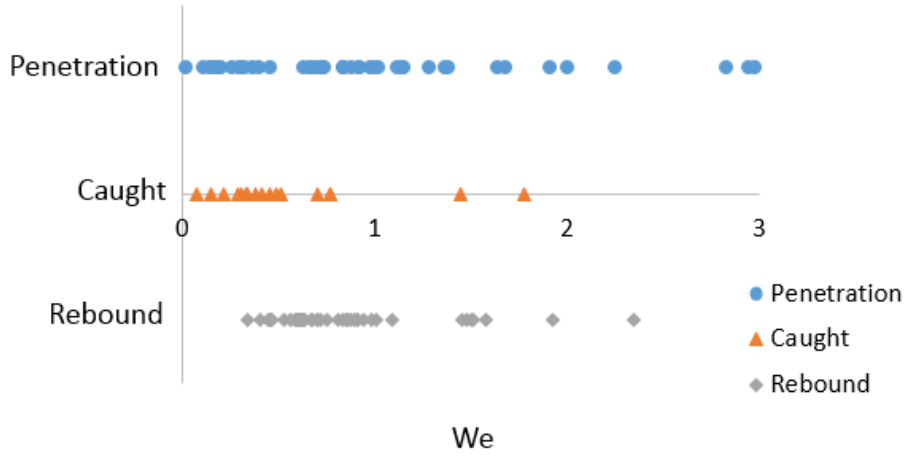

Figure 4.26 We of droplets (less than 3) impact on octyl acetate change for three different impact behaviours.

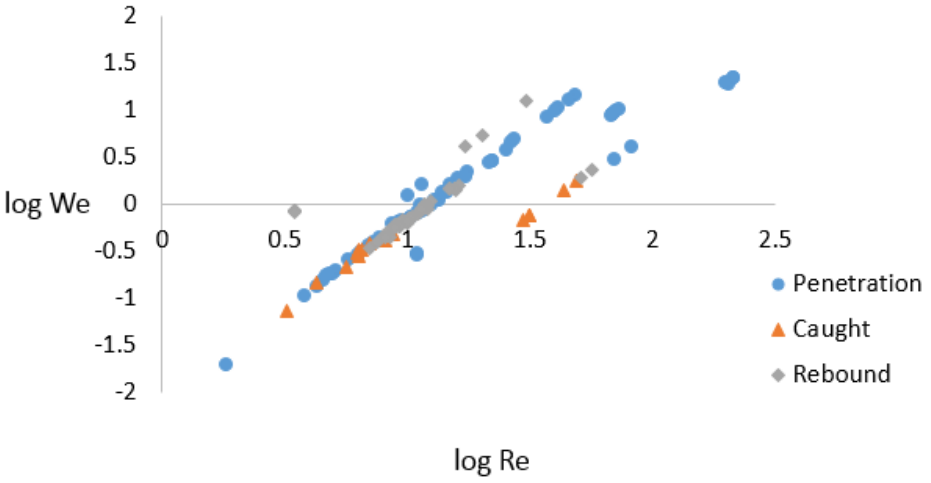

Figure 4.27 log We – log Re plot of droplets impact on octyl acetate for three different impact behaviours.

4.3.4 Drop impact conclusion

Inkjet printing is a highly controllable way of generating droplets of the same size. Utilising nozzles of the same size with a fixed waveform to print a liquid, the size of the droplets can be the same. The size of the droplets depends on the size of the printhead in a scope that is still modifiable by the printing waveform within certain ranges. Generally a higher printing voltage can lead to larger droplets, and the size is slightly different for different inks. The velocity of the droplets also relies on the peak voltage of the driving waveform, where high voltage can generate higher velocity droplets. However there is a critical value where the increment for both the size and the velocity of the droplets stops and increase again after this value. Compared with BF method, inkjet printing is a more reliable method for generating monodisperse drops.

Droplets printed onto octyl acetate and water can rebound from the surface. This is due to the air interlayer prevented the direct contact between the drop and the substrate. The rebound of droplets should be avoid when designing inkjet printing for fabrication. The results shown that relatively larger droplets of low velocity and low We have a higher possibility to rebound. However there is no sharp boundaries to turn on and off this drop rebound behaviour, only regions of high possibility can be detected and circumvented.

Nevertheless, in this research the range of speed that the current set-up and the inkjet printhead can reach limited behaviour of droplet impact. Also the fluid chosen was limited for the purpose of patterning polymers. More general rules of this micron level droplet impact behaviours can be examined by testing additional liquids and optimising the experimental rigs to get a wider range of impact velocities and drop sizes.

In addition, there are certain levels of uncertainty of the drop impact, because the influence of the collision wave is not considered at this stage. The ripple formed by drop impact may affect the impact behaviour of the drops hit the surface before the wave vanishes, especially in the case of drop collision on organic solvents. This is controlled by visually determine the time for the oscillation decay to a resting status, but not quantified therefore may have bias. The impact mechanism of drops colliding on the rippling liquid surface may be worth investigating in the future. From this work, it is also clear that drops are very stable once they penetrate the liquid surface and so this is defined further in the following section.

4.4 Single drop stability

4.4.1 Single drop stability introduction

According to the results in the previous section, the printed droplets were all pinning at the substrate-air interface instead of fully submerging into the substrate, except on water where the droplets coalesced with the bulk. This pinning is due entirely to the surface tension balance, rather than buoyancy, based on the size of the droplets. After eliminating the bouncing droplets, the stability of single printed droplet on the substrate were briefly examined. The research on single drop stability aims to study the stability of droplets at the substrate surface by identifying different contact angles. As introduced earlier, the change of contact angle has a significant effect on the final the pore geometry of the polymer (mainly the opening size of the pores in the polymer), thus the potential of changing the release speed of the contents within the pore for a drug delivery example. In the next section, the relationship between the contact angle and the surface tension of liquids is going to be introduced, and in the results section, the results of the droplet contact angle measured on different substrates is going to be discussed.

4.4.2 Single drop stability: surface tension and contact angle

When the droplets are sufficiently small, the gravitational effects are negligible. The shape of interface only depends upon the interfacial tension when the capillary length exceeds the droplet's diameter [101]. Capillary length (λ_c) is defined as a characteristic length scale below, which the surface tension forces are dominating.

$$\lambda_c = \sqrt{\frac{\gamma}{\rho g}} \quad (4.4)\ [102]$$

Where g (≈ 9.8 m/s^2) is the gravitational acceleration and ρ (kg/m^3) is the density of the fluid, and γ (N/m) is the surface tension of liquid-liquid interface. The capillary length in this work is between 2.4 mm and 2.6 mm, and the droplets diameter are much lower than these values.

For the liquid drop floating on another liquid the three phase surface tension balance can be described by the Neumann's triangle conditions [83]. Neumann's triangle describes the equilibrium of droplets on liquid surface that is demonstrated in Figure 4.28.

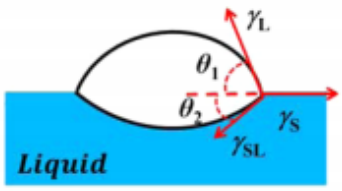

Figure 4.28 Neumann's triangle conditions: $\gamma_S = \gamma_{SL}\cos\theta_2 + \gamma_L\cos\theta_1$; where γ_L is the surface tension of the liquid, γ_S substrate and γ_{SL} substrate/liquid, adapted from. [103]

Work to describe this three-phase balance also often includes the three-phase line tension. This is the linear tension found at the three-phase line where the three interfaces meet [104]. For example, in Figure 4.27, there is a ring that the two liquids contact with each other and surrounded by the air. As shown in Figure 4.29, a, b and c are oil/water, oil/vapour and water/vapour interfacial tensions, r (m) is the radius and τ (N) is the line tension.

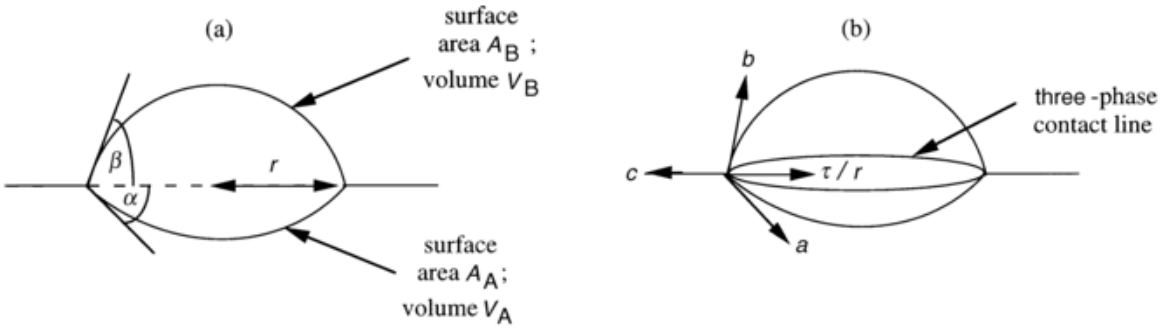

Figure 4.29 Lens on liquid surface (a) relevant angels of two spherical caps of the lens. (b) Tensions in the system, where a, b and c are interfacial tensions and τ is the line tension in the three-phase contact line. [105]

Resolving forces horizontally at the contact line gives:

$$c = a\cos\alpha + b\cos\beta + (\tau/r) \quad (4.5)\ [105]$$

When $\tau = 0$ (absence of line tension), equation 2.x becomes

$$c = a\cos\alpha + b\cos\beta \quad (4.6)\ [105]$$

Which is the same as the Neumann's triangle condition equation.

Aveyard and Clint summarised the equations for angles α and β [105]:

$$\cos\alpha = \frac{[c-(\tau/r)]^2 + a^2 - b^2}{2a(c-\tau/r)} = \frac{c^2(1-\bar{\tau})^2 + a^2 - b^2}{2ac(1-\bar{\tau})} \quad (4.7)\ [105]$$

$$\cos\beta = \frac{[c-(\tau/r)]^2 + b^2 - a^2}{2b(c-\tau/r)} = \frac{c^2(1-\bar{\tau})^2 + b^2 - a^2}{2bc(1-\bar{\tau})} \quad (4.8)\ [105]$$

Where $\bar{\tau} = \tau/cr$ (4.9) which is reduced line tension.

It was also reported that Neumann triangle represents the three-phase equilibrium of droplets at liquid interfaces. They defined a standard measure of surface stability, e, which is based on the Neumann triangle [106]:

$$e = \frac{\gamma_{2/3} - (\gamma_{1/3} + \gamma_{1/2})}{\gamma_{2/3}} \times 100\% \quad (4.10)\ [106]$$

Where e > 0 the droplet will submerge, and e < 0 the droplet is stable at liquid/ air interface. The contact angles of the droplets on liquid surfaces in this research were estimated with the assumption that the droplets at the interface did not changed the shape (the droplets are spherical). The results of the measured contact angle and the calculated values are compared in the next section.

4.4.3 Single drop stability: results and discussion

The droplets set at the substrate/air interface left a small cap above the substrate surface, which is shown clearly in Figure 4.18 (f), as introduced in previous section it is due to surface tension. To estimate the contact angle, an assumption was made that the droplets remained a sphere at the interface. Hence according to Figure 4.30, the value of r can be measured and R is the radius of the drop then the contact angle α can be calculated.

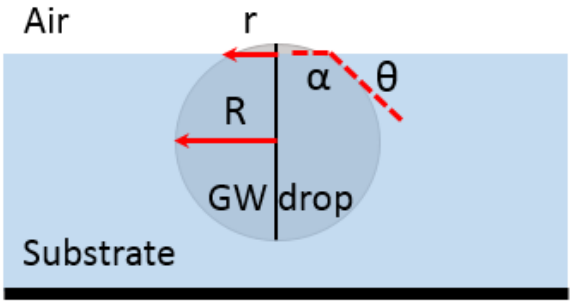

Figure 4.30 Estimation of the contact angle of droplets of GW solutions at substrate surface.

The measured value of r/R for different substrates were:

$$r/R_{oil} = 0.32 \pm 0.03$$

$$r/R_{OA} = 0.30 \pm 0.05$$

$$r/R_{PDMS} = 0.12 \pm 0.02$$

The contact angle α can be calculated:

$$\alpha_{oil} = 180° - \theta_{oil} = 180° - \sin^{-1} r/R_{oil} = 180° - 18.7° = 161.3° \pm 1.8°$$

$$\alpha_{OA} = 180° - \theta_{OA} = 180° - \sin^{-1} r/R_{OA} = 180° - 17.5° = 162.5° \pm 3.0°$$

$$\alpha_{PDMS} = 180° - \theta_{PDMS} = 180° - \sin^{-1} r/R_{PDMS} = 180° - 6.9° = 173.1° \pm 1.1°$$

The estimated contact angle from Neumann's triangle is 178.9°, but e value is 11.7 %, which is larger than 1 represent that the droplets should submerge in PDMS, however droplets were pinned at the PDMS/air interface.

4.4.4 Single drop stability conclusion

The measured contact angle of GW droplets on oil is 161.3° ± 1.8°, on octyl acetate is 162.5° ± 3.0°, and on PDMS is 173.1° ± 1.1°. These contact angle remained the same for all the observed droplets, which is determined by the surface tension. By changing the substrate surface tension and the drop contents, the contact angle can be controlled and the porosity of final product can also be set. The predicted contact angle for these drops, based on surface tension measurements for PDMS is 178.9°. As noted previously in the literature, it is highly likely that there is some mutual miscibility at the interfaces and also migration of the bulk fluid across the surface of the water droplet [106]

4.5 Single drop generation, impact behaviour and stability summary

The results demonstrated that inkjet printing is a stable and efficient way of generating micron scale droplets and delivering to the liquid substrate, by altering the size of the nozzle to print and the driving signals, the size of the droplets and the impact behaviour can be controlled. Three different impact behaviours were observed, which were namely penetration, bouncing and an intermediate behaviour of temporary non-coalescence finally caught by the substrate. The results shown none clear critical values for the occurrence of the bouncing of droplets, but regions of relatively low impact velocity and We have higher possibility for rebound to happen. To eliminate the rebound behaviour, the high possibility regions should be avoided while printing. Afterwards, the droplets delivered to the substrate can stabilise at the substrate/air interface instead of fully submerge into the bulk pool, with a small 'cap' above the surface and the main body is under the surface. This is owing to the surface tension effect, which gives the

freedom of design and control the porosity of the final product by controlling the contact angle of the droplets, thus surface tension of the droplets as well as the substrate.

These results shown that the inkjet technique of direct droplet deposition is suitable to attempt as an alternative to replace the BF method when producing the drop template to produce porous polymers. As it can generate uniform droplets with the same sized nozzle at the same printing waveform. The surface tension property of the droplets can be controlled, therefore the contact angle can be controlled, and when the droplets are captured the contact angle determines the opening size of the pores which is a key parameter to the morphology and the functionality of the porous polymer.

With each of the printed droplets stable on the substrate, it is important to examine printing of more droplets to form the template. While more droplets are printed, the droplet contact during printing and the interactions between neighbouring droplets on the substrate can also affect the quality of the final pores. Therefore the stability of multiple droplets is going to be discussed in the next chapter.

Chapter 5 Multiple droplets stability on liquid surfaces

5.1 Multiple droplets stability on liquid surfaces introduction

As explained in Chapter 4, to translate the direct printing of droplets to the BF method, a detailed understanding is needed of the control of drop speed and size to examine the stability of a single droplet landing on the liquid substrate. It was shown that while there are three different impact behaviours, it can be controlled to the extent that it is highly probable a drop will penetrate into the liquid surface. Also, the contact angle appears to be repeatable for a chosen system of liquids. The impact behaviour determines if the droplets land on the substrate at the programmed position, and the contact angle changes the position of the droplet relative to the polymer solution/air interface. In the BF method, as discussed in Chapter 2, droplets grow steadily by condensation. They are closely packed from an early stage in the process and so there are often coalescence events. The source of the stability that prevents this from occurring at a greater speed is not completely understood, but may be due to rapid evaporation of solvent or precipitation of materials at droplet interfaces. It is not understood what will happen when droplets are delivered to the surface, as they will make contact with each other during printing in a very different way to the BF method. Droplets on the surface will most likely interact with neighbouring droplets before convection driven self-organisation. In this chapter, drop stability is studied and it was decided to examine firstly the level of separation required to ensure stability on different substrates. As in Chapter 4, vegetable oil was examined initially due to its ease of availability and safety. Detailed analysis was then carried out using octyl acetate and polydimethylsiloxane (PDMS) as the liquid surface. The comparison of drop stability results for different substrates is discussed and reveals the relationship between the contact angle, thus the surface tension and the minimum separation distance.

The second part of this chapter will examine a different approach, where the droplets are separated by a significant distance to avoid stability issues during printing. With the goal of creating a monodisperse, ordered and close packed pattern of droplets, the array starts with large spacings and these are driven closer by convection-driven self-organisation. In this case,

the stability of rafts of multiple droplets needs to be studied. In the BF method, the mechanism of self-organisation is not fully understood, however there are convection currents within the system to stimulate the packing of droplets. In this research, the focus is to use PDMS cross-linking to replace a solvent evaporation technique, therefore convection currents and droplet motions are studied in PDMS. This will lead to the integration of cross-linking to trap a stabilised droplet, examined in Chapter 6.

5.2 The influence of spacing between printed drops

5.2.1 Drop spacing introduction

Coalescence events happen regularly in the BF method unless there is significant presence of a polymer within the solution. This is especially observed when there is a rapid growth (i.e. high relative humidity), or a high concentration of droplets. Droplets of the same content tend to coalesce naturally upon direct contact with each other. In the BF method, as introduced in Chapter 2, there is a time scale where the droplets grow rapidly by coalescence, which makes the control of the size of the final pore more difficult. Positioning of droplets by condensation is not controllable while with inkjet technique the deposition of droplets is more precise, then the spacing between the droplets is easily manipulated. The investigation into the spacing between the droplets to prevent coalescence can guarantee the size of droplets to be almost exactly the same. While programming inkjet printing, one of the set conditions is the distance between each droplet. Assuming the diameters of the droplets are the same, if the distance between two droplets is no larger than the diameter of the droplet they will make contact with each other. Contact of drops during printing on solid surfaces is key to initiate coalescence and create controlled features, whereas when printing onto a liquid it is expected to increase the volume of the final drop/pore. Figure 5.1 showed a line of 50 wt. % glycerol/water solution printed onto vegetable oil using a MicroFab (B12-80-01 and B12-80-02) 80 μm nozzle.

This was printed with the Fisnar robot testing system, set at a fixed printing frequency and movement speed of the nozzle holder, which means a fixed distance between each drop. This imaging setup shows the droplets and also behind them the nozzle from which they were printed. It showed some coalescence happened, but most of the droplets kept separate. This initial trial with the movement speed of the nozzle and the frequency of printing both set,

showed that most droplets remained separate while occasionally some coalesced. This provided sufficient evidence that there is a concern that when multiple droplets are printed continuously, the contact during printing can induce coalescence, therefore to make sure droplets remain separate after printing and give a highly controllable system, the unequivocal range of droplet spacing to prevent coalescence is essential to be well-defined.

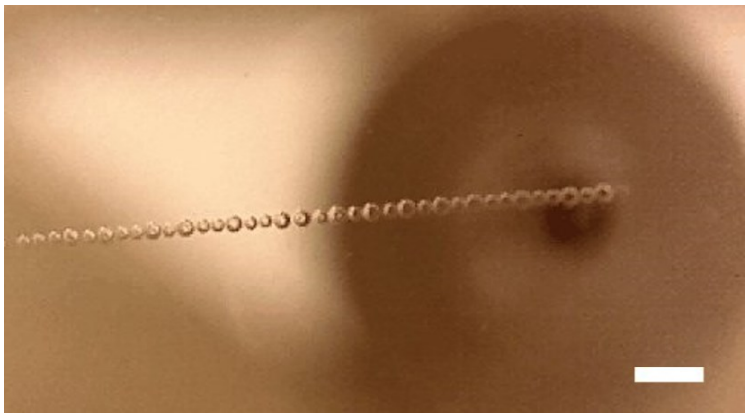

Figure 5.1 A line of drops printed with 50 % mass fraction glycerol water solution on vegetable oil using the Fisnar robot testing system. Larger drops all formed by coalescence. Drops are generated from an 80 μm sized orifice. Scale bar 500 μm.

5.2.2 Drop spacing: theory and method

The initial test described above was developed further to test whether there is a certain thresholding of distance preventing droplets from coalescing. 50 wt. % GW droplets were printed onto vegetable oil at room temperature using 80 μm MicroFab nozzles, as 50 wt. % GW has the most regular printing performance. The process of the experiments is illustrated in Figure 5.2, with one drop printed onto the substrate first without high speed image capturing, then the distance was adjusted manually by using the mounting system and changing the substrate stage displacement in the x-direction (refer to Figure 3.3). Afterwards, the external trigger was used to fire the second drop and to give the camera the command to capture the performance of the second drop. The imaging will identify if the two droplets either coalesce into one drop or stay separate as two drops. Statistics are challenging to build up due to the natural motion of the fluids during imaging, because the viscosity of the octyl acetate is very low that is difficult to hold the droplets at the same position.

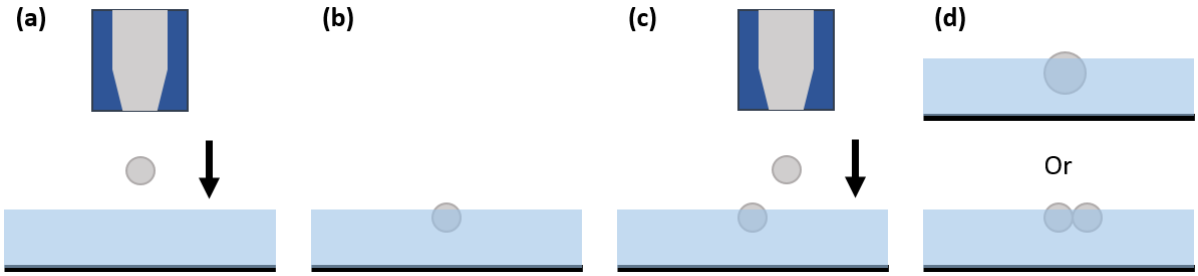

Figure 5.2 Schematic graph of drop spacing study. (a) Print the first drop onto the substrate. (b) Wait for the drop to set steady. (c) Move the substrate and print the second drop at the mean time capture the video of the second drop. (d) Two droplets coalesce into a larger drop or separate into individual droplets on the substrate.

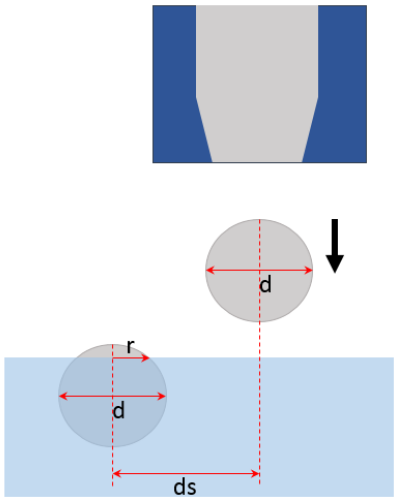

Figure 5.3 Schematic graph of the definition of relative distance. The diameter of the drop is d, the radius of the 'cap' above the substrate surface is r., the distance between the two drops is ds, and the relative distance is dr, which equals to ds divided by d.

Then the relationship between the droplets behaviours at contact (coalescence or separation) and the relative distance were examined. As demonstrated in Figure 5.3, the relative distance (dr) is the centre-to-centre distance between two drops (ds) over the diameter (d) of the drop.

$$dr = \frac{ds}{d} \quad (5.1)$$

Hence, when the relative distance is less than 1, the droplets are touching each other, while dr greater than 1 indicates that the droplets are contact-free. The assumption is that the diameters

of the droplets are the same. This is validated through the initial setup of the inkjet printing and ensuring a stable droplet is created. As noted in Chapter 4, the impact of a droplet on vegetable oil and PDMS does not form ripples, however on octyl acetate this is not the case and time was given prior to the second printing event to allow the surface to recover. Therefore the assumption is made that the impact wave's effect on the behaviour of drop contact can be neglected.

5.2.3 Drop spacing: results and discussion

It is shown clearly in the previous chapter that when droplets stabilise at the substrate surface, there is a small peak of the drop left above the surface, the cap is formed by a surface tension effect. This is considered closely related to the space between the drops to keep them separate. Therefore a hypothesis was made that the droplets that are printed will either hit the cap of the first drop, or the submerged part of the drop and it is anticipated that there will be a range of behaviours that may be linked to these geometries.

Stability of glycerol/water droplets on vegetable oil

The distance between the centres of two droplets, which can keep them separate was examined. Videos were captured using the drop-on-demand single nozzle high-speed imaging system using the method mentioned in the theory. When two drops were printed onto the vegetable oil in sequence, at the range of spacings noted above, there were two different states after contact. Figure 5.4 shows droplets that are sufficiently close to have experienced impact after printing, but remain separated and Figure 5.5 shows the process of droplet coalescence.

In Figure 5.4 (a), the droplet in the oil is steady at the air/oil interface due to surface tension effect. According to Figure 5.4 (a) and (b), it is quite obvious that the second drop collides with the drop under the substrate surface, and because of the existence of a layer of oil as lubricant, the second drop slides to the side and pushes the first drop. Compare Figure 5.4 (b) and (d), the position of the first drop changes slightly, illustrating this force. From calculations in the system shown in Figure 5.4 (b), the second drop did not hit the cap of the first drop.

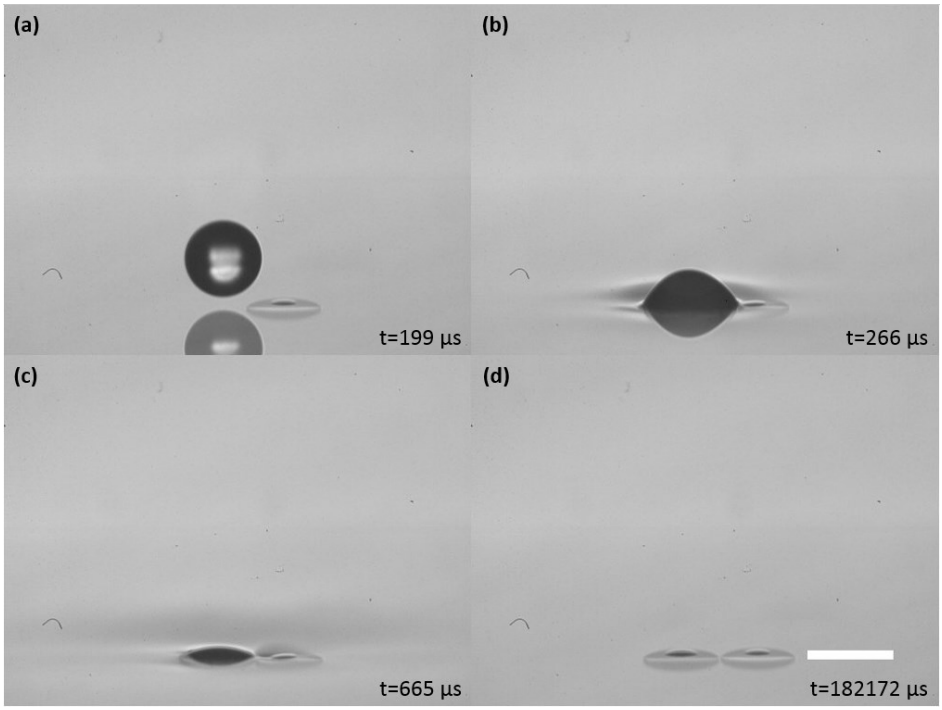

Figure 5.4 Two drops separation on vegetable oil surface. (a) One drop on the surface already, a second drop was printed. (b) The second drop impact on the surface. (c) The second drop submerged into the substrate. (d) Two drops kept separate. The time in the images is the time in the video. Scale bar 100 µm.

Figure 5.5 shows the collision of two droplets in the same system but at a closer spacing and the resulting coalescence. Figure 5.5 (b), (c), and (d) reveal the process of coalescence, when the second drop hits the first drop, it gradually coalesces with the first drop and is dragged by the first drop to form a larger drop at the original position. Comparing the process of coalescence and separation, the distance between the two droplets (ds) in Figure 5.4 is greater than that in Figure 5.5. Also in Figure 5.4 (a), the second drop hit the first drop on the edge which is covered by a layer of vegetable oil, while in Figure 5.5 (a), the second drop makes contact with the cap of the first drop that is above the substrate. As this cap is protruding from the oil surface, it is very likely that there is no significant oil layer to help prevent coalescence.

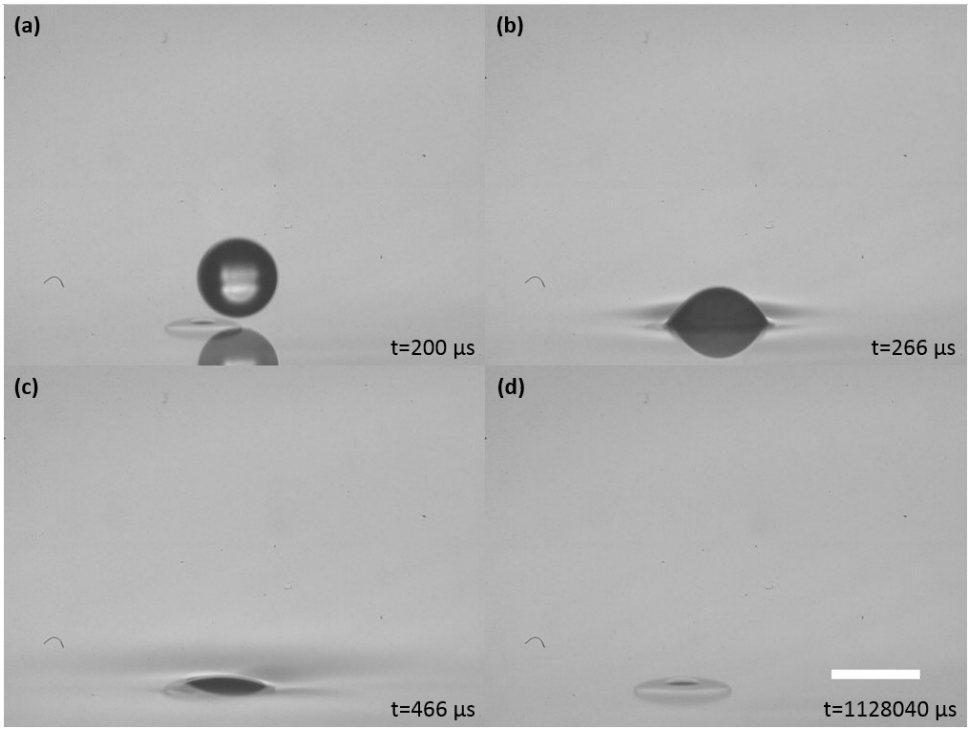

Figure 5.5 Two drops coalescence on vegetable oil surface. (a) One drop on the surface already, a second drop was printed. (b) The second drop impacts on the surface. (c) The second drop submerges into the substrate. (d) Two drops coalesce. The time in the images is the time in the video. Scale bar 100 µm.

It is hypothesised that the droplets that hit the 'cap' of the first drop above the surface will coalesce while those ones did not hit the 'cap' stayed separate. According to chapter 4 and Figure 5.3, the average value of 2r/d on this oil is 0.32 ± 0.03. A threshold value to avoid contact between the drops is defined as ds'_{oil}. When $ds'_{oil} \geq d/2+r$, two droplets are contact-free. Defining another threshold value dr'_{oil} as the relative distance for two-drop separation on vegetable oil:

$$dr'_{oil} = \frac{ds'_{oil}}{d}$$

$$dr'_{oil} = \frac{\frac{d}{2} + r}{d}$$

$$= \frac{0.5d + 0.16d}{d}$$

$$= 0.66 \pm 0.03$$

The size of the 'cap' is related to the surface tension of both the drop content and the substrates, therefore this relative distance to keep droplet separate is also dependent on the surface tension and so will change for each different liquid. To test the hypothesis, the range of different spacing were carried out. This requires significant numbers of repeats to enable capturing of the drops at sufficient sharpness to allow measurement and to cover the range of spacing required. The results are shown in Figure 5.6.

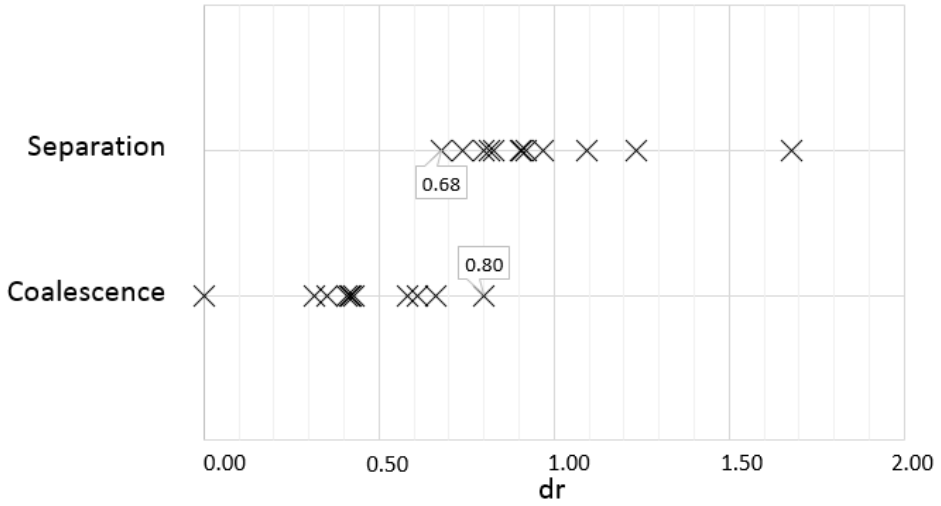

Figure 5.6 50 % GW droplets printed to vegetable oil at a range of drop spacing.

According to Figure 5.5, Figure 5.6 and the calculations, both the observed dr value and the calculated values for two drop to keep separate on this vegetable oil are less than 1, which specifies that the droplets can still separate after contact. Figure 5.6 demonstrates the results for drop separation on vegetable oil, regarding the relative distance with the corresponding contact behaviours, there is a region between 0.68 and 0.80 where the behaviour of the droplets is difficult to define, as both separation and coalescence can be observed within this range of dr. The calculated value is 0.66 ± 0.03, which is slightly smaller than the measured value of 0.68. This is not a huge deviation, so it is considered the transaction region where both coalescence and separation can happen is between 0.66 and 0.80, also separations can happen when the relative distance reaches 0.66.

Stability of glycerol/water droplets on octyl acetate

As with Chapter 4, a detailed study was carried out with octyl acetate as a good comparison with the solvents used in the BF method. When droplets were printed onto octyl acetate, similar observations were obtained. Droplets could remain separate after collision, which is demonstrated in Figure 5.7. Due to the low viscosity of octyl acetate, also shown in the previous chapter, the collision of droplets upon octyl acetate can form ripples. By allowing time for ripple dissipation, there is no significant effect of the ripples on the coalescence of droplets.

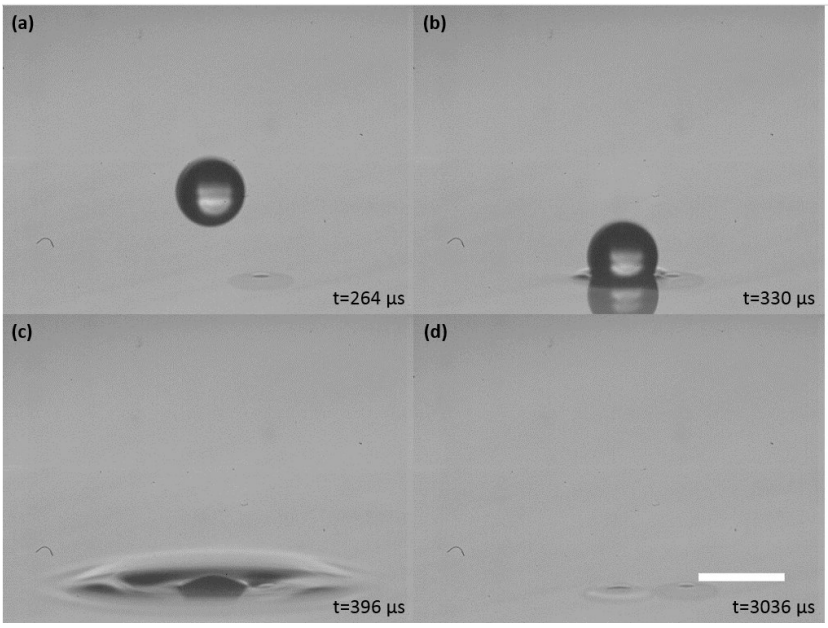

Figure 5.7 Two drops separation on octyl acetate. (a) One drop on the surface already, a second drop was printed. (b) The second drop impact on the surface. (c) The second drop submerged into the substrate. (d) Two drops kept separate. The time in the images is the time in the video. Scale bar 100 µm.

The average value of the diameter at the interface divided by the diameter of the whole drop for octyl acetate is 2r/d = 0.30 ± 0.05.

$$dr'_{OA} = \frac{dr'_{OA}}{d}$$

$$dr'_{OA} = \frac{\frac{d}{2} + r}{d}$$

$$= \frac{0.5d + 0.15d}{d}$$

$$= 0.65 \pm 0.05$$

The same phenomena as before can be seen when the droplets contact the substrate in Figure 5.7 and Figure 5.8. Coalescence can occur at a distance where the droplets contact the 'cap' and separation is due to the lubricate layer of the substrate owing to wetting.

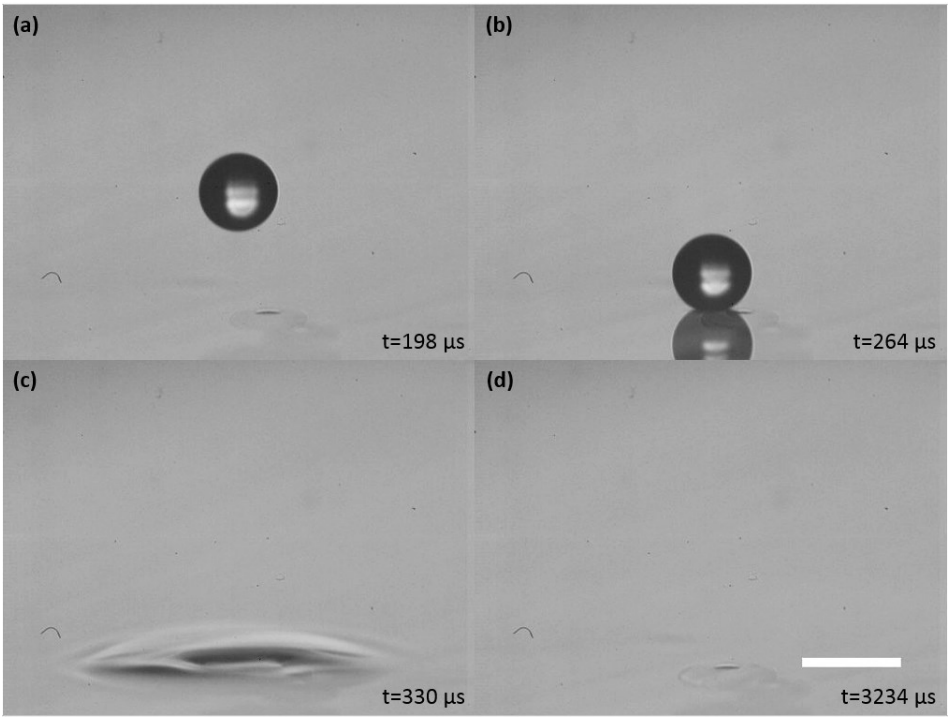

Figure 5.8 Two drops coalescence on octyl acetate surface. (a) One drop on the surface already, a second drop was printed. (b) The second drop impact on the surface. (c) The second drop submerged into the substrate. (d) Two drops coalesced. The time in the images is the time in the video. Scale bar 100 µm.

A series of experiments at a range of spacing was also carried out for octyl acetate surfaces. This is particularly challenging because of the low viscosity and evaporation leading to convection currents. Droplets were often no longer in the original position upon printing the second drop. Because of the importance of ensuring the correct spacing for rigorous conclusions, data is only included where significant moving has not occurred. The measured results are illustrated in Figure 5.9. The separation threshold could not be defined to a greater

level of accuracy because of the droplets drifting on the octyl acetate surface. It is shown that the region of uncertainty regarding coalescence is from 0.57 to 0.71. The region of relative distance for separation from the calculation is around 0.65 ± 0.05, which is in between this interval where the coalescence could happen, again supporting the hypothesis.

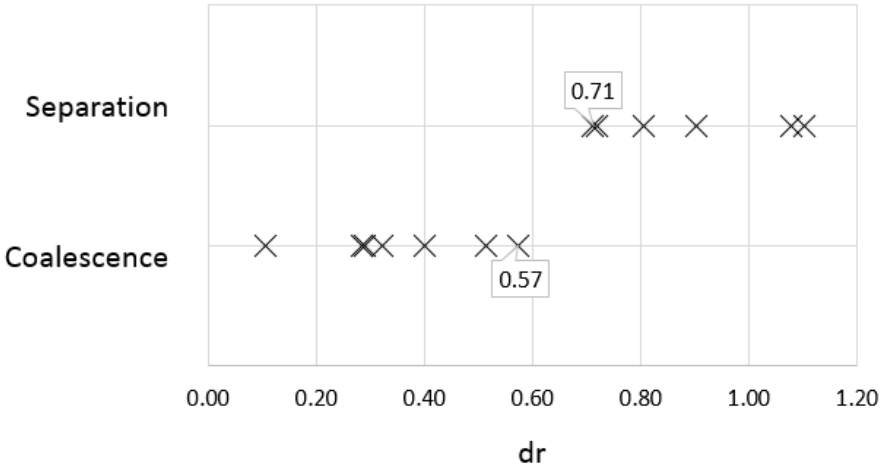

Figure 5.9 Relative distance change from coalescence to separation of 50 % GW on octyl acetate.

One additional phenomenon was observed when working with octyl acetate, that of delayed coalescence. As shown in Figure 5.10, two droplets were printed and settled separately at the interface after contact during printing, but after a time delay they still coalesced. This phenomenon was only observed once, and could be due to an instability or contamination between the drops promoting coalescence. However, it shows that close packing will be problematic to achieve through printing droplets close together.

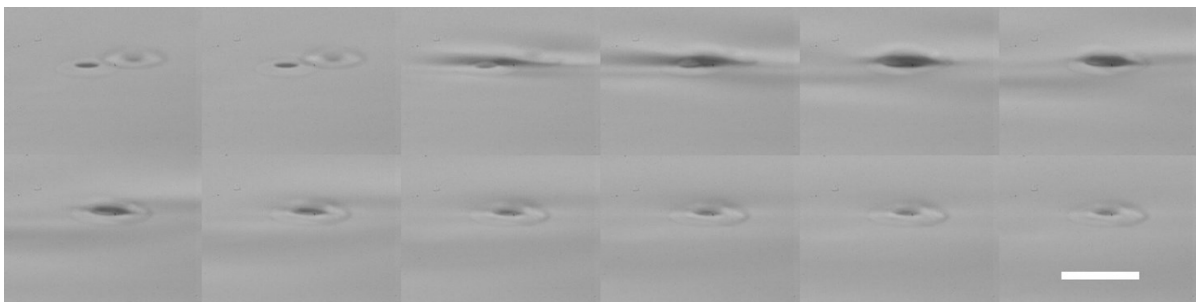

Figure 5.10 Two droplets at octyl acetate/air interface coalesced into one single drop. Frame interval 87 μs. Scale bar 100 μm.

Stability of glycerol/water droplets on PDMS

It was noted previously that it would be a breakthrough to move the BF technique away from evaporation-based formation and towards a cross-linking chemistry. Drop impact on PDMS was therefore explored but is quite different from the behaviour on octyl acetate and oil, as the viscosity of PDMS is 3.3 Pa·s at 1 h curing time while that of octyl acetate is 0.0013 Pa·s. The impact of droplets on PDMS is shown in Chapter 4, which resembles impact on solid surfaces, as the droplet deforms after impact. With this high viscosity, it takes a much longer time for droplets to submerge into PDMS and as a result, as shown in Figure 5.11, when following standard experimental protocol, the two droplets printed to overlap slightly impact before either has submerged into the PDMS.

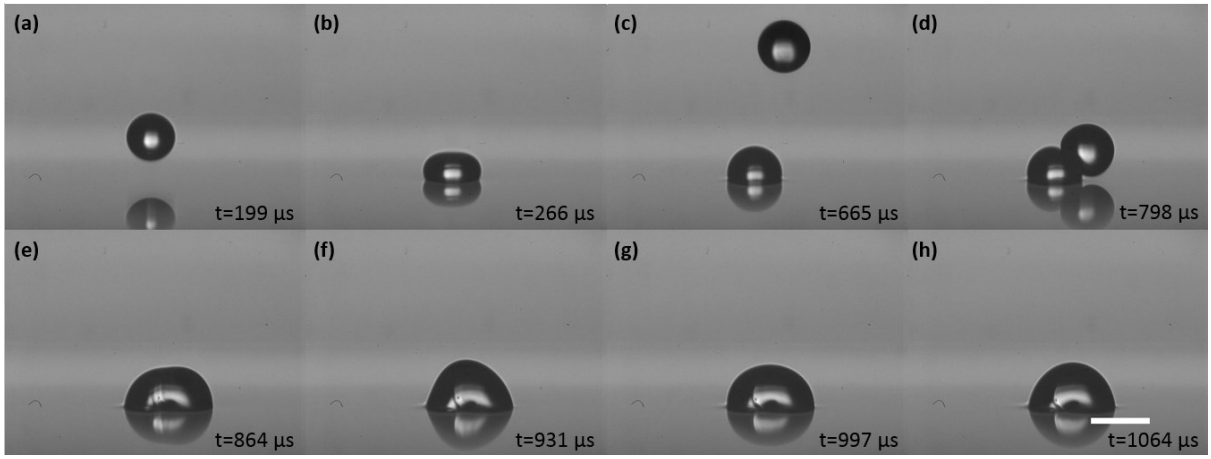

Figure 5.11 Two drops coalescence above PDMS surface. (a) First drop printed onto PDMS. (b) The first drop impact on the surface. (c) Second drop printed onto PDMS. (d) Second drop collided on the first drop. (e)-(h). Coalescence of droplets and gradually submerged into PDMS. The time in the images is the time in the video. Scale bar 100 µm.

Additional studies were carried out to identify the time at which the drops would submerge and be suitable for stability testing. It usually required 12.1 s for GW droplets after contact with PDMS surface to fully submerge into it and pin at the interface. Therefore for high-speed printing, the distance between the centres of the droplets should be designed carefully. As illustrated in Figure 5.12, with the change in timings to allow for robust results (print the second drop after the first one finally stabilised at the PDMS/air interface), two drops can still

experience non-coalescence after contact and remain steady as two single droplets at the PDMS/air interface.

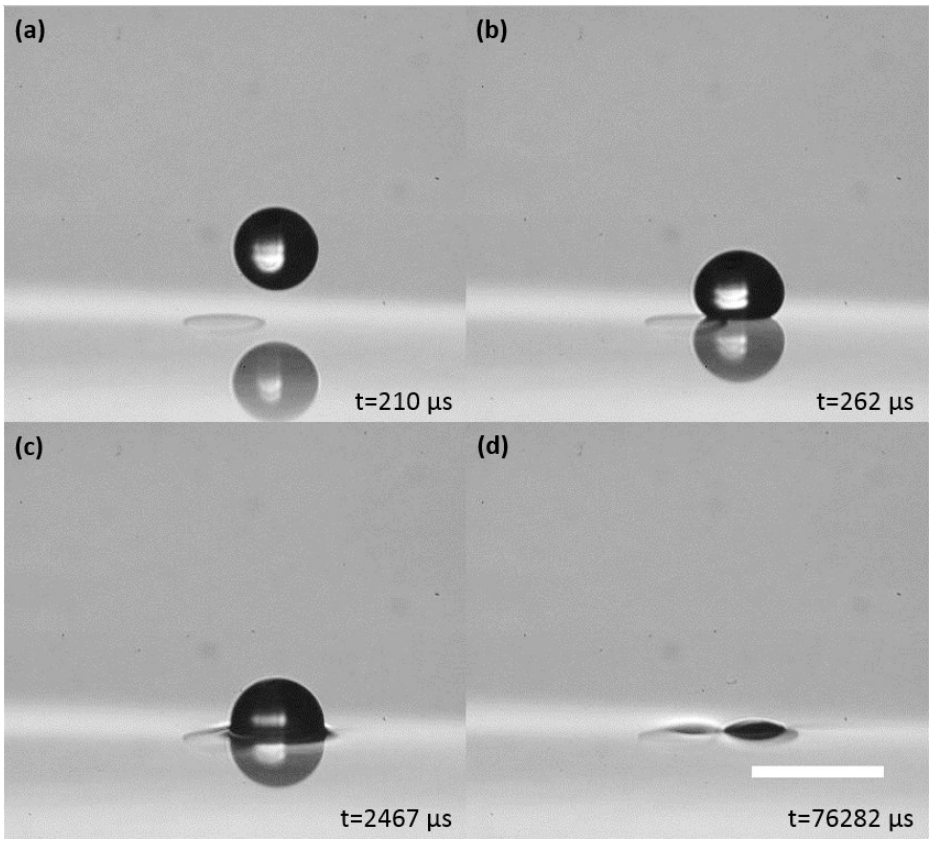

Figure 5.12 Two non-coalescing drops on PDMS. (a) One drop on the surface, a second drop was printed. (b) The second drop impacts on the surface. (c) The second drop submerges into the substrate. (d) Two drops remain separate. Scale bar 100 µm.

As with the work examining vegetable oil and octyl acetate, coalescence can occur when two drops contact each other. The same calculations can be carried out with PDMS as with previous liquid surfaces. The average value of 2r/d on PDMS is 0.12 ± 0.02.

$$dr'_{PDMS} = \frac{dr'_{PDMS}}{d}$$

$$dr'_{PDMS} = \frac{\frac{d}{2} + r}{d}$$

$$= \frac{0.5d + 0.06d}{d}$$

$$= 0.56 \pm 0.02$$

Compare this value with the measured region of separation/coalescence, which is demonstrated in Figure 5.14, between 0.53 and 0.58, it can also proof that the stability of two drops contact during printing is related to the contact angle of the droplets. An example of two droplets impacting and coalescing to give one drop is shown in Figure 5.13. From the calculation above, the level of overlap (due to the high contact angle) is very significant and it is challenging to print to the correct position to drive coalescence.

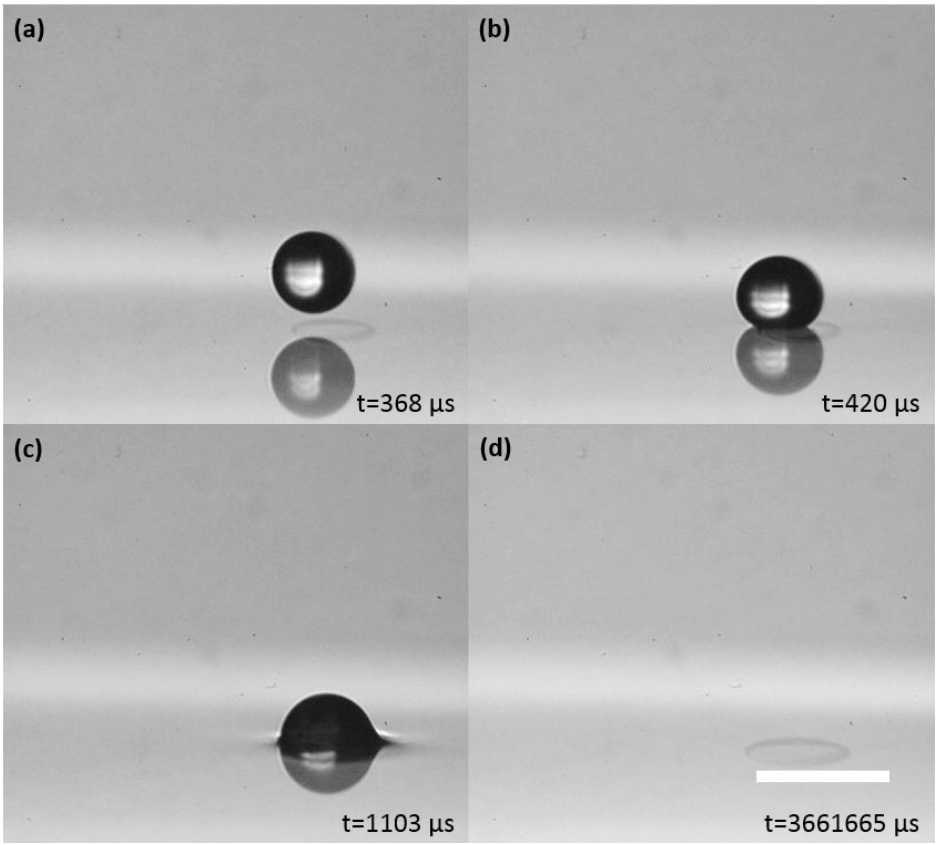

Figure 5.13 Two drops coalescence on PDMS. (a) One drop on the surface already, a second drop was printed. (b) The second drop impact on the surface. (c) The second drop submerged into the substrate. (d) Two drops coalesced. The time in the images is the time in the video. Scale bar 100 µm.

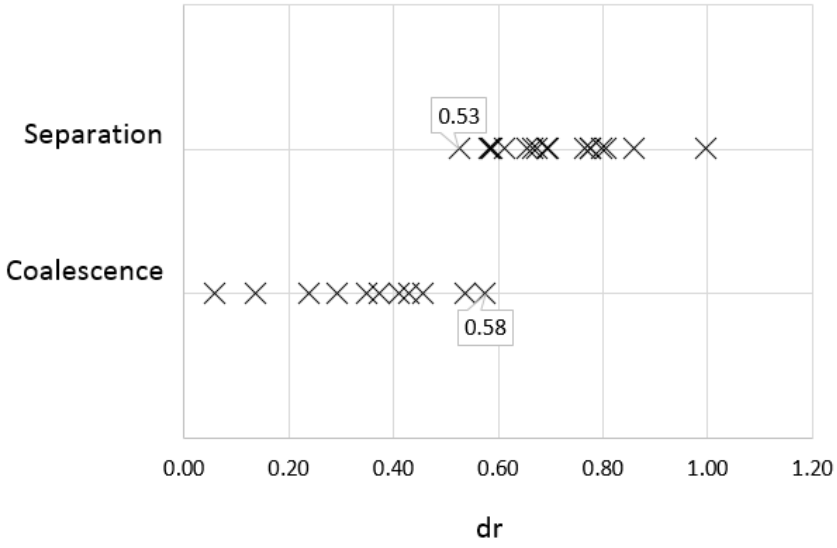

Figure 5.14 Relative distance change from coalescence to separation of 50 % GW on PDMS.

The relative distance to keep droplets separate on octyl acetate is around 0.65 ± 0.05, while the dr required for PDMS is 0.56 ± 0.02, which is slightly less than that of octyl acetate due to the high contact angle at which the drops settle. In addition, the delayed coalescence after impact was not observed in any cases for PDMS.

5.2.4 Conclusions: Drop spacing influence on stability of droplets on liquids

It is concluded from the experiments controlling droplet spacing and observing the drop coalescence behaviour that a stable separation can be created by avoiding contact with the 'cap' of the droplet above the substrate surface due to surface tension effect. There is a region of ambiguous behaviour where both separation and coalescence can happen and so the guidelines for targeting a particular behaviour also include a guidance as to the safety factor for the separation. The region of uncertainty is defined with the aforementioned relative distance which is the ratio of the centre-to-centre distance of the two droplets to the diameter of the droplet. The measured region for 50 % GW droplets on vegetable oil is between 0.68 and 0.80. For octyl acetate as the substrate, the region is around 0.51-0.71, however due to the drifting of droplets on the octyl acetate surface, within this region, overlap did not witnessed. On PDMS, which is the most stable substrate, there is a narrow region of 0.53-0.58. This region is closely related to the surface tension because it is linked the size of the 'cap' above the substrate. The threshold dr values were calculated using the average 'cap' size above each

substrate, the results showed that for these high contact angle liquid-liquid system, the distance required for droplets to stay separate is only slightly larger than 0.5 as the radius of the 'cap' is small. Value of dr'_{oil} is 0.66 ± 0.03, dr'_{OA} is 0.65 ± 0.05, and dr'_{PDMS} is 0.56 ± 0.02. This shows that there is an opportunity to print droplets directly to PDMS with a small drop-to-drop spacing and still avoid significant coalescence. However, due to the noise, it is also correct to conclude there will be regular defects. Printing droplets for templating will be further explored in Chapter 6 however, it is examined further here how to bring the droplets together after printing with a safe separation to avoid any coalescence.

5.3 Drop self-organisation by convection on liquid surfaces

5.3.1 Drop self-organisation by convection introduction

In the BF method, droplets can self-organise under the Marangoni effect, which is discussed in Chapter 2. Water droplets can coalesce when there is a high concentration of droplets at the solution surface, while with inkjet printing droplets can remain steady at the solution interface if they are not contacting each other, achieved by controlling the space between each drop. While the BF method relies upon solvent evaporation to drive a temperature gradient and the resulting convection, with PDMS we can provide some heat to the bottom of the sample to induce some convection in the system to drive self-organisation. As discussed in the previous section, the distance between droplets is crucial for droplets to stay separate, therefore droplets in this section are printed at a significant distance and are driven closer into hexagonal arrays. Droplets were generated by the DMP, and the convection was captured by the convection imaging system introduced in Chapter 3.

5.3.2 Drop self-organisation by convection: visualisation of convection

Convection is the fluid motion caused by temperature difference. In 1900, Bénard first investigated the convection current happening in a thin fluid layer with heating applied below. This type of convection occurred in a horizontal plane of shallow fluid layer heated from below, known as Rayleigh- Bénard convection. In Bénard's experiments, a fluid of free surface was chosen to observe the convection, the fluid for steady-state was spermaceti, which is rigid under room temperature, non-volatile, viscous fluid of poor thermal conductivity, melts at 46 °C

[107]. Then the layer was heated at 100 °C from below, and the surface was exposed in ambient temperature (not uniform cooling), which was assumed at 20 °C, then the temperature difference cross the layer in vertical direction was 80 °C. The primary results from Bénard's investigations were the presence of stable hexagonal convection cells of regular patterns, which are called Bénard cells, and have long been associated with the BF method.

To study the convection current, a range of materials were attempted to add to a small container containing the PDMS. The most stable option was solvent blue 35 used to dye a separate supply of PDMS. This dyed solution was deposited by ultra-sharp tip to the surface of PDMS in a range of patterns to help identify when convection has occurred. These patterns are shown in Figure 5.15. The white plastic square weighing boats (Sigma-Aldrich, USA) were used for PDMS convection and patterning studies. The size of it is 43 mm × 43 mm × 9 mm, with round edges at the bottom. Fill the weighing boat with approximately 5 ml of PDMS with a syringe and degas with a pump (as introduced in Chapter 3), then print droplets onto it with DMP and finally heat up at 80 °C on a hot plate can capture the video with the convection imaging system. Figure 5.15 (a)-(c) are the random patterns to help visualise convection, and (d)-(f) are the patterns after convection.

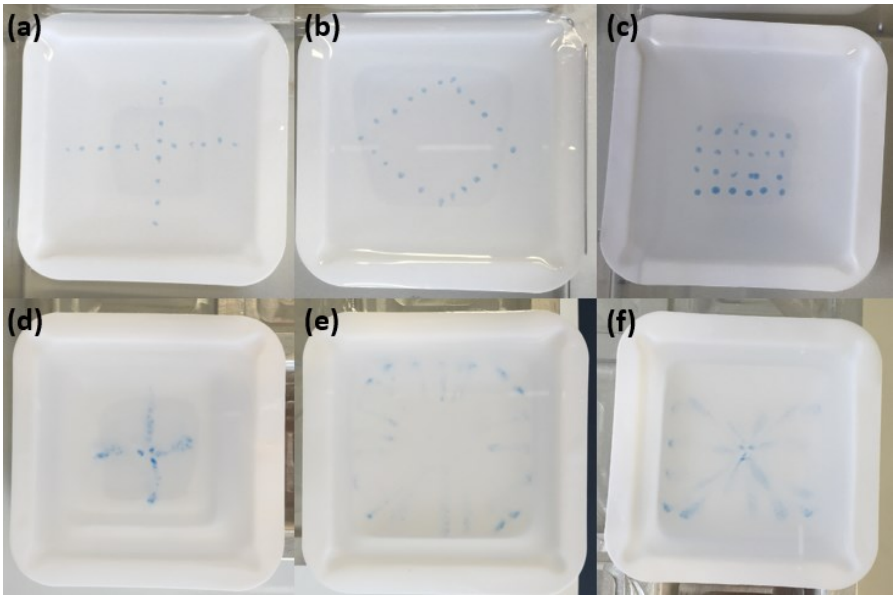

Figure 5.15 Convection visualisation using solvent blue 35 dyed PDMS. (a) Cross pattern. (b) Diamond pattern. (c) Arrays of dots pattern. (d)-(f) The pattern of (a)-(c) after convection.

The details of the convection results are demonstrated in Figure 5.16, Figure 5.17 and Figure 5.18. As revealed in Figure 5.16 and Figure 5.15 (d), the convection of cross patterns showed a contraction of the whole pattern into the centre of the weighing boat, from Figure 5.16 (a) to (b), while in Figure 5.16 (c) and (d) the pattern starts to stretch to the outer edges of the container.

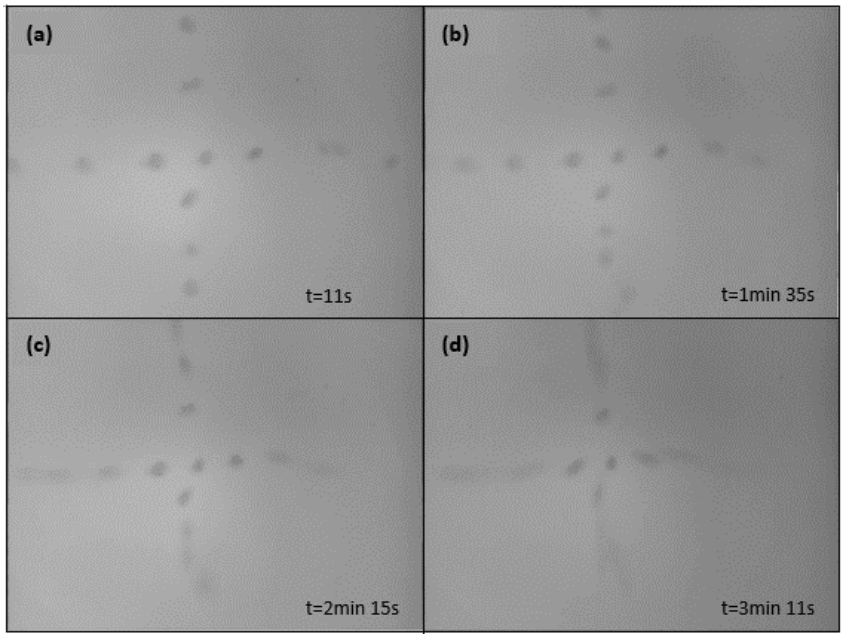

Figure 5.16 Convection visualisation for the cross pattern by heating on hot plate at 80 °C.

According to Figure 5.17, the diamond pattern followed a similar track to the cross pattern, as the whole pattern 'shrunk' to the centre from Figure 5.17 (a) to (d) in 2 min 30 s first, then formed a radial pattern and spread to the edge direction, which is clearly shown in (e)-(f). In addition, the original diamond pattern finally changed to a symmetric round shaped pattern after convection, which mean the velocity at the lateral direction may be the same as that at diagonal direction. Figure 5.15 (e) is the pattern left after the convection, it is more obvious than Figure 5.15 (d) that the dyed radial PDMS is now under the surface, therefore the convection current under the surface is expanding to the edge, while the current at the PDMS/air interface is towards the centre of the container.

The dot arrays aim to simulate what could be convection's effect on droplets arrays packing on PDMS, but the performance is different from droplets because it can be destabilised into streaks

of dye in contrast to the droplets, which each can hold as one single bead without any spread of the liquid. Figure 5.18 demonstrates the convection pattern formed for the dot array pattern, in the first 1 min, the pattern shrunk and kept the original shape, it is manifest that those close to the centre did not move a lot in the convection, and then in Figure 5.18 (c), the pattern further shrunk to the centre and the edge started to stretch out, which again proof that the convection in the weighing boat is contracting to the centre at the surface and radial expanding from the entre under the surface.

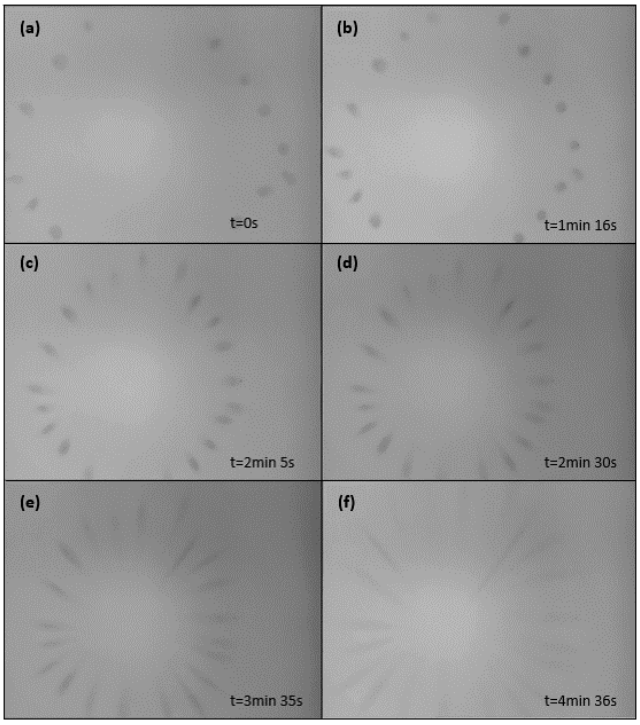

Figure 5.17 Convection visualisation for the diamond pattern by heating on hot plate at 80 °C.

Then from these observations, the convection happened within the weighing boat can be predicted. As can be seen from Figure 5.19, the blue lines with arrows characterise the convection current and the red ones represent the heating. The convection current on the surface is contracting to the centre of the weighing boat, however all the parts under the surface is drawing to the bottom and circling to the edge of the container. Then the current ascend at the edges and in the middle descending, thus for convections at high temperature the droplets were dragged into the PDMS formed a tornado shape connecting the bottom and the surface of PDMS.

The speed of the convection is not necessary for this system, the qualitative visualisation of the convection made it clear that the convection current can help droplets to pack. The behaviour of the dyed PDMS on PDMS surface still very different from the behaviour of the droplets packing on PDMS, as droplets are less infected by the random movement within PDMS, and can self-organise when they interact with each other. Therefore the convection with droplets printed on PDMS was studied and the results are in the next section.

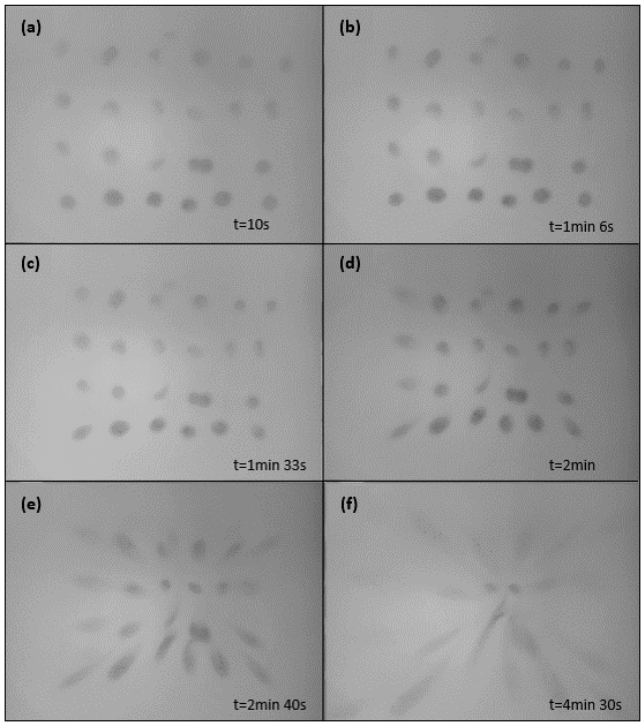

Figure 5.18 Convection visualisation for the arrays of dots pattern by heating on hot plate at 80 °C.

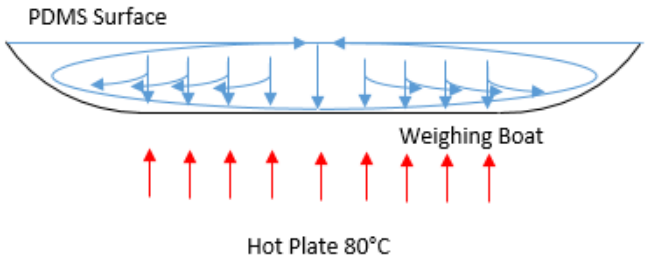

Figure 5.19 The cross-sectional schematic diagram of hypothetical convection model within the weighing boat of PDMS heating on hot plate at 80 °C.

5.3.3 Drop self-organisation by convection: droplets packing

As introduced in previous section, the convection at the PDMS/air interface tends to constrict the central portion of the surface towards the centre of the weighing boat. In the middle, the convection current descends and transfers to the outer edge ascending again to the surface. Therefore the convection current can drive the droplets closer to each other when the pattern is almost rotational symmetry to the centre of the weighing boat.

Using the imaging setup described in section 3.2.4 the convection imaging system and printing with the DMP with a drop to drop spacing of 50 μm, GW drops were printed onto the surface of the PDMS within the weighing boat. Drops were targeted at the central region, where the convection would converge inwards and drive self-organisation. Convection was driven initially by an arbitrary increase in the temperature of the PDMS by heating from below to 80 °C. The pattern printed is always 10 mm × 10 mm droplets arrays with either cubic or hexagonal arrangements.

Convection pattern study: 50 % GW on PDMS

Initially, inkjet printed drops were deposited in a square array pattern. This is the default option for inkjet printing when printing a pattern. At 50 μm spacing, the droplets are far from overlapping within the substrate. The square arrays are shown in Figure 5.20 (a). Once the temperature is increased, the convection currents begin and the droplets start to reduce their spacing. The pattern in Figure 5.20 (b) reveals that the packing structure is mixed. While some of the drops are hexagonally packed, there are clusters in different orientations and there are many dislocations to this packing order. From observations, the droplets retain their square packing structure as they approach each other and then try to flow to meet maximum packing density once they are in contact. As introduced in Chapter 2, in BF the natural self-organisation of droplets usually form hexagonal close packed pattern, thus in order to acquire a higher level of ordering, the droplets were printed into hexagonal arrangements initially, all with the same centre-to-centre distance, as shown in Figure 5.20 (c). With a repeat of many experiments, it was seen in all cases that the droplets retain their hexagonal pattern as they approach each other with the self-organisation process and eventually form a highly repeatable pattern which is shown in Figure 5.20 (b).

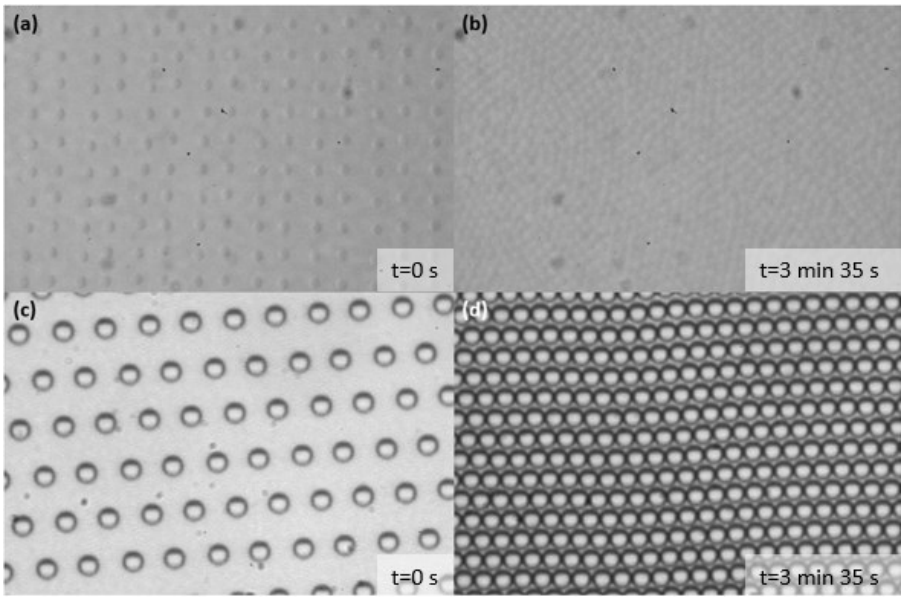

Figure 5.20 Cubic array self-organisation and hexagonal array self-organisation. (a) Cubic before self-organisation. (b) Cubic after self-organisation. (c) Hexagonal before self-organisation. (d) Hexagonal after self-organisation. Droplet size is approximately 20 μm in all images.

The pattern formed can be seen to have a slight curvature when compared with the ideal scenario, but overall gives a 'single crystal' packing throughout, in that there is only one domain of ordering. This is impossible to achieve over these large lengthscales using the BF technique and so represents a major step forward in patterning. It was observed that the temperature applied to the PDMS was important, in that a high temperature sometimes led to a failure of the system to pack and instead the droplets were dragged into the bulk of the fluid by convection. As a result, a more detailed study was carried out to examine firstly a range of different temperatures to drive convection, and secondly by adding a cross-linking agent to the PDMS, a range of different times allowed for cross-linking to occur.

Convection temperature study: constant 1 h curing time, different temperatures

In 1916, based on the results from the Bénard, Lord Rayleigh again pioneered the development of the theory of convection occurring with heating applied from the bottom [108], and showed that the convection only happens when the Rayleigh number (R), which was first introduced by Sutton in 1950 [109], is larger than a critical value. The Rayleigh number is defined as:

$$R = \frac{\varepsilon g \Delta T d^3}{\upsilon \kappa} \quad (5.2)$$

Where ε is the volume expansion coefficient, g is the acceleration due to gravity, ΔT is the temperature difference between the surface and the bottom of the fluid, ν is the kinematic viscosity, κ is the thermal diffusivity. The Rayleigh number is a non-dimensional measurement of the vertical temperature gradient applied to a fluid layer. For PDMS, $\varepsilon = 9.6 \times 10^{-4}$ °C^{-1} for high temperature change, and for small temperature change $\varepsilon = 3.2 \times 10^{-4}$ °C^{-1} [110]. η= 5.1 Pa·s for the base and 3.5 Pa·s after mixed with the cross-linker, $\nu = \eta/\rho$, $\rho \approx 1030$ kg/m^3. κ = $10.8 \pm 0.04 \times 10^{-4}$ cm^2/s [111].

There is a critical Rayleigh number (Rc = 1100.7 for rigid-free liquid layer) for convection to happen, which by definition of the Rayleigh number, represents the critical value of the difference in temperature for a fluid perturbation happens at a wave number at the margin, where instable state is verging [107].

Droplet self-organisation on PDMS surface under different temperatures at 1 h after PDMS was sampled were examined. The same hexagonal pattern was printed onto PDMS samples, and then the peltier heater was heated to different temperatures. Figure 5.21 demonstrates the time required for the convection current at different temperature to pack droplets together. Figure 5.21 (a) is the 25 °C which is slightly higher than room temperature. This is explored further in Chapter 6 but it is found that this does not provide enough energy for droplets to close pack. In addition, lower heating temperature required a much longer time for the droplets to self-organise. Figure 5.21 (b) is at 40 °C, can as the time shown, and the time for droplets to pack reduced significantly from 19 min 58 s to 3 min 16 s. For higher temperature of 60 °C and 80 °C in Figure 5.21 (c) and (d) the time is further decreased, but from 60 °C, the time is almost the same.

Assuming room temperature above the PDMS surface, which is 20 °C, therefore the following calculations are done for 25 °C, 40 °C, 60 °C, and 80 °C:

$$R_{25} = \frac{3.2 \times 10^{-4} \times 9.8 \times (25 - 20) \times 0.009^3}{3.5 \div 1030 \times 10.8 \times 10^{-8}} = 31.1$$

$$R_{40} = \frac{3.2 \times 10^{-4} \times 9.8 \times (40 - 20) \times 0.009^3}{3.5 \div 1030 \times 10.8 \times 10^{-8}} = 124.6$$

$$R_{60} = \frac{3.2 \times 10^{-4} \times 9.8 \times (60 - 20) \times 0.009^3}{3.5 \div 1030 \times 10.8 \times 10^{-8}} = 249.2$$

$$R_{80} = \frac{3.2 \times 10^{-4} \times 9.8 \times (80 - 20) \times 0.009^3}{3.5 \div 1030 \times 10.8 \times 10^{-8}} = 373.8$$

When Rc = 1100.7

$$\Delta T = \frac{1100.7 \times 3.5 \div 1030 \times 10.8 \times 10^{-8}}{3.5 \times 10^{-4} \times 9.8 \times 0.009^3} = 166.2\ ^\circ C$$

Therefore over 166.2 °C temperature difference, pure thermal convection happened, and all the convection in this research was affected by buoyancy.

Convection curing time study: 80 °C heating, different curing times

In this research, it is also witnessed that the self-organisation of droplets on PDDMS can be influenced by the curing time of PDMS under room temperature. After PDMS is mixed with the cross-linking agent, it starts to cure and increase surface tension as well as the viscosity, where the viscosity is more important in convection, the detailed rheology studies are revealed in Chapter 6 as part of the section on droplet templating. As Figure 5.22 illustrates, the more time PDMS left cured the more time required for droplet packing. For 4 h curing time, the time required is only 1 min 57 s to achieve the relatively close packed pattern, as the low temperature difference resulted in weak convection, while at 10 h curing time, the time for achieving the close packed pattern is increased to 3 min 20 s. Comparing the pattern after packing in Figure 5.22, it is also shown that at 10 h curing time, the pattern of droplets packing is more ordered than those for other curing times. In the next chapter, this curing time study is introduced in more detail regarding the curing time resulted more regular hexagonal pore arrangement, the capability of other arrangements, and change in pore shapes.

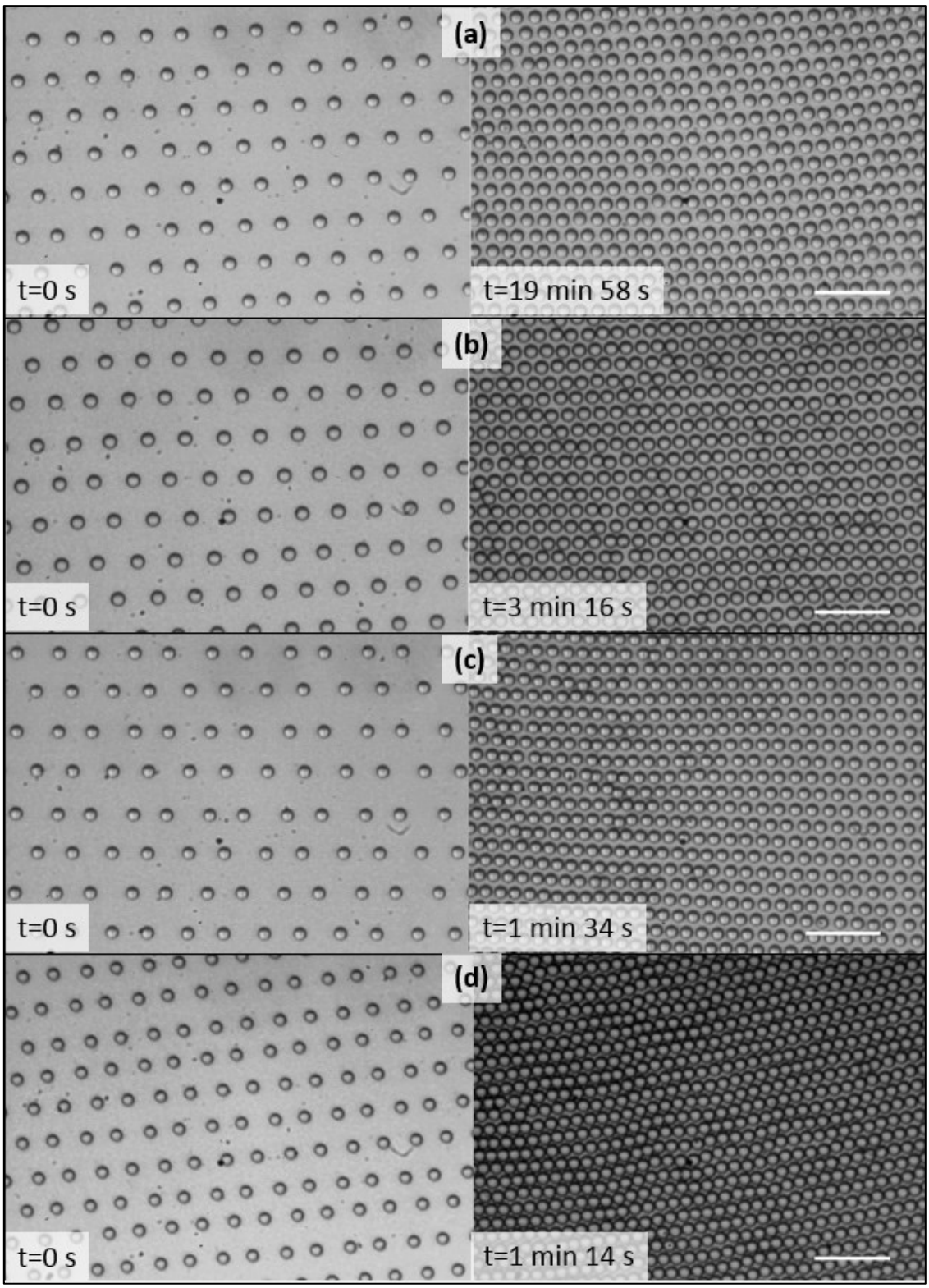

Figure 5.21 Convection at 1 h curing time for different temperatures. (a) 25 °C. (b) 40 °C. (c) 60 °C. (d) 80 °C. Scale bar 100 μm in all the images.

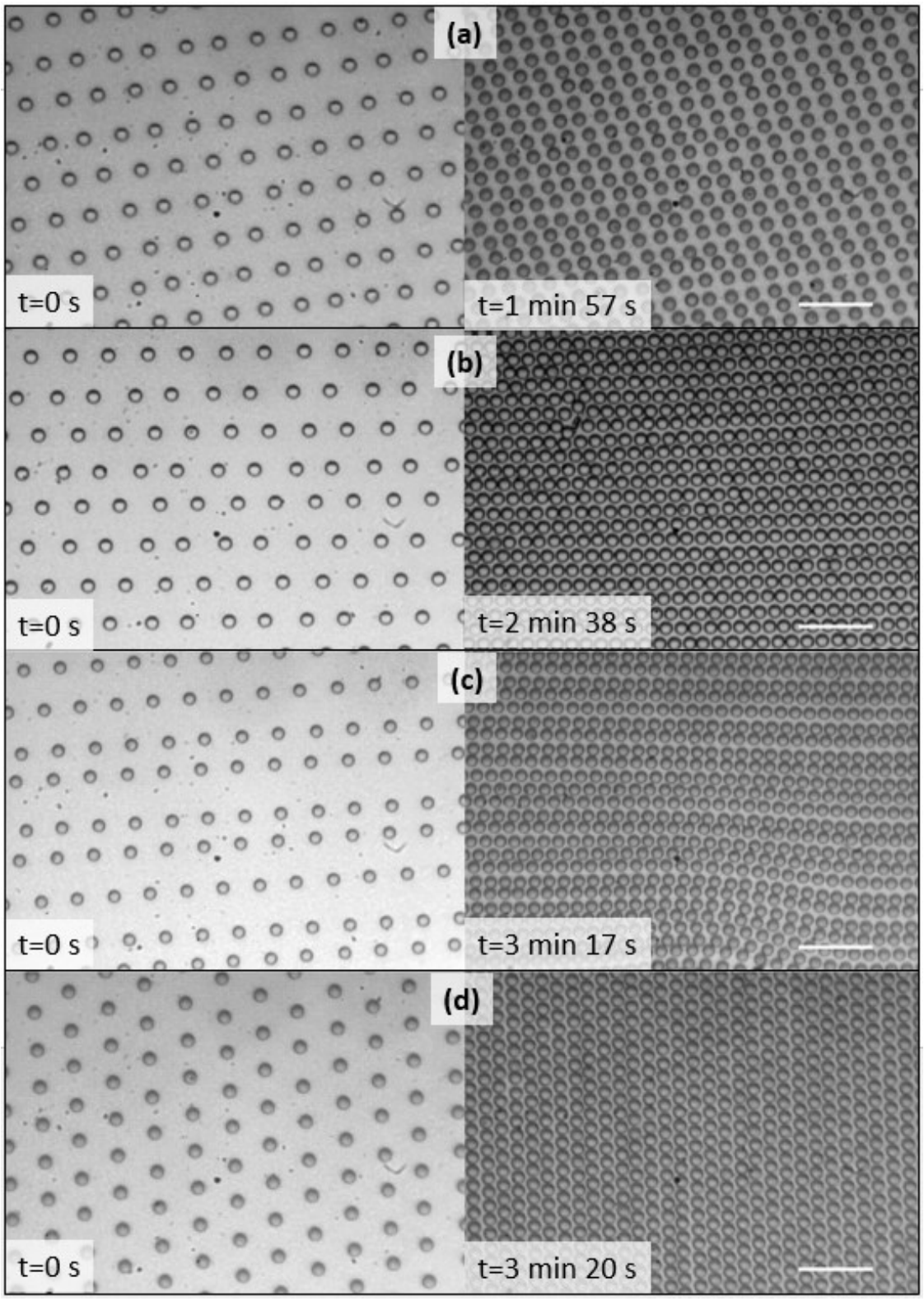

Figure 5.22 Convection at different curing time of PDMS heated at 80 °C. (a) 4 h. (b) 6 h. (c) 8 h. (d) 10 h. Scale bar 100 μm in all the images.

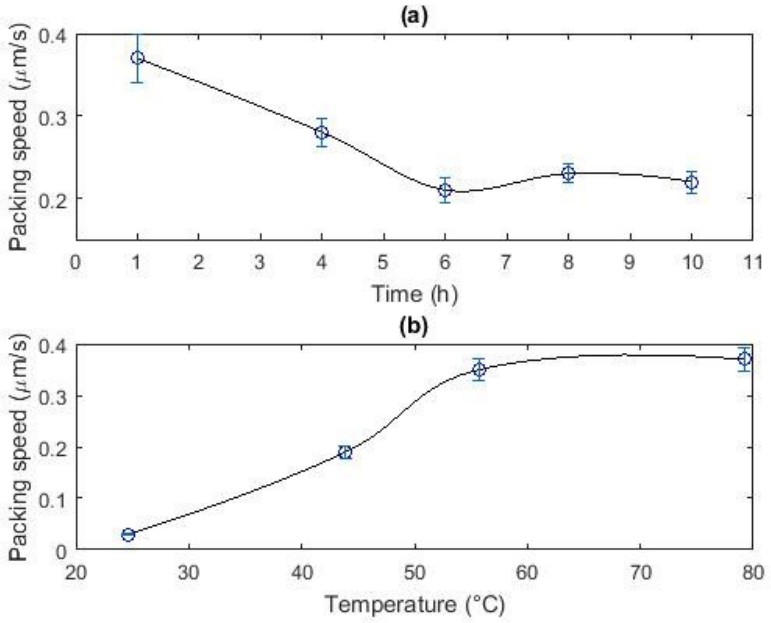

Figure 5.23 The packing speed change under different conditions. (a) Curing time change at room temperature. (b) Temperature change.

The overall packing speed was calculated for the convection conditions mentioned above. Figure 5.23 (a) shows that with the increment of curing time, the speed of packing dropped from 0.37 μm/s to 0.22 μm/s, but after 6 h of curing time, the packing of droplets cannot slow down further, and levelled off at around 0.21 μm/s to 0.23 μm/s. The packing speed for 1 h curing time but at different temperatures is demonstrated in Figure 5.23 (b). This reveals a tendency to increase packing speed with a rise in temperature, but finally after the speed reached the peak, it stopped increasing. The packing speed at 25 °C is 0.03 μm/s, and increases to 0.35 μm/s at approximately 58 °C where the packing speed levels off.

5.3.3 Drop self-organisation by convection conclusion

Convection currents were visualised with the aid of solvent blue 35 dyed PDMS, which revealed that PDMS moved towards the centre and sunk in the middle of the weighing boat. This is the main driving forces for the droplet motion, when drops were printed to he surface of the PDMS and spaced far apart. The behaviour of droplets self-organising and packing on PDMS was also tested. For different patterns of the droplets printed, the cubic droplet matrix formed a pattern with different directions, but hexagonal arrays can close pack with better

arrangement. For 1 h curing time, the higher temperature of heating reduces the time required for packing, but can lead to overlapping of droplets, droplets forming multiple layers as the layer squeezes some drops below the surface and also pulling of streams of droplets down through the centre of the PDMS along the convection pathway. The packing speed at 1 h curing time for 25 °C is around 0.03 μm/s, while for 80 °C is 0.37 μm/s, and at 58 °C the packing speed is 0.35 μm/s already, therefore the packing speed increases with the increase of temperature and then levels off. The packing speed at 1 h curing time is 0.37 μm/s, while at 10 h is 0.22 μm/s, and after 6 h curing time the speed stabilises around 0.22 μm/s.

5.4 Multiple droplets stability on liquid surfaces summary

The stability of arrays of droplets on different fluid surfaces was shown in this chapter, which reveals the most reliable approach to patterning is to keep the droplets separate during the deposition procedure and then allow self-organisation. This provides the sufficiently stable droplet template to explore the capture of droplets in the next chapter. The stability of two droplets printing on to different liquid surfaces shows that there is a certain critical value of relative distance that can keep droplets separate, this value for all the tested surface: vegetable, oil and PDMS was all less than 1 which indicates the droplets still can separate after deposition contact on the surface. However on octyl acetate surface, coalescence happened after two droplets separated, this may due to the low surface tension of octyl acetate. Then the droplets can be separated by printing at a distance between each other, and convection can drive droplets together via self-organisation. The stability of two droplets contributed to quantify the stability of inkjet printing and help to design the patterns for self-organisation.

Convection happens, as predicted, when heating is applied to the system from below, and this convection can drive the droplets printed onto the PDMS surface to move towards the centre of the weighing boat and when they packed close enough, they started to self-organise into hexagonal packing. The convection current was visualised with dyed PDMS on the sample PDMS surface, and the convection imaging system was used to capture the processes. The convection in the PDMS in a weighing boat was driven by heating from a hot plate below. The flow tended to contract from all the directions to the centre of the surface, and descending current was observed as a column of droplets formed in the centre if the solution was not

sufficiently viscous. Then this current separated at the bottom, moved towards the edge of the weighing boat, and ascended at the edge. As a result, the droplets printed on the surface can be driven by the convection current to the centre of the weighing boat and when they were close enough to interact, they can self-organise into hexagonal close packed arrays. The visualisation only used PDMS, which is different from the performance of droplets, therefore the droplets behaviour under convection was also investigated, which revealed an improvement of the self-organisation by printing hexagonal arrays before heating and convection instead of cubic arrays, which can minimise the formation of the packing in different directions and more repeatable pattern was obtained. The packing speed was the main parameter considered for packing, the results show a higher packing speed with higher temperature and a reduced packing speed with longer curing time under room temperature. In this chapter, the convection by heating shown the capability to replace BF method to pack droplets and trigger self-organisation, the self-organisation of the droplets were also visualised. This study of PDMS property change with different curing time is going to be introduced more in the next chapter, and shows the advantage of longer curing times.

Chapter 6 Polymer patterning with inkjet generated templates and self-organisation

6.1 Polymer patterning with inkjet generated templates and self-organisation introduction

In previous chapters, research focused on using single drop printing systems to study the phenomena during printing of liquid drops directly to liquid surfaces. The approach to scaling this up to create monodisperse droplet arrays using the DMP was also discussed in detail. It was clear that there is a minimum droplet spacing to avoid coalescence and ensure monodisperse arrays are achieved. However, it was more reliable to print with a very large spacing and use self-organisation to bring the droplets together. The opportunity noted from the literature review is that this may help with a move towards cross-linking of polymer to template the drops, rather than entangling the polymer upon solvent evaporation. This leads to a more sustainable process, significantly reduced waste and a broader choice of non-toxic materials. In this chapter, the work is reported to explore the templating of the droplet arrays using a cross-linking polymer system. It was already reported that single drops stabilise on PDMS easily, but with a longer time to be fully submerged, as discussed in Chapter 4. Then the stability of multiple droplets on PDMS also investigated, showing that there is certain threshold value to keep droplets separate after printing contact. To avoid coalescence, droplets can be printed at a distance, and in order to obtain a close packed droplet raft for patterning, convection-driven self-organisation happened when heating was applied, which is demonstrated in Chapter 5. PDMS is a viscous fluid polymer under room temperature before mixing with cross-linker. Once mixed with the curing agent PDMS can then cross-link and finally solidify at room temperature over 24 hours or more rapidly at an elevated temperature.

In this chapter, PDMS mixed with cross-linker is used to reveal the newly developed engineering solution of making porous polymers using droplet templating in replace of etching, soft lithography, and direct templating with pre-made moulds. Using the inkjet technique as a precise droplet deposition method, combining with the self-organisation induced by

convection, this is a new one-step cost saving technique with easy loading, which is shown later in this chapter to allow printed functional materials to be integrated directly into the pores. The detailed rheology of the process is also explored to understand the role this plays in the self-organisation and pore geometry. Also, as noted in the literature review, the work on the BF technique relies almost entirely on quantitative descriptions of the level of ordering observed and here a script was developed to analyse the quality of the patterning of the droplets with a distribution of the angles between the centre-to-centre connections between adjacent pores. Overall, the approach was designed to both study the fundamental phenomena of drop capturing while also considering the challenges faced during manufacturing.

6.2 Drop self-organisation and polymer patterning

Drop self-organisation is mainly depending on the convection current within the substrate fluid, which is introduced in Chapter 5. The study was carried out by investigating the convection in PDMS samples. This self-organisation phenomenon is utilised for polymer patterning, with droplets printed far apart and driven to pack together, then PDMS cross-linking is used to capture the structure of the droplets.

6.2.1 Drop self-organisation and polymer pattering introduction

PDMS is a non-degradable synthetic polymer widely used in biomedical applications in prosthetics and as the drug carrier. It cannot be patterned with BF method, due to its low solubility in organic solvents, and the inherent fluid properties. Therefore in this research, it is considered to pattern the PDMS directly by droplet deposition instead of using growth by condensation.

As noted in Chapter 5, convection is driven when heating the PDMS sample from the bottom of the container, however the heating also speeds up the curing of PDMS dramatically. The goal is to use convection to drive the droplets to pack into hexagonal close packed arrays and PDMS to capture the structure of the final pattern formed by the droplets. PDMS has the unit of $–OSi(CH_3)_2–$ sequences, which determines the hydrophobic surface properties. The calculated contact angle of 50 % mass fraction of glycerol water solutions under the surface of PDMS is 173.1° ± 1.1°, which is shown in Chapter 4. This hydrophobicity should lead to a

very small pore opening at the PDMS/air interface due to the GW droplets being almost fully submerged. This leads to a large chamber, suitable for holding the functional material. With this porosity, the chamber can store the droplet contents and the small opening can be used to control the releasing speed, therefore this structure has a huge potential in drug delivery vehicle applications with significant more control than the current BF method. The following theory and work is targeting achieving this output.

6.2.2 Drop self-organisation and polymer patterning theory and method

As introduced in Chapter 3, PDMS is a fluid before cured. After mixed with cross-linker, PDMS this changes to a solid/rubbery state. For the preparation of PDMS, as described in Chapter 3, Sylgard® 184 silicone elastomer kit has two liquid components - the elastomer base and the curing agent. In this research the curing agent was added to the PDMS at a 10 to 1 weight ratio, using a mass balance, and then mixed in a disposable centrifuge tube for 10 minutes to ensure thorough mixing. It was found that thorough mixing and repeatable mass measurements were important for repeatable experiments. A syringe was then used to take approximately 5 ml of the mixture and this was placed into weighing boats as introduced in Chapter 5.

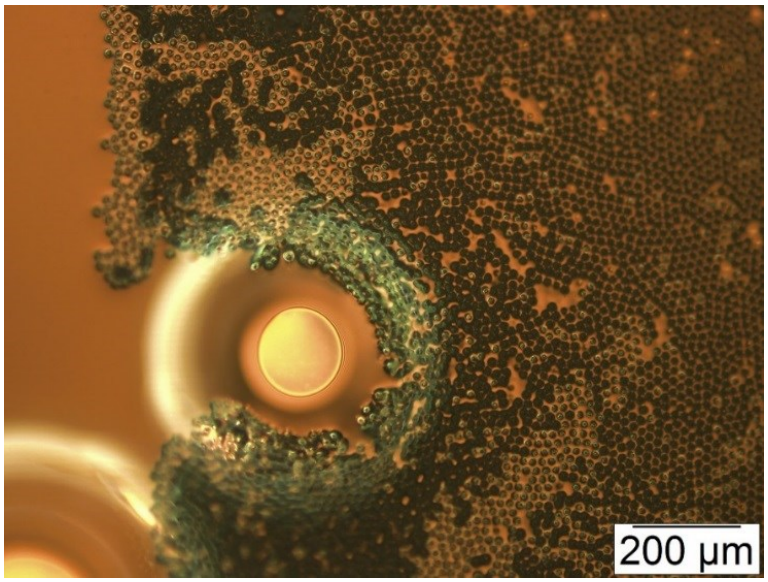

Figure 6.1 Defects in cured PDMS due to bubbles left within the mixture after incomplete de-gassing.

Air bubbles are introduced during mixing, and do not dissipate due to the high viscosity, thus de-gassing is required after the mixture is transferred into weighing boat. De-gassing was carried out by placing the weighing boat under vacuum until no more bubbles become visible. This procedure is vital in PDMS patterning, as the bubbles trapped can lead to defects in the pattern, as shown in Figure 6.1 where GW droplets surround the deformation made in the PDMS by an air bubble. Normally, 30 min is required under vacuum to ensure the mixture is bubble-free and can be used for patterning.

Figure 6.2 demonstrates the four main steps for PDMS patterning. The DMP was used for patterning, with a pre-designed pattern (described later in this section) and waveform (tuned for each GW ink to ensure single drops were achieved without satellite droplets). With the DMP, it is possible to design different arrangement of droplets. At the beginning of the research, the pattern designed is a 10 mm × 10 mm cubic array of droplets as shown in Figure 6.2 (a). In this schematic drawing, the number of the actual drops is kept small for ease of illustration but in reality 200 drops are printed along the x-direction. The size of the droplets generated by DMP is around 20 μm in diameter, and the space between droplets can be set, as shown in Figure 6.2 (a). The space can be controlled between drop 1 and drop 2 or between drop 1 and drop 3. From the results shown in previous chapters, droplets contacting during printing may lead to coalesce, therefore 50 μm was set as the centre-to-centre spacing to ensure that the droplets would not interact when being printed. During Chapter 5, it was found that cubic-array droplets struggled when they tried to self-organise into hexagonal arrays, and formed irregular pattern with small gaps or different zones of packing. Therefore the pattern was changed to hexagonal arrangement, the drop 4 and drop 5 in Figure 6.2 (a) is still 50 μm, but the space between each row of droplets was changed, as it is now the centre-to-centre spacing between 4 and 6, 5 and 6 is 50 μm. For the purposes of this research, this was assumed not to be a significant source of error. The templating droplets were generated at 5 kHz and deposited onto the sample which is shown in Figure 6.2 (b). After that, in Figure 6.2 (c), the samples were then placed into an oven set at 80 °C for 2 h to self-organise the droplet template as well as to cure the PDMS. Figure 6.2 (d) shows the planned final structure of porous PDMS after the drop content evaporates.

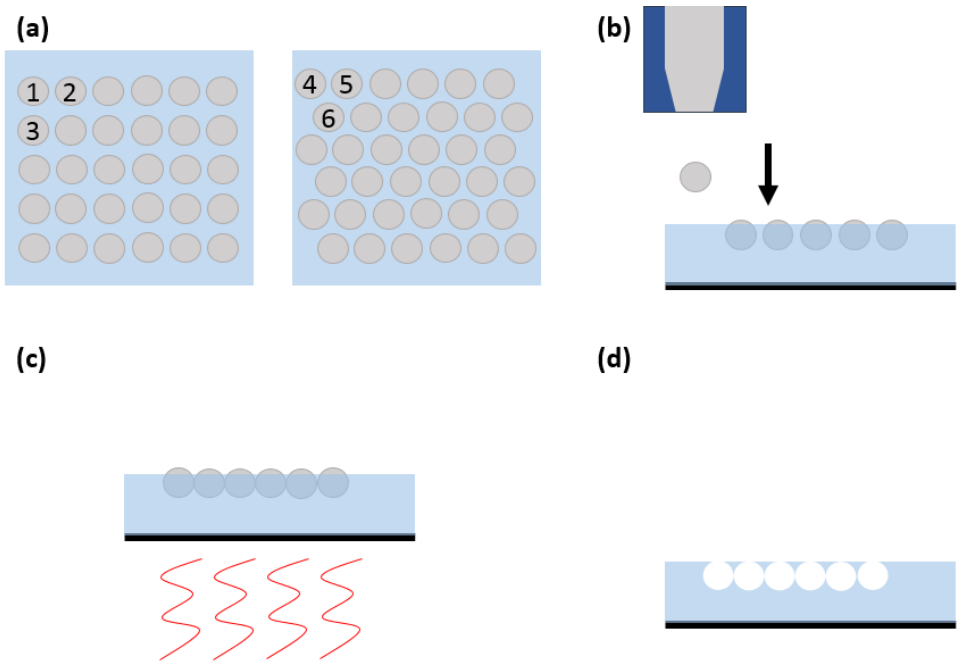

Figure 6.2 Four main steps of PDMS patterning. (a) Pattern design. (b) Printing onto PDMS (c) Self-organisation of droplets. (d) Captured pattern in PDMS.

GW solutions were used as the templating droplets, and later as the solution to carry functional materials that can make them printable. PDMS has low solubility in organic solvents but some of the organic solvents can make PDMS swell. A study of solubility of PDMS in a numbers of solvents showed the calibration of the relationship between the solubility parameter (δ) and the swelling ratio (S); the solubility parameter, which is known as the Hildebrand parameter is the square root of the cohesive energy density (molar cohesive energy over molar volume) [112], and the swelling ratio is the length of PDMS in the solvent over the length of the same dry PDMS [113]. The relationship between the swelling ratio (shown as Log(S)) and the solubility parameters is shown in Figure 6.3. Glycerol and water were examined and shown in this graph as point 37 and 38. They grouped the solubility of the solvents as low solubility ($1.00 < S < 1.10$), moderate solubility ($1.10 < S < 1.22$), and high solubility ($1.28 < S < 1.58$), and extreme solubility ($1.58 < S < 2.13$) [113]. Importantly, glycerol, 1-propanol and other alcohol like ethanol, methanol etc., are in the low solubility region. Therefore GW solutions cannot make PDMS swell significantly, and the porosity of PDMS patterned with GW droplets can be preserved. In future studies, the high solubility and the extreme solubility groups should be avoided in PDMS patterning.

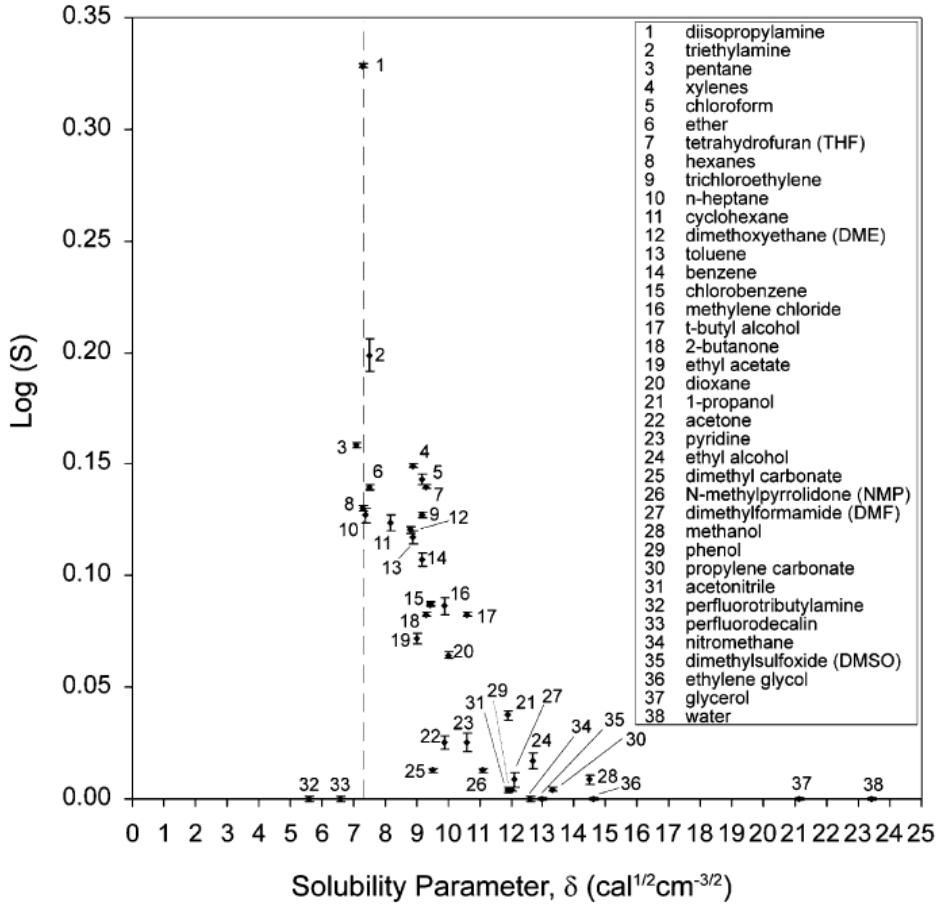

Figure 6.3 Relationship between swelling ratio for different solvents and the solubility parameter. The dashed line is the solubility parameter of PDMS (7.3 $cal^{1/2}$ $cm^{-3/2}$), solvents with similar values of δ results in a greater swelling of PDMS. [113]

6.2.3 Drop self-organisation and polymer patterning results and discussion

Initial experiments followed the procedure noted earlier. From the optical microscopy image of a typical sample shown in Figure 6.4 (a), it is seen that the drops on the PDMS surface are at different level, with some droplets completely submerged in PDMS, with clear overlapping visible. Figure 6.4 (c) is an example SEM image of the same sample, and it is clear that the droplets packed hexagonally in many regions, although they have been printed as cubic arrays. Also it shows that there are significant differences in pore opening sizes. Figure 6.4 (b) reveals the PDMS structure after cured under room temperature, droplets form several layers as well and drops have submerged into the mixture, which the failed to form an opening on the surface. Figure 6.4 (d) reveals the inner surface of a pore, and that the pore formed rough surfaces,

because the inner structure is not the main focus of this research, only the hypothesis was made that the way of drying of the GW solution inside the pore left the rippled structure.

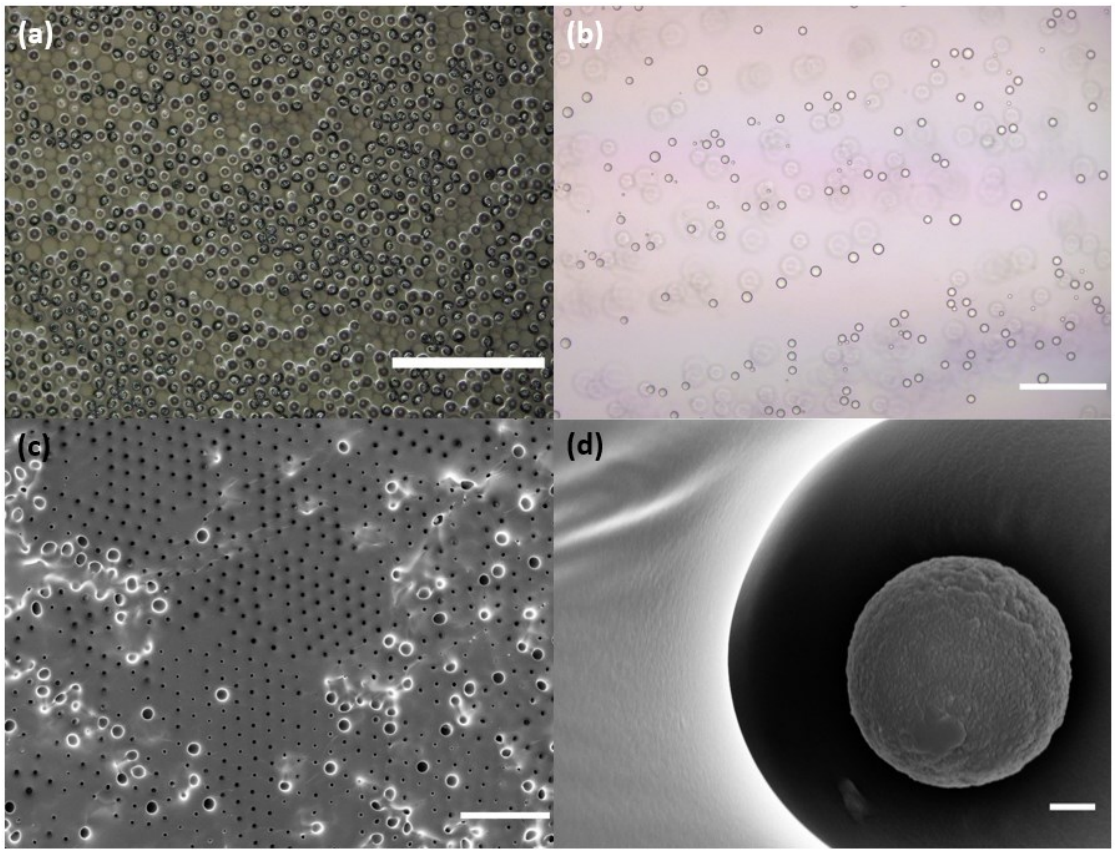

Figure 6.4 Microscope and SEM images for PDMS (1 h curing time) patterned by 50 % GW droplets cubic arrays generated by DMP. (a) PDMS cured in oven at 80 °C for 2 h. Scale bar 200 µm. (b) PDMS cured under room temperature for 48 h. Scale bar 200 µm. (c) SEM images of (a). Scale bar 100 µm. (d) SEM images of details inside pore in (a). Scale bar 0.5 µm.

The size distribution of the pore opening on the surface of PDMS is illustrated in Figure 6.5, this is measured specifically for image Figure 6.4 (c) using ImageJ software particle analysis plug-in which is introduced in Chapter 3. This plug-in was most often used for the droplet diameters, in this case it is utilised to measure the diameter of the openings on the surface. In Figure 6.5, it shows that there are two peaks of distribution one is between 0-2 µm, the other is between 4-6 µm. Manually identifying the smallest visible pores in Figure 6.2, the smallest size recorded is 1.96 ± 0.02 µm, therefore within this distribution of opening sizes, any results smaller than 2 µm can be ignored as these are the randomly picked pixels in the image. The

larger openings were randomly picked as well to do the manual measurement of the diameter. The smallest found is 8.14 ± 0.02 µm. Therefore the drops embedded within the PDMS formed the pore opening size of about 2-8 µm which explained the peak in between 4 µm and 6 µm, but some of them were measured between 8-10 µm.

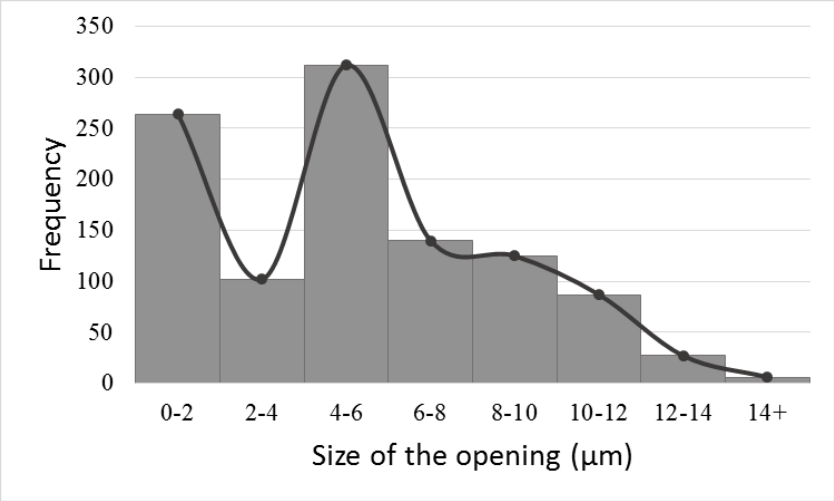

Figure 6.5 Size distribution of the pore opening size for the PDMS sample patterned by 50 % GW cured at 80 °C for 2h.

These results showed an irregular packing of pores on PDMS, with regard to the pore opening size as well as the pore ordering. As noted in Chapter 5, at higher temperatures, the convection flows can be observed to drag droplets below the surface and lead to poor ordering. In order to achieve more regular packing, room temperature curing and self-organisation was tested. Figure 6.6 demonstrates two typical structures that can form under room temperature. Figure 6.6 (a)-(b) shows the unpacked status of droplets, and Figure 6.6 (a) is the edge of the weighing boat where no drops were printed. Figure 6.6 (c)-(d) reveals that within the bulk of the arrays that the organisation was not complete, some droplets self-organised into hexagonal arrays but some aggregated in clusters within a packed matrix.

This self-organisation at room temperature is believed driven by the random movement of the substrate and droplets particles as well as the lateral capillary forces. As introduced in previous chapters, the droplets hang at the substrate/air interface due to surface tension, this surface tension effect can create deformations at the interface, then leading to weak capillary attractions between nearby objects. The lateral capillary force driven 2D convection were mostly studied

for sub-micron level colloidal particles [114][79], but similar to nanoscale particles, at micon-scale, solid granules can stick harder together by the action of capillary forces [115], as the droplets act as hard beads, the capillary forces can also drive the self-organisation.

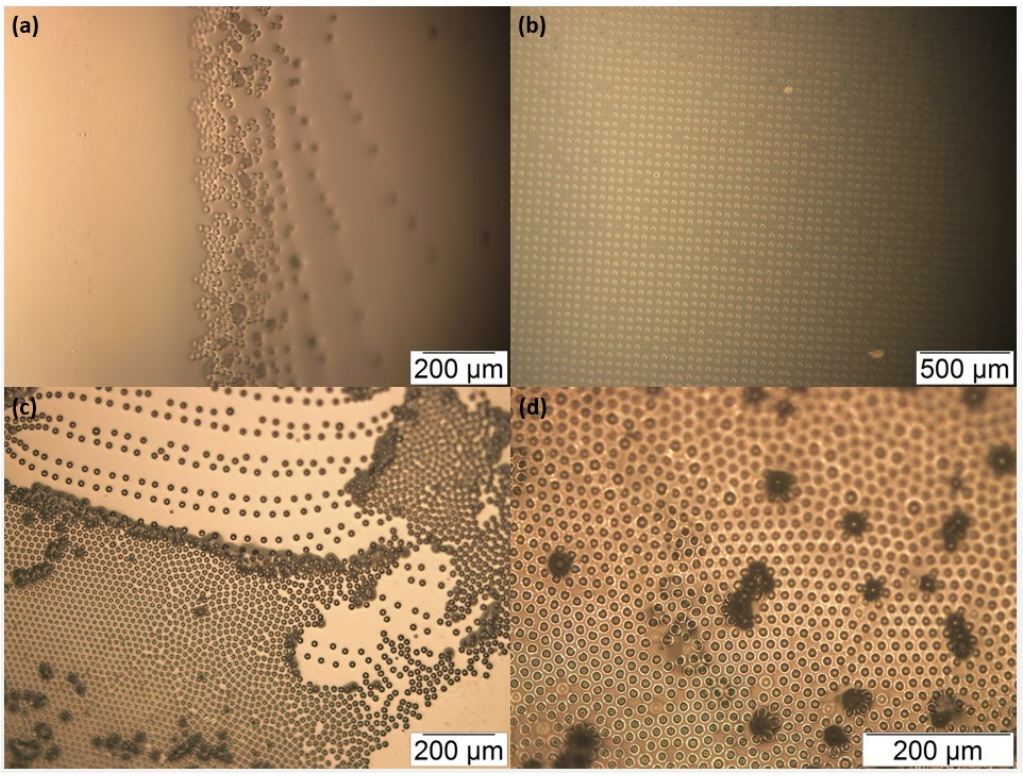

Figure 6.6 Microscope images for room temperature cured PDMS (1 h curing time) printed with cubic arrays. (a)- (b) Droplets on PDMS did not pack. (c)- (d) Some droplets packed some moved further apart.

According to Figure 6.6, room temperature is not an operating temperature to produce ideal patterning of PDMS with this method. Also 80 °C is the optimal PDMS curing temperature but led to rapid convection flows and poor drop self-organisation, thus the temperature was lowered to 60 °C. Figure 6.7 demonstrated the PDMS patterning with a curing temperature of 60 °C in an oven for 2 h. Figure 6.7 (a) shows a representative sample and that most of the droplets did not transition and pack in a hexagonal array. Figure 6.7 (b) is the detailed view of the same sample, with cubic pattern of droplets printed, it is difficult to find the minimum energy packing (hexagonal packing). Figure 6.7 (c) shows the unpacked area with defects formed by drop missing. Figure 6.7 (d) shows the droplets at different level which is the same

as PDMS cured at 80 °C. The temperature is still too high for the self-organisation of droplets into a single layer hexagonal packing, however the level of multi-layer artefacts has decreased (qualitatively). This initial improvement led to a shift to a curing temperature of 40 °C, Figure 6.8 reveals a representative sample from the results of the patterning. Figure 6.8 (a) shows that the droplets packed better than 60 °C in hexagonal arrays, but as Figure 6.8 (b) shows that the droplets in this case were also completely submerged beneath the surface of PDMS.

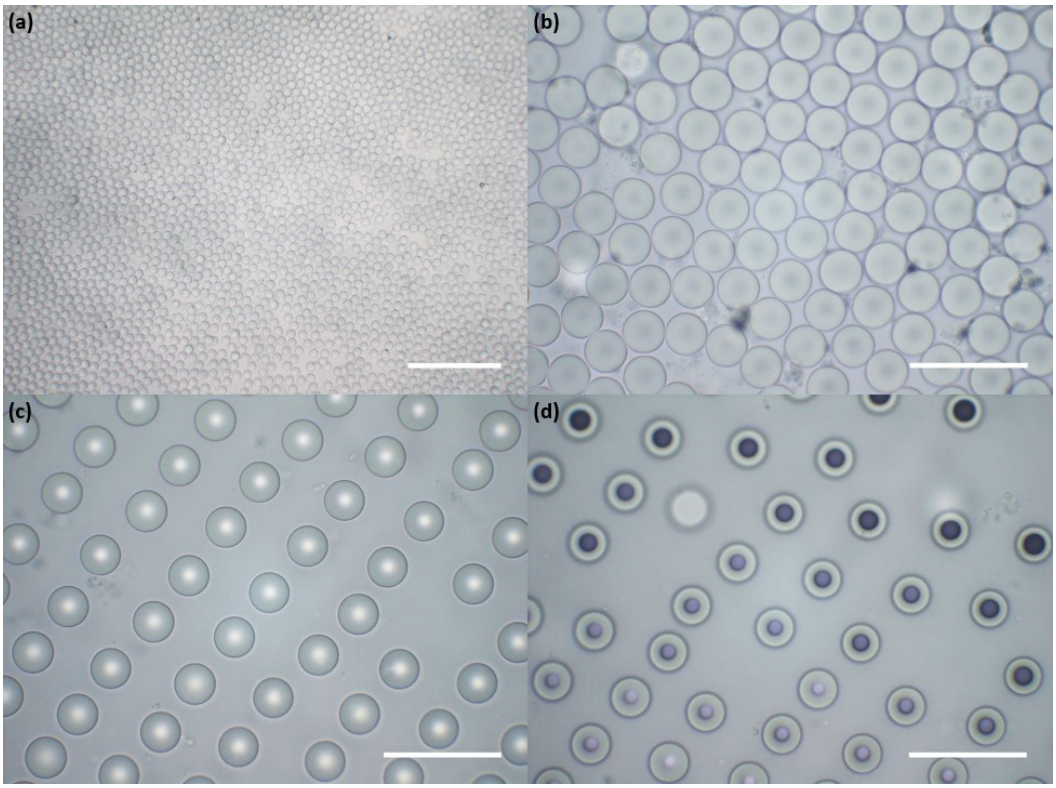

Figure 6.7 Microscope image of PDMS (1 h curing time) cured at 60 °C in oven printed with cubic arrays. (a) Overview of the sample. Scale bar 200 µm (b) Packed part. (c) Unpacked part. (d) Droplets of different contact angle. (b)-(d) Scale bar 50 µm.

The distance between the droplets were also studied. With a high temperature, droplets can be printed further apart therefore the time required for the droplets to pack together is longer and PDMS is cured during this time. This was expected to allow the droplets to be more ordered with a higher PDMS viscosity at the time that they meet. In Figure 6.9 (a) and (b), smaller spacing of around 20 – 30 µm between droplets leads to coalescence, and 40 – 50 µm in Figure 6.9 (c) and (d) there is no coalescence, Drop spacing of 50 µm has the best packing

performance, and drop spacing of 50 µm has the best packing performance. Nevertheless larger spacing results in the failure of packing. Droplets spacing of 120 µm and 150 µm are revealed in Figure 6.9 (e) and (f), the droplets stopped packing together, they tend to aggregate in lines.

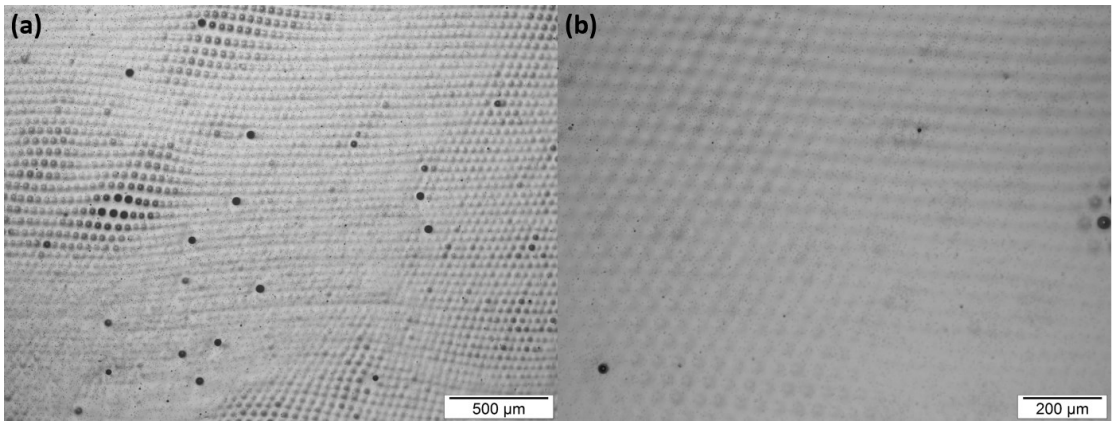

Figure 6.8 Microscope image of PDMS (1 h curing time) cured at 40 °C in oven printed with cubic arrays. (a) Irregular packing. (b) Under the surface.

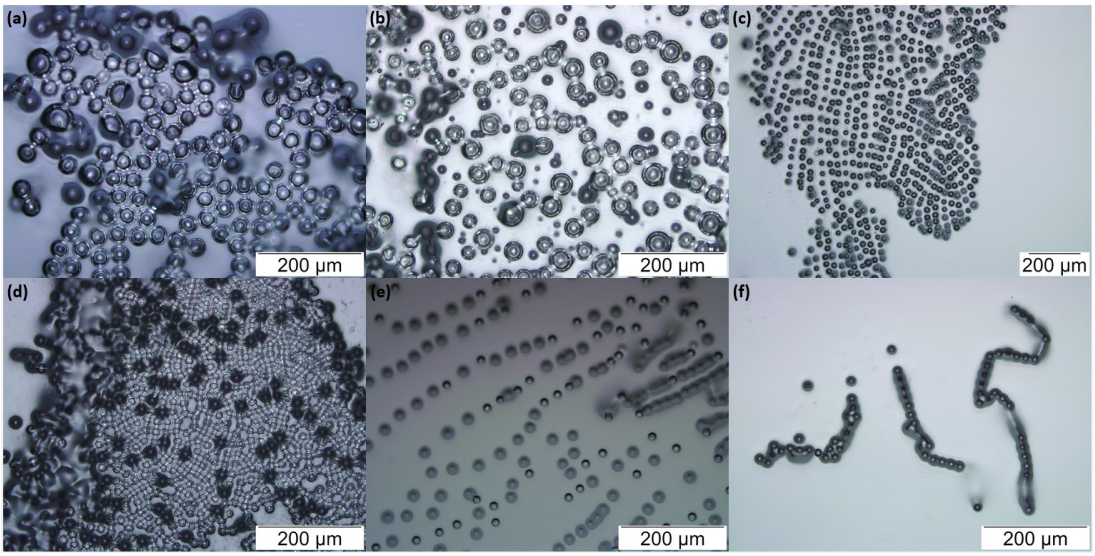

Figure 6.9 Microscope images for different droplet spacing. (a) 20 µm (b) 30 µm (c) 40 µm (d) 50 µm (e) 120 µm (f) 150 µm.

6.2.4 PDMS rheology study

The key parameters of curing time, curing temperature and droplet spacing are found to be important to control. A more quantitative approach was used, where the details of the PDMS

rheology was mapped out to help with parameter choice. As PDMS cures over time, once mixed with the cross-linker, the viscosity of the fluid will increase gradually, which would affect the convection and the regularity of the packing. The viscosity of PDMS for different curing time was measured by using the rheometer in CAPE building in Cambridge with the help of Dr. Clare Conboy. The whole process was designed to map onto the process of PDMS patterning. The timing of the experiment commenced upon mixing with the cross-linker. The required de-gassing step was included and then sufficient time was measured to indicate a pause prior to printing. This pause is important in terms of the viscosity of the fluid prior to printing and so a range of times were attempted. While no printing was carried out, there was then a ramp up of the temperature to indicate when the self-organisation process commenced.

As shown in Figure 6.10, PDMS was mixed with the cross-linker and different samples were left at room temperature to cure for a given time. Rheological tests were carried out for the next 300 s at room temperature, because this mimics the time when GW droplets are printed onto PDMS with the DMP. After 300 s, the temperature was ramped up to the target temperature (e.g. 80 °C in 40 s), in real patterning experiments at this stage, PDMS samples were put into the oven for droplet self-organisation and heat cured, and afterwards the temperature was maintained at 80 °C where the PDMS samples were in the oven to fully cure.

As illustrated in Figure 6.10, PDMS was measured at 1 h, 2 h, 4 h, 6 h, and 10 h after room temperature curing, the initial 300 s is also under 25 °C. The viscosity of PDMS increased from 3.25 Pa·s at 1 h curing time to 15.20 Pa·s at 10 h curing time. There is a sudden rise between 8 h and 10 h, as the viscosity is 8.67 Pa·s at 8 h. Then the temperature is ramped up to 80 °C, and it is noticeable in Figure 6.9 that after heated up at 300 s, the viscosity of PDMS first dropped, at this stage, as expected in a fluid. This is the point when convection is observed and so the drop in viscosity is important to consider as it will control the velocity at which drops approach. Then more PDMS cures during the heating, therefore the viscosity starts to climb rapidly and finally the extremely high viscosity and the fluctuation in rheology results indicates that there are solids forming within the test PDMS sample.

This level of viscosity and self-organisation control suggests that similar to earlier BF work [116] there should be some level of control over the geometry of the cavity and the quality of

packing by printing at different times after curing. For example, an initial test showed (Figure 6.11), after 2 h of curing the size of the final packed pattern is about 3.1 mm, and if 10 h was used as a pre-printing delay the size is approximately 8.3 mm. With every additional hour after the mixing of the curing agent, the 10 × 10 mm hexagonal array of droplets printed shrinks to a lesser extent, and so it is clear that the convection currents are indeed reduced.

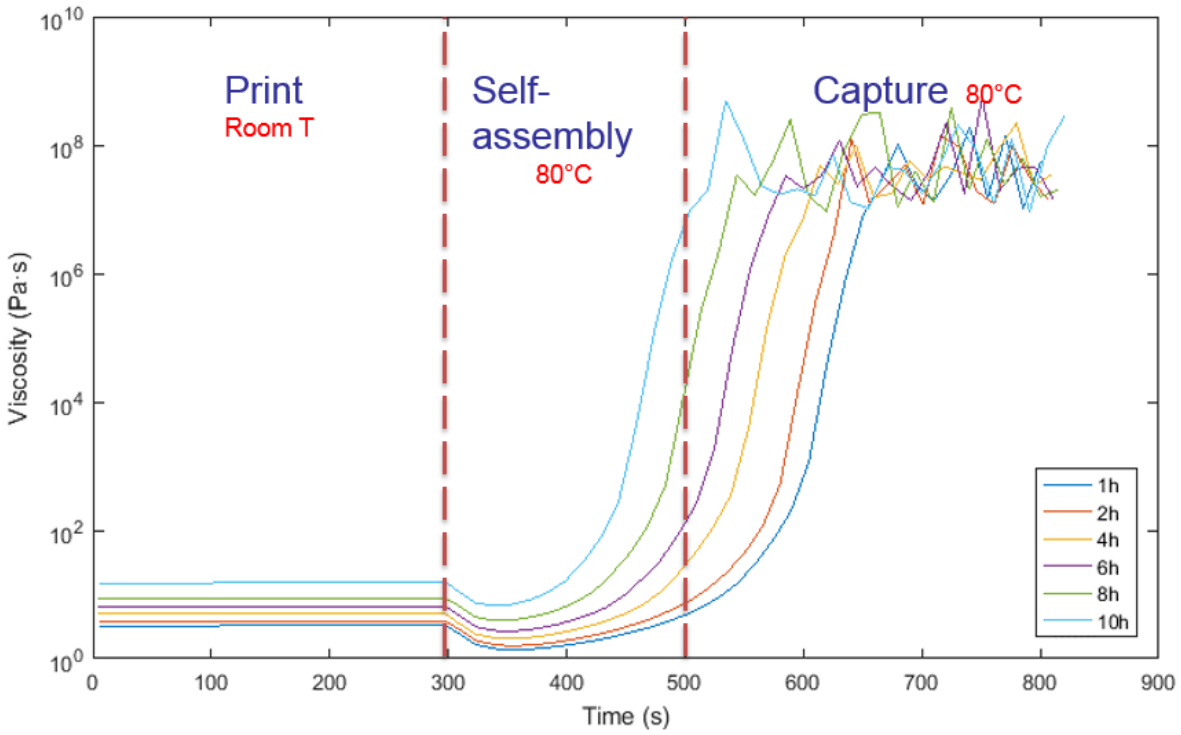

Figure 6.10 PDMS rheology measurements from 1h to 10 h. 0-300 s room temperature, 300-500 s temperature increased to 80 °C, after 500 s temperature kept at 80 °C.

The change in the patterned area resulting from droplets packing and self-arrangement can also be examined by the normalised area, which is shown in Table 6.1. The pattern is programmed with the DMP, the target width and height of the pattern were both 10 mm and the actual width was 10.025 mm and the height was 10.043 mm with 200 droplets in both directions. Then the minimum packed width was 3.50 mm and the packed height was 3.03 mm, therefore the minimum area was 10.61 mm^2. The normalised area is defined as the measured area of the sample divided by the minimum area of the packed structure. Therefore, for normalised area greater than 1, the pattern is not close packed, while those less than 1, the droplets were overlapped after packing. According to Figure 6.11 the normalised area showed a linear

increase with the increase in curing time. In Table 6.1, the normalised area is less than 1 for 1 h curing time, which as mentioned, represents the overlap of droplets, and at 2 h curing time, the normalised area is 1.27, which is about close packed. Then after 2 h curing time, the size of the final packed pattern kept growing and at 24 h curing time, the normalised area is 10.37, which means the pattern were captured as the way it was printed. This gives an insight into the level of control that can be achieved with this system and quantitative measures of the outputs.

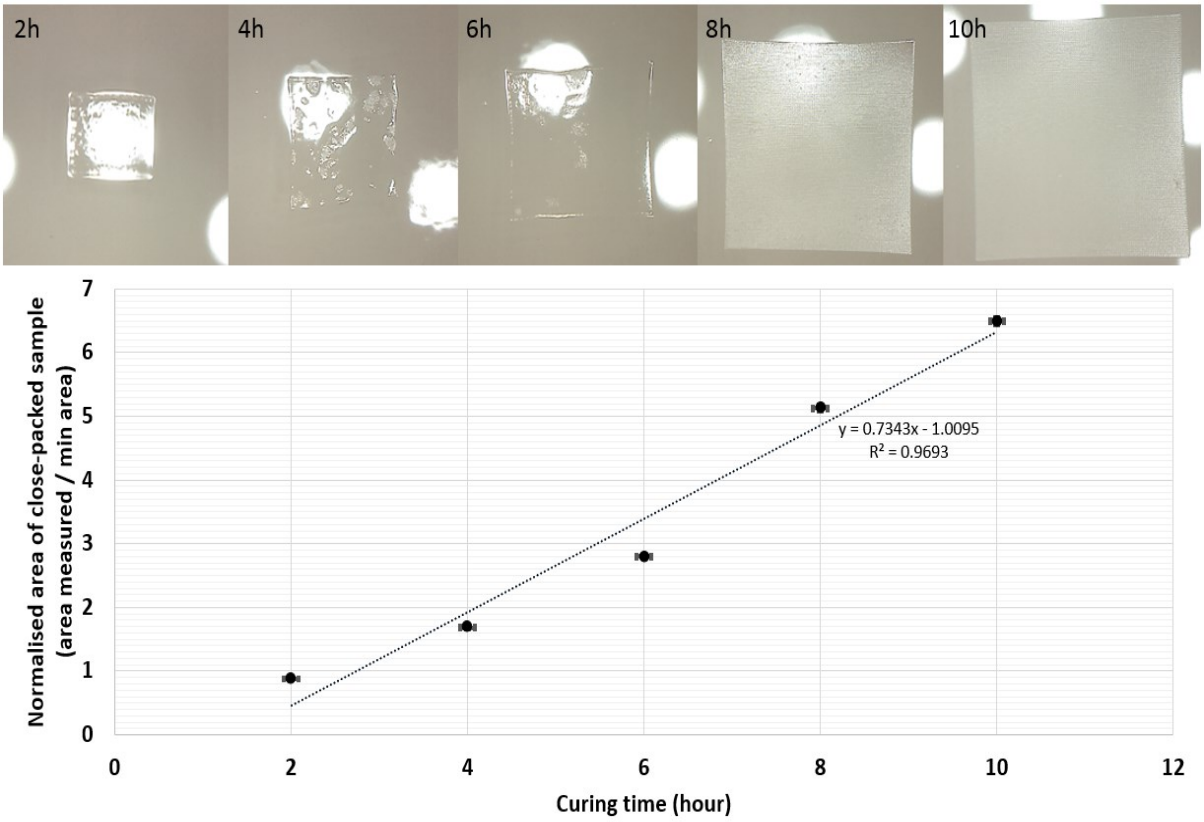

Figure 6.11 Size change of the packed pattern for different curing hours. The error bar in x is constant 0.08, and in y is 1 %.

Table 6.1 The area and normalised area of patterns on PDMS sample

Sample (hr)	Area (mm^2)	Normalised area
1	6.52	0.61
2	13.51	1.27
4	34.05	3.21
6	41.63	3.92
8	67.55	6.37
10	85.17	8.03
24	110.06	10.37

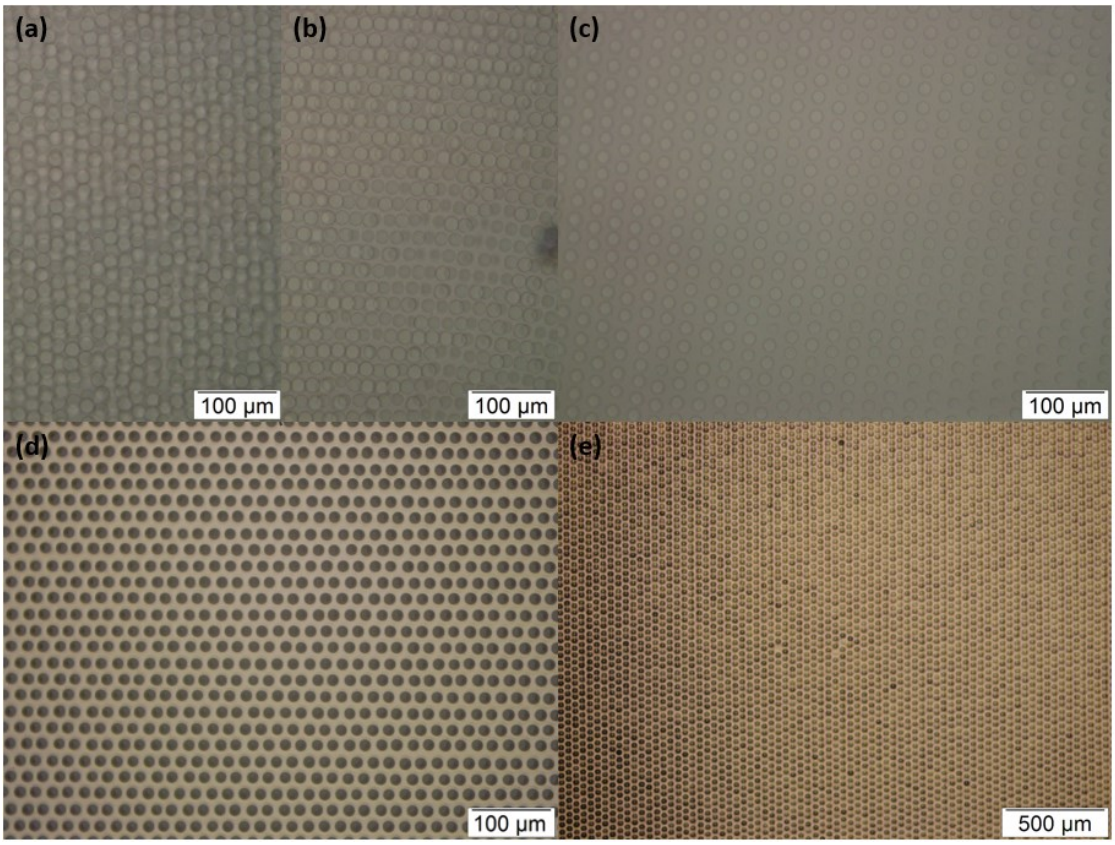

Figure 6.12 Microscope images for hexagonal arrays of packing from 2 h to 10 h curing time. (a) 2 h. (b) 4 h. (c) 6 h. (d) 8 h. (e) 10 h.

From this work, it was clear that there is an optimum time to allow the PDMS to cure, prior to printing. Figure 6.12 reveals the results of packing with a regulated PDMS curing time, thus controlling the viscosity. Figure 6.11 (a) and (b) are the 2 h and 4 h packing, it shows that the droplets still formed multiple layers and over-packing. Figure 6.12 (c) is the 6 h packing, which shows a regular packing but slightly under the surface of PDMS. Starting from 8 h curing time, PDMS is partly cured and the convection is limited, and the pattern printed can be fully packed into highly ordered structures.

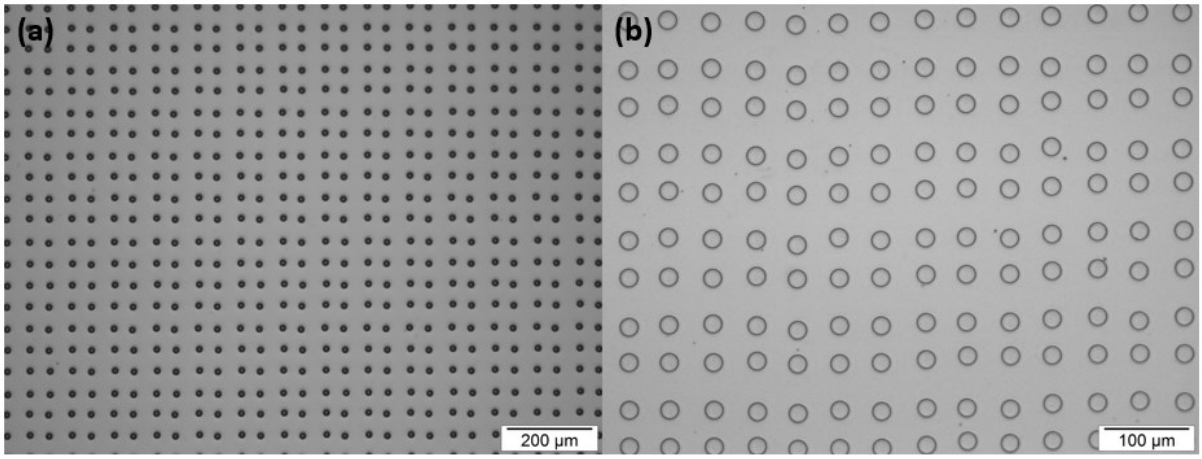

Figure 6.13 Microscope images of cubic packing on PDMS. (a) 10 h. (b) 24 h.

This regulation over the dynamics of the system has the additional benefit of being repeatable and tuneable to allow higher density packing of square arrays. It was hypothesised that a careful tuning would also enable freely designed configurations. Figure 6.13 demonstrated the cubic packing pattern for 10 h and 24 h curing time. It shows that after PDMS cures under room temperature for 24 h, it still can be patterned with droplets. The average size of the imaged pore in Figure 6.13 (a) is 17.37 µm, and the average size in Figure 6.13 (b) is 23.39 µm. The size is larger for 24 h than that of 10 h, therefore the geometry of the pores must have changed. The SEM images of the top view of these samples and the cross-section of the pores are revealed in Figure 6.14. From 8 h to 24 h curing time the geometry of the pore changed significantly. Figure 6.14 (d) shows that 8 h curing time resulted in a pore with a small opening on the surface of PDMS followed by a larger spherical chamber underneath. The materials around the pore is the protective layer of titanium, without the protective layer the edge of the pore can be deformed. At 10 h, which is shown in Figure 6.14 (e), the pore is changed to a cylindrical pit,

and at 24 h in Figure 6.14 (f), shallow marks can imprint onto PDMS and the pattern can be fully captured, however the materials in the ink can only be left on the surface.

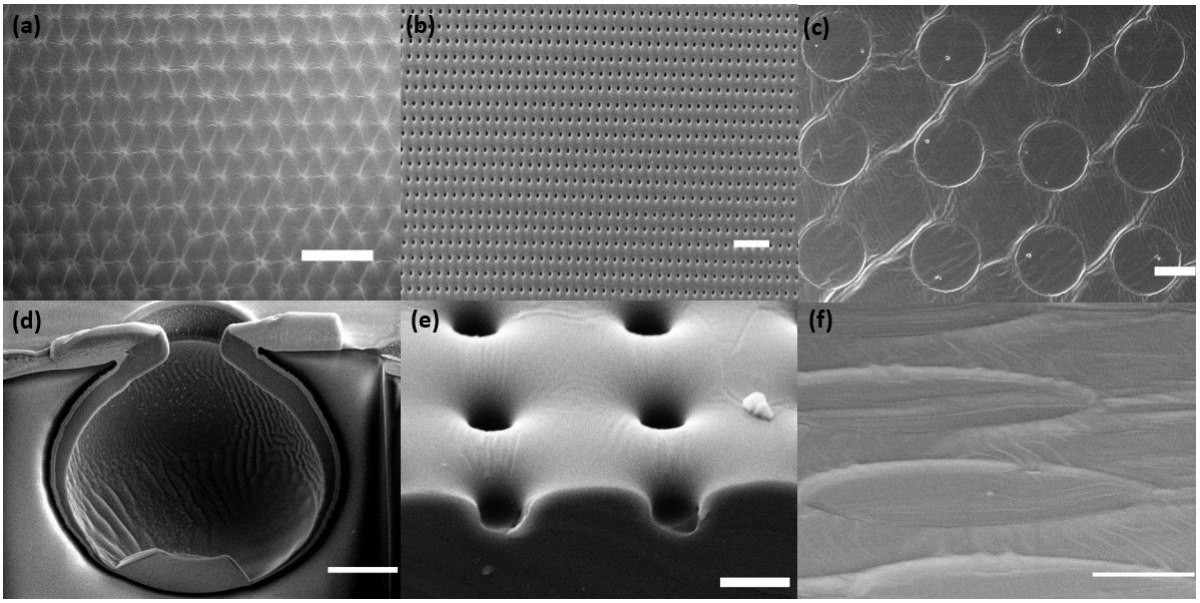

Figure 6.14 Images of 8 h curing time, 10 h curing time and 24 h curing time. (a) SEM 8h hexagonal. Scale bar 100 μm. (b) SEM 10 h cubic. Scale bar 100 μm. (c) SEM 24 h cubic. Scale bar 20 μm. (d) Helios Cross-section of (a). Scale bar 5 μm. (e) SEM Cross-section of (b). Scale bar 20 μm. (f) Tilted imaging of (c). Scale bar 10 μm.

At 8 h curing time, the diameter of the opening on the PDMS surface is approximately 8.28 μm. The pore opening size distribution is exhibited in Figure 6.15. In contrast with Figure 6.5, the pore size gathered around 8-9 μm at 8 h curing time, while the pore size is mostly around 4-6 μm. This is a very tightly controlled size and with this change of the opening size, the release speed of the inner contents of the pores is more likely to be controllable.

At 24 h curing time the whole pattern can be fully preserved. As demonstrated in Figure 6.16, bitmap images were uploaded into the DMP, which is introduced in Chapter 3, the patterns were printed onto PDMS pre-cured for 24 h under room temperature. Comparing Figure 6.16 (a) and (b), the same IfM pattern was printed, at 8 h when the PDMS was still able to flow and the pattern packed into a dense pattern (shrinking of the image by close packing), while at 24 h the original pattern was stamped onto PDMS and also in Figure 6.15 (c). The challenge of this

technique is at 24 h the droplets are exposed on the surface of PDMS, therefore it is apparent that some coalescence happened in both Figure 6.16 (b) and (c), the spacing between the droplet requires carful design when processing bitmap images as a template.

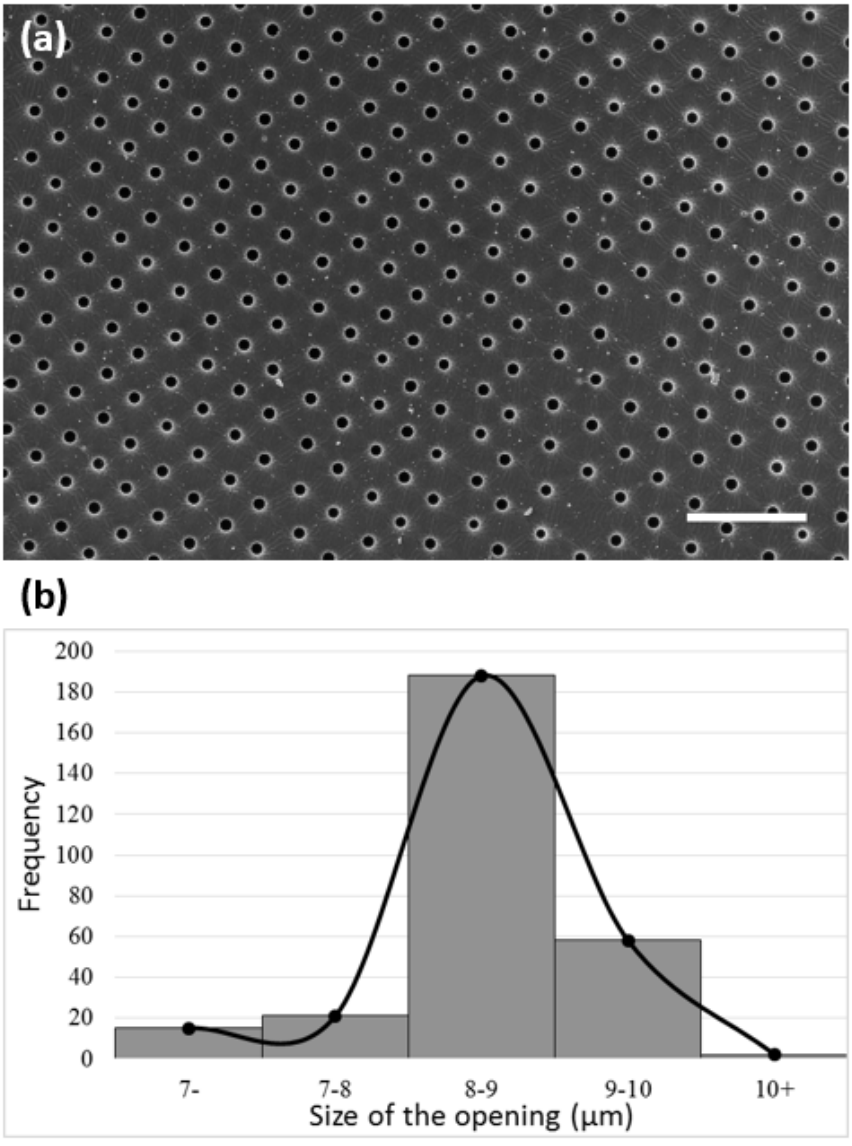

Figure 6.15 Size distribution of the pore opening size for the PDMS 8 h sample patterned by 50 % GW cured at 80 °C for 2h. (a) The SEM image used for analysis. Scale bar 100 μm. (b) Size distribution of the diameter of the pores in (a).

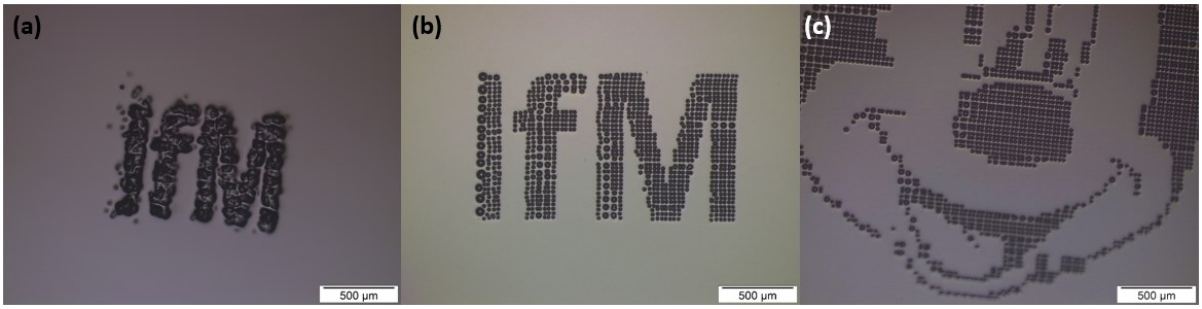

Figure 6.16 Microscope images of bitmap designed patterns on PDMS. (a) 8 h IfM. (b) 24 h IfM. (c) Micky mouse.

6.2.5 Printing functional materials

The challenges with the BF method are both in the control of the highly dynamic system and also in the final tuning of the surface functionality. Direct deposition of inks enables the inclusion of functional materials at the same time as the templating. Figure 6.14 (d) shows the structure has a real potential for embedding functional materials easily within a polymer matrix. Control over contact angles due to the surface tensions was discussed previously, which will be explored to control release or swelling rates. Figure 6.17 and Figure 6.18 shows the structure of different materials. A variety of functional materials such as carbon nanotubes, gold nanoparticles and iron oxide particles can be printed and enclosed in the close packed pores. PEG 1000 can also be printed. PDMS embedded with PEG 1000 beads is very promising in the application of controlled drug release.

This flexibility is not feasible with the BF method, as noted in Chapter 2. Evidence of the isolation of materials within pores is given in Figure 6.18 (a)-(b), where an SEM image and subsequent EDX mapping shows a very strong signal from the iron oxide now embedded within the pores, but not present on the upper surface. Figure 6.18 (c) shows the cross section of a pore of PEG 1000. This material is often used to deliver small molecule pharmaceuticals because it is biologically compatible, water soluble and can store and release these molecules in a reliable fashion.

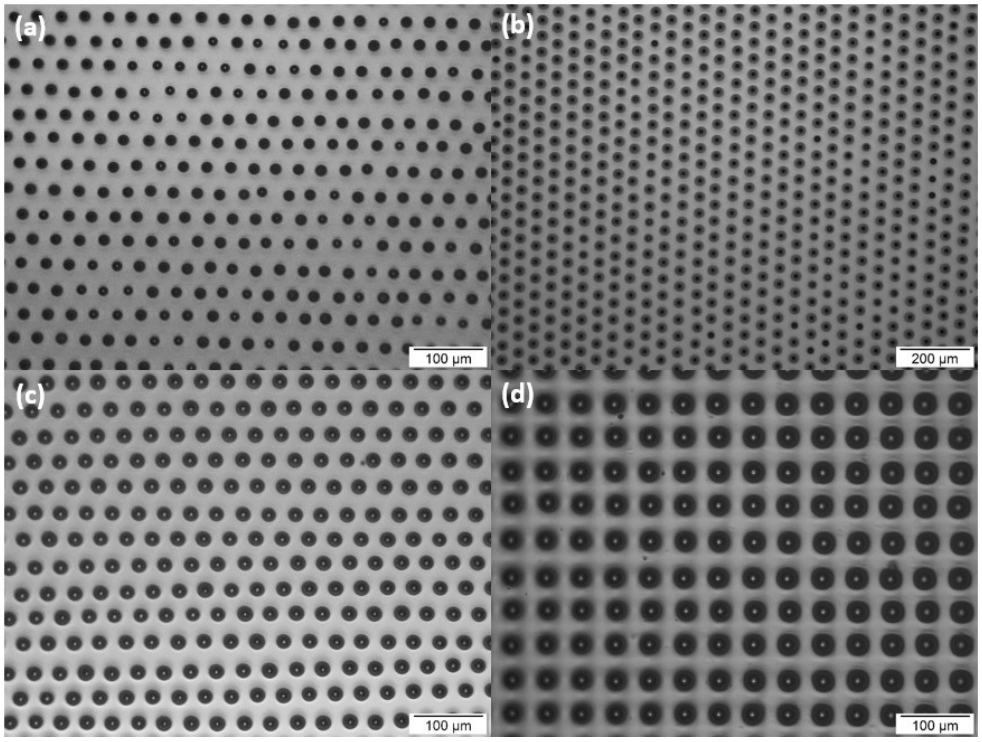

Figure 6.17 Porous structure with encapsulated functional materials. (a) CNTs. (b) FeO. (c) AuPs (d) PEG 200.

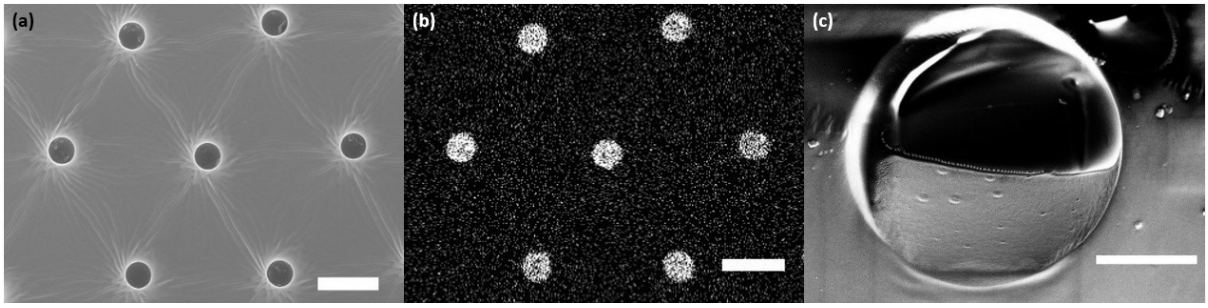

Figure 6.18 Functional materials analysis. (a) SEM image of FeO. Scale bar 20 µm. (b) EDX image of Fe. Scale bar 20 µm (c) SEM image of a cross section of PEG 1000 in the pore (significant charging). Scale bar 10 µm.

Multiple materials can be printed into the pores for capturing. This was attempted because of the need to move towards personalised drug delivery with a combination of active ingredients. Figure 6.19 (a) shows the droplets printed with a line of AuNPs alternating with a line of FeO.

The size different is due to the printing waveform and voltage changed for different inks. This is important to consider because it will have an effect on packing arrangements.

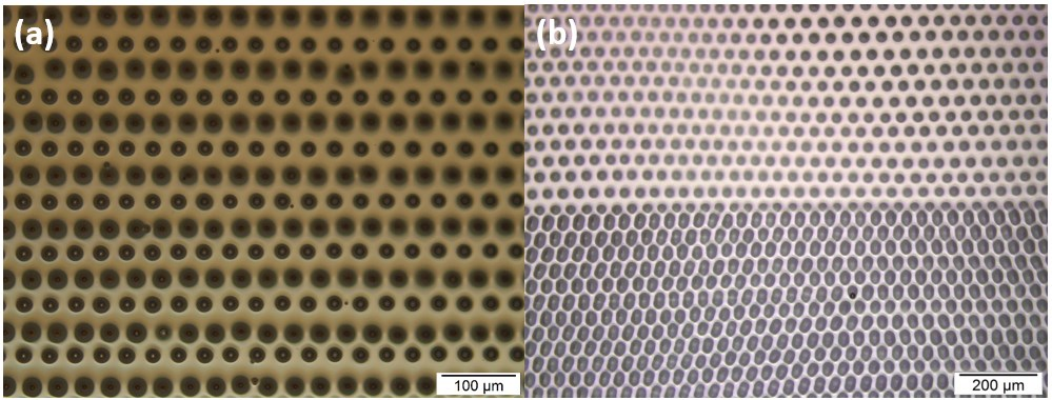

Figure 6.19 Print of two different materials and self-organisation. (a) AuNPs and FeO. (b) HCl and NaOH.

An additional application often noted for BF materials is the use for high throughput screening. This is highly challenging because of the need to post-dose materials into each pore through a very narrow opening. Here some initial tests show the first attempts at carrying out such work in fluids that are then solidified for analysis. As a drop is deposited, it forms a sphere and has an isolated volume of liquid. If an additional ingredient needs to be added, this time it can coalesce with the original drop and grow in volume, expanding as needed. The final 'beaker' or container will solidify upon curing and the reactants will still be contained within. Figure 6.19 (b) shows an initial test with an acid-base titration using a layer of hydrochloric acid (HCl) printed first and covered the lower half of the pattern with sodium hydroxide (NaOH) (thanks for Dr. Niamh Fox help with the design and formulation). At this level of scale the colour change of indicator is not viewable, therefore other methods for examination of the reaction need to be developed.

However, to see if signals could be recorded for high throughput screening applications, standard fluorescent tags were included in droplets that were printed onto a surface. mCherry and green fluorescent protein (GFP) were printed into PDMS, and the confocal microscope images (with thanks to Dr. Stefanie Reichelt, Cancer Research UK Cambridge Centre) show two different types of droplets and the fluorescence in the pores. Unfortunately the current

printing setup used has poor alignment during cartridge changeover and so the packing was quite random in this case. However, this final set of experiments demonstrated that the inkjet technique is compatible with a lot of materials in contrast to the BF method, where the content is only water droplets or occasionally ethanol. In addition, the pores can encapsulate the materials without any coalescence to ensure stable containment.

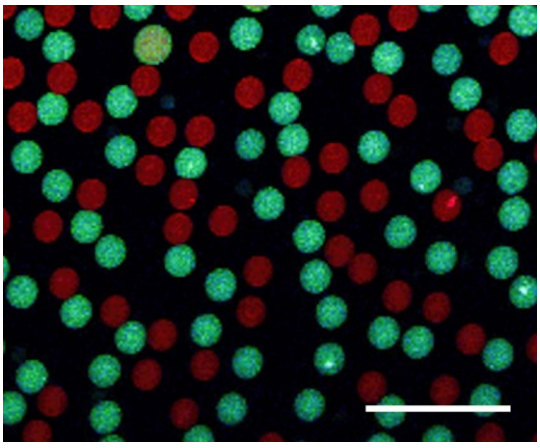

Figure 6.20 Confocal microscopy image of mCherry and GFP in PDMS. Scale bar 100 μm.

6.2.6 Pattern quality study

This chapter has followed the standard BF technique of describing ordering, through qualitative descriptions. However, it is clear that different conditions for droplets self-organisation including temperature, spacing, patterning, PDMS curing time and different materials in the droplet have a significant influence on the final structure of the pores and the packing. The porosity and the arrangement are the main determinates of the functionality of porous polymer. Therefore it is important to define the porosity and the packing mode. This will be especially important to automate as the next steps in the research will need to include moving to industrial scale printing and rapid measurement of results. The porosity can be determined by the distribution of the size of the pores and the FIB can show the cross-section of the pores, which displays the shape of the pore. A method was developed here to quantify the arrangement of pores by analysing the angle distributions.

A script was written to plot the angle distribution. First the images were analysed with ImageJ with thresholding technique and particle analysis was used to find the centre coordinates X and

Y values for all the pores in the image. Then these values were exported and all the adjacent centres were connected with lines, and the angle between each line was measured. This could be used to create a histogram of the angle distribution can then be plotted. For hexagonal close packed patterns, if the centres of the pores are connected, the angle between each neighbouring line should be 60° as all of them are equilateral triangles. Figure 6.21 (a) is the threshold image the hexagonally close packed sample examined with this method.

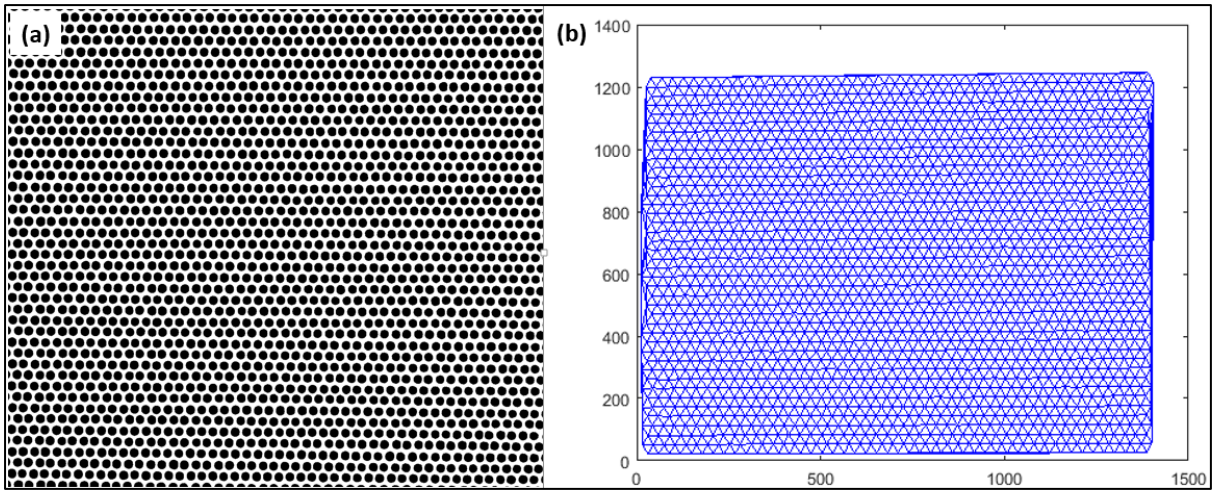

Figure 6.21 Ordering of hexagonal packing of pores in PDMS. (a) Threshold image. (b) Connected centre of pores.

The centre of each identified pore is recorded by 'particle analysis' function of ImageJ software. Extracting the information of the X and Y value of the centres and running the script with these values as input gives the output shown in Figure 6.21 (b), with the connections between all the neighbouring centres of the pores. The same method is applied to a cubic packing sample, which is demonstrated in Figure 6.22 (a) and (b). It is obvious from the connected image, for cubic packing, there are two majority angles, one is 45° the other is 90°, and for perfect cubic packing, the number of 45° is twice the number of 90°. Then the angles were calculated and distributed in the histograms in Figure 6.23. In Figure 6.23 (a) the distribution of angles in a relatively ordered hexagonal sample, there is a main peak around 60°, while there are two peaks in Figure 6.23 (b), which is for the cubic packing, one is around 45° the other is at 90°.

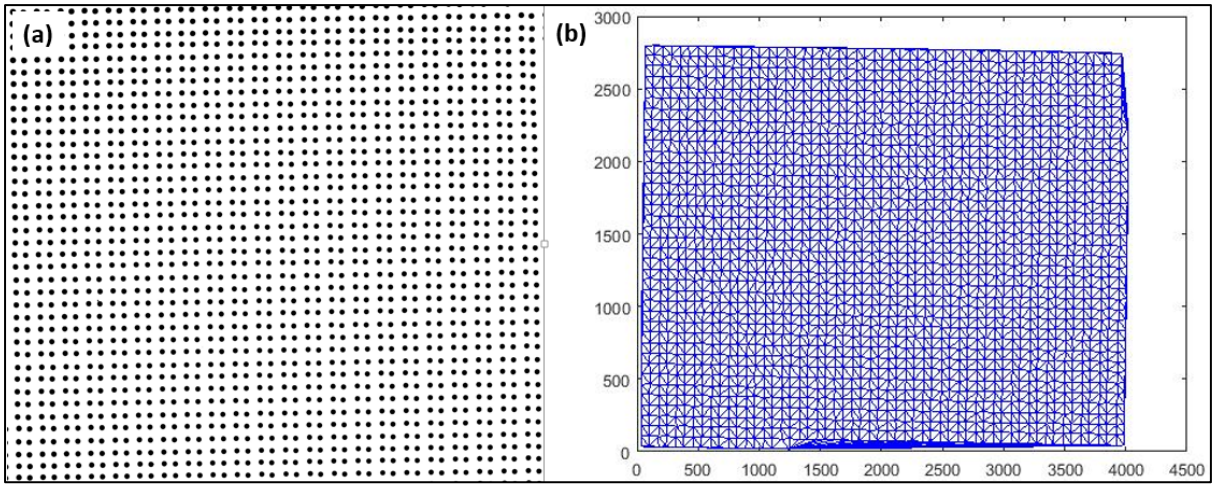

Figure 6.22 Ordering of cubic packing of pores in PDMS. (a) Threshold image. (b) Connected centre of pores.

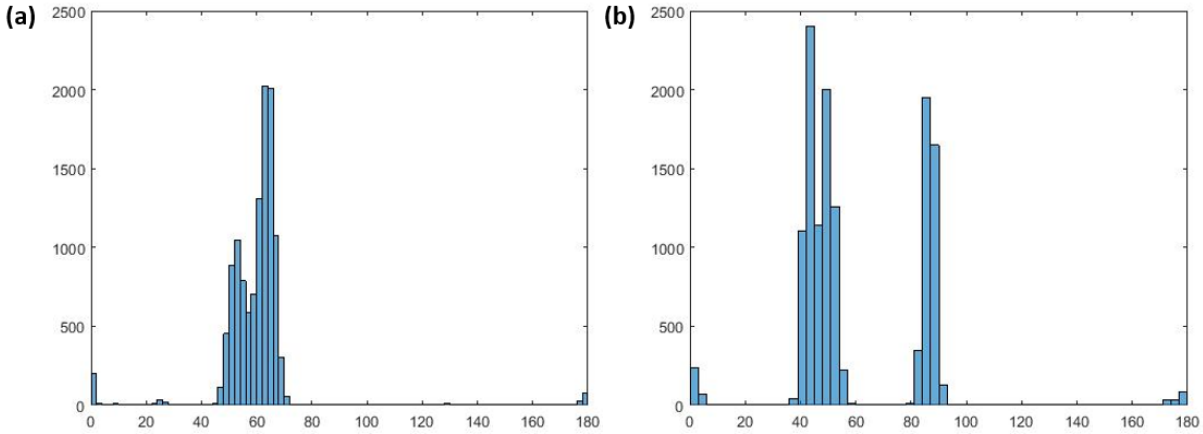

Figure 6.23 Angle distribution. (a) Hexagonal packing. (b) Cubic packing.

Then this measurement of angles were tested for some unpacked patterns for less than 8 h curing time samples, the angle distribution revealed spread trend, however the peak is always around 50°-60°, which means the droplet self-organisation has the tendency of finding the hexagonal packing when the restriction of PDMS is absent. The limitation of this model is the distance between the droplets is not considered. Comparing Figure 6.24 (a) and (d), the very close packed region of droplets on the top of the image were not recognised by the ImageJ particle analysis plug-in, then these were not plotted in (d), which leads to errors in the analysis. In Figure 6.24 (b), the defects can have an influence on the quality of the polymer samples, and it can be detected by this method, which is demonstrated in (e) that the 'blank' areas are the

defects. Figure 6.24 (c) is a non-packed sample, it is also clear from the image (f) as the connections between each centre have left large spaces in between.

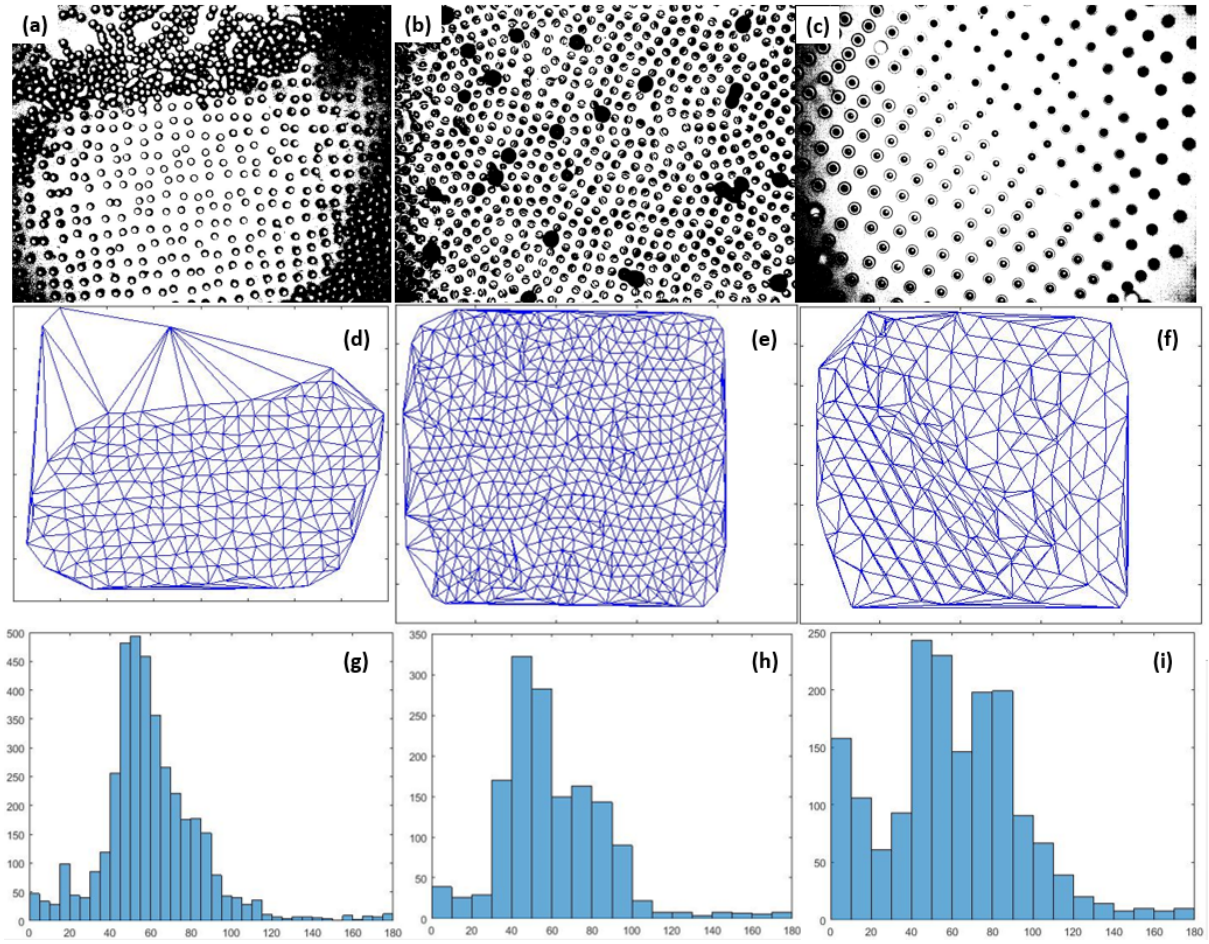

Figure 6.24 Other tests with some unpacked samples. (a)-(c) Threshold images. (d)-(f) Connected centre of pores. (g)-(h) Angle distribution.

6.3 Polymer patterning with inkjet generated templates and self-organisation conclusion and summary

This new method of PDMS patterning showed different levels of control of porosity. The printed pattern can affect the arrangement of droplets when they packed closer, as the minimum energy pattern is the hexagonal close packed pattern. When printed into cubic arrays, the

droplets struggled to pack into hexagonal arrays, then defects occurred. This can be amended easily by printing the droplets into hexagonal arrays originally, then driving them close together, more ordered structures can be obtained. At high temperature, also discussed in the previous chapter, droplets had excessive energy to pack, they started to overlap and the convection current also dragged them fully into the substrate. Lowering the packing temperature can reduce the overlap, but is not the optimum temperature for PDMS to cure. The rheology study of PDMS offered a novel approach of porosity design, as PDMS cures under room temperature once mixed with cross-linking agent, after certain amount of time for cure, the viscosity of PDMS increased and the increasing viscosity can restrict the convection, which can lead to highly ordered structures. This is a similar approach to manufacturing with adhesives and using their taking account of their potting life. Moreover, at long curing time (after 10 h), the geometry of the pore changed as the viscosity is too high to fully flow to allow a spherical water droplet and some of the PDMS has cured, which make it more difficult for PDMS to deform. This showed that after 24 h curing time under room temperature, droplets still could pattern PDMS, but the pattern can only leave imprints on the surface of PDMS instead of captured by PDMS. These results revealed that there is still potential of manipulation of the porosity with the aid of rheology. The wide range of packing results here and in the BF literature meant the work was concluded by developing a simple model to examine the quality of the PDMS packing, with the main focus to analyse the angle between each centre-to-centre lines and obtain the distribution of the angles. This method can be improved by a more explicit definition of the range of the acceptable angle values and get a more compact distribution. This final results chapter combines the fundamental research of drop-liquid interactions with the patterning through convection to allow final capturing of multiple materials and a route to both the manufacturing scale-up and validation work required to ensure manufacturing of functional porous films to the correct manufacturing standards. The following chapter will bring together these results and examine where this will guide the field in the future.

Chapter 7 Conclusions and future research

7.1 Conclusions

Breath figure is the term for droplets condensed on cold surfaces, which was first studied by Rayleigh in 1911. In 1994, droplets of breath figure pattern were discovered to self-organise on polymer solutions and template a honeycomb morphology of polymer sheets. This method is simpler and cheaper compared with lithographic techniques in patterning surfaces. There are a lot of applications for the porous films made from breath figure methods, for instance optical devices, cell scaffolds, separation filters, drug delivery systems and templates for further patterning. However, in the breath figure method the quality of the pores is extremely sensitive to the humidity and air flowrate as the key mechanism of this method is the condensation of water droplets, and these factors are difficult to control to a sufficient accuracy. Also there are other potential limitations that hinder this technique from being translated to manufacturing.

This thesis has started with a hypothesis that direct deposition of droplets could be an alternative and potentially more manufacturable approach to making highly ordered porous polymers. Inkjet printing was the chosen technique to create the droplet template instead of condensation, with the aid of droplets self-organisation. In order to conclude on the potential of this approach, three main areas of research were completed and discussed.

Firstly, inkjet printing research rarely includes a detailed analysis of the control over droplet velocity and volume for the full range of printing conditions required. This is critical to understand the ejection of droplets from commercially available inkjet printheads of different sizes, the control via manipulating driving signals and the ability to ensure single drops every time. The signals were developed to generate single droplet for each print and the home-build high-speed imaging system was used to capture the performance of the droplets for further analysis. The results show that inkjet printing is a stable and efficient way of generating micron level droplets of the same size once there is significant optimisation of the waveform and inks. Therefore the printing conditions, including the size of the nozzle and waveforms for the glycerol water solutions, used in this research are transferable to other similar setups and this will help with future research upon further distribution of these detailed results. Different

impact behaviours were observed during the research, and so a detailed study was carried out to identify regions where defined behaviours could be identified. These impact behaviours have not previously been reported for such a system, in particular the delayed coalescence behaviour. These show clear links to the importance of impact velocity and the Weber number of the droplets. This initial section also examined the surface tension driven stabilisation at the substrate/air interface and the contact angle manipulation.

The second part of this research discussed the stability of multiple droplets as they interacted within a fluid. This is not feasible with the breath figure method and so led to exciting evidence of droplet stability within fluids. Two droplets were brought into contact during printing and for each liquid substrate system the critical distance between two droplets to keep them separate after printing was defined, which is critically important for later pattern design. It is found that the droplets can still keep separate after contact each other except for those hitting the 'cap' of the water droplet appearing above the liquid substrate surface. Then droplet arrays stability on PDMS was studied by driving packing and self-organisation. Due to the highly viscous liquid used for this work, only overlapping of droplets was observed instead of coalescence as polymers around the droplets act as lubrication layers and do not drain easily from between the drops.

The final part of the research contributed to the porous polymer preparation methods, this is a new approach, which possesses significant potential of scaling up the production of ordered porous polymer films. The rheology study of PDMS offered a significant insight into porosity design, as PDMS cures under room temperature once mixed with cross-linker, and the viscosity of PDMS will increase with the time. Then the high viscosity can lead to highly ordered structures and change of morphology of the pores. Even at 24 h curing time PDMS surfaces can still be patterned by droplets with round coin-like imprints. These results revealed that there is still potential of manipulation of the porosity with the aid of rheology control. During the research of printing functional materials and in-situ encapsulation, PEG 1000 was successfully captured by PDMS, which made this a more flexible technique to build a polymer-polymer system, which may have a potential application in drug delivery devices. Also a model was developed to examine the quality of the PDMS packing, the main focus is to analyse the

angle between each centre-to-centre lines and obtain the distribution of the angles, which can then provide a much needed quantification of this parameter to the field.

In conclusion the answers to the research questions can be summarised as follows:

1) Can direct deposition of liquids (inkjet printing) be used to make porous materials?
2) To what extent can the pore morphology and the surface properties be controlled?

Inkjet printing technique has been proved as an alternative to BF method in producing porous polymers. Also this technique can pattern PDMS which is not compatible with the BF method. The study of drop ejection revealed that the size and the velocity of the droplets are quite consistent under the same set up, but need significant optimisation. The pore morphology, including the size, opening size, shape and the packing mode of the pores, can be manipulated by different parameters. The size of the pores can be controlled by changing the nozzle size and the voltage of printing. Generally, with larger orifice size larger droplets can be generated. The opening size is largely depend on the surface tension of both the droplet and the substrate, owing to the change of contact angle. The pores can be switched amongst three different shapes, as demonstrated in the PDMS rheology study, before 10 h curing time the pores have small openings on the surface with a round shaped cavity below it, while at 10 h curing time the hole change to a cylindrical pit and finally at 24 h curing time only shallow round shaped marks can left by droplets on the surface of PDMS.

3) How can we produce stable monodisperse, stable rafts of droplets suitable for templating by the inkjet printing technique?

Monodisperse droplet arrays that can be used as templates to pattern PDMS were generated by the DMP, which shows the high efficiency and accuracy of this top-down deposition technique. This is a tool used by industry to help with scale-up although is not an industrial printhead, which would need to be tried in the next stage. In addition, using DMP software, the pattern of droplets can be designed by programming as well as importing of images, which offers great freedom in pattern design. As the breath figure method mainly depends upon the random condensation and growth of water droplets over the whole surface, and coalescence can happen right after droplet contact, thus droplet coalescence is unavoidable. In contrast, in the study of two-droplet stability after contact during printing showed that it

is more stable for when interacting with one drop already stabilised at the substrate/air interface and surrounded by the substrate liquid due to surface tension effects. Although droplets can keep separate after contact, it is more reliable to print droplets at the distance that they cannot contact during the deposition process.

4) Can we control the ratio of the opening to the internal diameter of the pores?

As noted earlier, the opening to the internal diameter of the pores is controlled by the surface tension of both the droplets and the substrate. For the same droplets on different substrates the ratio is different. The measured results of this ratio for 50 % GW droplets on vegetable oil is 0.32 ± 0.03, on octyl acetate is 0.30 ± 0.05, and on PDMS is 0.12 ± 0.02. This ratio then related to the contact angle, on vegetable oil is 161.3° ± 1.8°, on octyl acetate is 162.5° ± 3.0°, and on PDMS is 173.1° ± 1.1°. With modified viscosity, the influence on the ratio is not obvious, however the change in the shape of the pores is quite significant due to the dynamic capturing in the curing polymer.

5) What is the relationship between drops/substrate properties and the impact behaviours?

When droplets impact on vegetable oil only one impact behaviour was observed, which is the droplet gradually submerging into the oil and finally pinning at the interface. Impact on PDMS showed the same submerging process, but taking a longer time to stabilise due to the high viscosity. Noticeable impact behaviour of droplets on PDMS was observed that the droplets collision upon PDMS surface resembles the impact behaviour on a solid surface as the drop can deform can squeeze into a patty-shape then oscillate and recover to steady state above the PDMS surface first. Nevertheless, three impact behaviours were observed for droplets impact on octyl acetate surface: bouncing, temporary non-coalescence, and penetration. In both the literature and this research there is no sharp boundary for the droplets to rebound from the impact liquid substrate, however regions can be defined where the possibility of bouncing is higher than other behaviours. There are a few parameters examined that are correlated to the bouncing behaviours of the droplets on octyl acetate: diameter of the impact droplet, impact velocity, and dimensionless numbers We and Re. There is no strong correlations between the diameter and the impact behaviour, but for droplets size smaller than 66.4 μm, no bouncing was witnessed. The impact velocity

of the droplets demonstrated that the penetration can still happen through the tested range, but the bouncing behaviour gathered around low velocity region (0.5 m/s to 1.2 m/s), while the temporary non-coalescence happened at even lower velocity. Region of high likelihood rebound for We is between 0.03 and 0.12. Re did not show a direct influence on the impact behaviour, but the log We – log Re plot proved that the region of rebound is between the caught and penetration.

6) What are the mechanisms of self-organisation for the droplets deposited on liquid surfaces?

The self-organisation of droplets on PDMS surfaces was driven by convection induced by heating applied from below. The visualisation of convection in a weighing boat made it clear that the convection happened when PDMS heated on a hot plate at 80 °C. The convection current on the surface of PDMS is contracting to the centre of the weighing boat, and in the middle descending, then all the parts under the surface is drawing to the bottom and circling to the edge of the container where the current ascending. Droplets self-organisation tend to pack in a hexagonal closed packed pattern, convection can provide the energy to pack and self-organise. Low temperature convection can form a more ordered structure but not close packed, while too high the temperature can results in the overlap of droplets, which formed multiple layers of pores. PDMS cured for various times was studied, and the convection videos were captured, it revealed that for longer curing times the time required for the convection to pack the pattern is extended, but a more ordered pattern can form after self-organisation.

7) Can this new level of control give a better understanding of the self-organisation to switch between different packing modes (for example hexagonal or square arrays), or reduce coalescence/overlap?

Rheological studies of PDMS enables the change of arrangement of the droplets, as from 8 h curing time, PDMS is partly cured and the viscosity is high enough to limit the convection, highly ordered hexagonal arrays can obtain at this time of curing time. At 6 h an improved pattern is possible compared with 1 h curing time where most droplet overlapping happened. Also starting from 8 h curing time, cubic arrays can be achieved

after PDMS heated to fully cure. At 24 h, the pattern can be fully captured (marks on surface) without any movement. Coalescence of droplets after separately printed at PDMS/air interface will not happen under the conditions in this research.

7.2 Future research

With these questions addressed, future research should focus on the application and scale up of this method. Drug delivery device is of great interest in both future researches and manufacturing. The successful innovations in this technique would very likely have huge positive effects on the treatment of various diseases, where combinations of drugs need to be personalised and implanted or delivered to a dissolvable polymer matrix. To control the release rate, time and place of the drug in the body, the main components of the drug delivery device is the reservoir of drug, the orifice or membrane that can control the flowrate or penetration rate of the formulation and the functional group to match with the specific target within the body. As in this research, the control of the pore size by controlling the contact angle of the droplets on the substrate has been demonstrated, it is viable to further investigate the opening size affected drug release speed. The device itself should be made from biodegradable materials to avoid a second operation to get it out of the body. Hence, biodegradable polymer sheets are considered to possess significant potential in the design and manufacturing of drug delivery devices. PDMS was patterned with this new method, which is one of the most widely used silicone elastomers. Although this polymer is not biodegradable, its rubber-like elasticity, elasticity and biocompatibility made it perfect for implanted long-time drug carrier. Also this method can be tested on other polymers to find what type of polymers are compatible with this method. Initial work showed that the BF method can now be translated to rapidly incorporate almost any functional material, as long as it can be printed within a suitable non-coalescing fluid. Except for these applications, the rheological study of PDMS in this research showed that an additional levels of control is feasible to give square or hexagonal arrays, and also different geometries of pore. This needs to be explored in more detail to realise the full extent of this flexibility. Finally, it is important now to seek collaborations with industry to practically scale up the production of porous polymers with this approach and move this method towards a helpful engineered solution.

References

[1] Q. Liu, Z. Tang, B. Ou, L. Liu, Z. Zhou, S. Shen, and Y. Duan, "Design, preparation, and application of ordered porous polymer materials," *Materials Chemistry and Physics*. 2014.

[2] H. M. El-Kaderi, J. R. Hunt, J. L. Mendoza-Cortés, A. P. Côté, R. E. Taylor, M. O'Keeffe, and O. M. Yaghi, "Designed synthesis of 3D covalent organic frameworks.," *Science*, vol. 316, no. 5822, pp. 268–72, Apr. 2007.

[3] D. Wu, F. Xu, B. Sun, R. Fu, H. He, and K. Matyjaszewski, "Design and preparation of porous polymers.," *Chem. Rev.*, vol. 112, no. 7, pp. 3959–4015, Jul. 2012.

[4] L. Connal, "Ordered, porous and multifaceted polymer films," *Old.Iupac.Org*, no. Scheme 1, pp. 1–11, 2008.

[5] R. B. Wehrspohn, *Ordered Porous Nanostructures and Applications*. Springer Science & Business Media, 2006.

[6] C. Wang, Y. Mao, D. Wang, Q. Qu, G. Yang, and X. Hu, "Fabrication of highly ordered microporous thin films by PS-b-PAA self-assembly and investigation of their tunable surface properties," *J. Mater. Chem.*, vol. 18, no. 6, p. 683, 2008.

[7] A. Bolognesi, C. Mercogliano, S. Yunus, M. Civardi, D. Comoretto, and A. Turturro, "Self-organization of polystyrenes into ordered microstructured films and their replication by soft lithography," *Langmuir*, vol. 21, no. 8, pp. 3480–3485, 2005.

[8] N. Kurono, R. Shimada, T. Ishihara, and M. Shimomura, "Fabrication and Optical Property of Self-Organized Honeycomb-Patterned Films," *Mol. Cryst. Liq. Cryst.*, vol. 377, no. 1, pp. 285–288, 2002.

[9] L. Ghannam, H. Garay, J. François, and L. Billon, "New Polymeric Materials with Interferential Optical Properties," *Macromol. Chem. Phys.*, vol. 208, no. 13, pp. 1469–1479, Jul. 2007.

[10] S. Chen, X. Lu, Z. Huang, and Q. Lu, “In situ growth of a polyphosphazene nanoparticle coating on a honeycomb surface: facile formation of hierarchical structures for bioapplication,” *Chem. Commun.*, vol. 51, no. 26, pp. 5698–5701, 2015.

[11] S. Chen, X. Lu, Y. Hu, and Q. Lu, “Biomimetic honeycomb-patterned surface as the tunable cell adhesion scaffold,” *Biomater. Sci.*, vol. 3, no. 1, pp. 85–93, 2015.

[12] P. C. Chen, L. S. Wan, B. B. Ke, and Z. K. Xu, “Honeycomb-patterned film segregated with phenylboronic acid for glucose sensing,” *Langmuir*, vol. 27, no. 20, pp. 12597–12605, 2011.

[13] Y. Xia, J. a. Rogers, K. E. Paul, and G. M. Whitesides, “Unconventional Methods for Fabricating and Patterning Nanostructures.,” *Chem. Rev.*, vol. 99, no. 7, pp. 1823–1848, 1999.

[14] Y. N. Xia and G. M. Whitesides, “Soft lithography,” *Annu. Rev. Mater. Sci.*, vol. 37, no. 5, pp. 551–575, 1998.

[15] D. Qin, Y. Xia, and G. M. Whitesides, “Soft lithography for micro- and nanoscale patterning,” *Nat. Protoc.*, vol. 5, no. 3, pp. 491–502, 2010.

[16] J.-S. Lee, S. H. Joo, and R. Ryoo, “Synthesis of Mesoporous Silicas of Controlled Pore Wall Thickness and Their Replication to Ordered Nanoporous Carbons with Various Pore Diameters,” *J. Am. Chem. Soc.*, vol. 124, no. 7, pp. 1156–1157, Feb. 2002.

[17] A. Stein and R. C. Schroden, “Colloidal crystal templating of three-dimensionally ordered macroporous solids: materials for photonics and beyond,” *Curr. Opin. Solid State Mater. Sci.*, vol. 5, no. 6, pp. 553–564, Dec. 2001.

[18] P. Jiang, J. F. Bertone, K. S. Hwang, and V. L. Colvin, “Single-Crystal Colloidal Multilayers of Controlled Thickness,” *Chem. Mater.*, vol. 11, no. 8, pp. 2132–2140, 1999.

[19] G. Widawski, M. Rawiso, and B. François, “Self-organized honeycomb morphology of star-polymer polystyrene films,” *Nature*, vol. 369, no. 6479, pp. 387–389, Jun. 1994.

[20] Lord Rayleigh, “Breath Figures,” *Nature*, vol. 86, no. 2169, pp. 416–417, 1911.

[21] A. Steyer, P. Guenoun, D. Beysens, and C. M. Knobler, “Two-dimensional ordering during droplet growth on a liquid surface,” *Phys. Rev. B*, vol. 42, no. 1, pp. 1086–1089, Jul. 1990.

[22] a. Limaye, R. Narhe, a. Dhote, and S. Ogale, “Evidence for Convective Effects in Breath Figure Formation on Volatile Fluid Surfaces,” *Phys. Rev. Lett.*, vol. 76, no. 20, pp. 3762–3765, 1996.

[23] L.-S. Wan, L.-W. Zhu, Y. Ou, and Z.-K. Xu, “Multiple interfaces in self-assembled breath figures.,” *Chem. Commun. (Camb).*, vol. 50, no. 31, pp. 4024–39, 2014.

[24] J. J. Boland, “Porous Polymer Surfaces Novel technique that allows users to create porous films with micron to nanoscale pores whose depth , shape and function can all be controlled in a simple , robust , single step process .”

[25] M. H. Stenzel, C. Barner-Kowollik, and T. P. Davis, “Formation of honeycomb-structured, porous films via breath figures with different polymer architectures,” *J. Polym. Sci. Part A Polym. Chem.*, vol. 44, no. 8, pp. 2363–2375, Apr. 2006.

[26] U. H. F. Bunz, “Breath figures as a dynamic templating method for polymers and nanomaterials,” *Adv. Mater.*, vol. 18, no. 8, pp. 973–989, 2006.

[27] M. Srinivasarao, D. Collings, a Philips, and S. Patel, “Three-dimensionally ordered array of air bubbles in a polymer film.,” *Science*, vol. 292, no. 5514, pp. 79–83, Apr. 2001.

[28] S. Xu, M. Li, Z. Mitov, and E. Kumacheva, “Surface textures induced by convection in thin films of polymeric and polymerizable fluids,” *Prog. Org. Coatings*, vol. 48, no. 2–4, pp. 227–235, 2003.

[29] M. Hernández-Guerrero and M. H. Stenzel, “Honeycomb structured polymer films via breath figures,” *Polym. Chem.*, vol. 3, no. 3, pp. 563–577, Feb. 2012.

[30] N. Maruyama, T. Koito, J. Nishida, T. Sawadaishi, X. Cieren, K. Ijiro, O. Karthaus,

and M. Shimomura, “Mesoscopic patterns of molecular aggregates on solid substrates,” *Thin Solid Films*, vol. 327–329, pp. 854–856, 1998.

[31] O. Pitois and B. François, “Crystallization of condensation droplets on a liquid surface,” *Colloid Polym. Sci.*, vol. 277, no. 6, pp. 574–578, 1999.

[32] M. H. Stenzel-Rosenbaum, T. P. Davis, and A. G. Fane, “Porous polymer films and honeycomb structures made by the self-organization of well-defined macromolecular structures created by living radical polymerization techniques,” *Angew. Chemie - Int. Ed.*, vol. 40, no. 18, pp. 3428–3432, 2001.

[33] N. E. Zander, J. a. Orlicki, A. S. Karikari, T. E. Long, and A. M. Rawlett, “Super-hydrophobic surfaces via micrometer-scale templated pillars,” *Chem. Mater.*, vol. 19, no. 25, pp. 6145–6149, 2007.

[34] A. Bolognesi, F. Galeotti, U. Giovanella, F. Bertini, and S. Yunus, “Nanophase separation in polystyrene-polyfluorene block copolymers thin films prepared through the breath figure procedure,” *Langmuir*, vol. 25, no. 9, pp. 5333–5338, 2009.

[35] J. Peng, Y. Han, Y. Yang, and B. Li, “The influencing factors on the macroporous formation in polymer films by water droplet templating,” *Polymer (Guildf).*, vol. 45, no. 2, pp. 447–452, Jan. 2004.

[36] I. J. Chin, S. C. Lee, and S. Quan, “Preparation and characterization of surfactant-induced nanoporous PMMA film,” *J. Ind. Eng. Chem.*, vol. 15, no. 1, pp. 136–140, 2009.

[37] B. You, N. Wen, S. Zhou, L. Wu, and D. Zhao, “Facile method for fabrication of nanocomposite films with an ordered porous surface.,” *J. Phys. Chem. B*, vol. 112, no. 26, pp. 7706–7712, 2008.

[38] M. S. Park and J. K. Kim, “Breath figure patterns prepared by spin coating in a dry environment,” *Langmuir*, vol. 20, no. 13, pp. 5347–5352, 2004.

[39] M. S. Park and J. K. Kim, “Broad-band antireflection coating at near-infrared wavelengths by a breath figure,” *Langmuir*, vol. 21, no. 24, pp. 11404–11408, 2005.

[40] S. a. Jenekhe, “Self-Assembly of Ordered Microporous Materials from Rod-Coil Block Copolymers,” *Science (80-.).*, vol. 283, no. 5400, pp. 372–375, 1999.

[41] B. B. De Boer, U. Stalmach, H. Nijland, and G. Hadziioannou, “Microporous Honeycomb-Structured Films of Semiconducting Block Copolymers and Their Use as Patterned Templates,” *Adv. Mater.*, no. 21, pp. 1581–1583, 2000.

[42] J.-P. Gao, W. Wu, L. Rong, G.-L. Mao, Y.-N. Ning, Q.-L. Zhao, J. Huang, and Z. Ma, “Well-defined monocarboxyl-terminated polystyrene with low molecular weight: A candidate for the fabrication of highly ordered microporous films and microspheres via a static breath-figure process,” *Eur. Polym. J.*, vol. 59, pp. 171–179, Oct. 2014.

[43] B. H. Wu, L. W. Wu, K. Gao, S. H. Chen, Z. K. Xu, and L. S. Wan, “Self-Assembly of Patterned Porous Films from Cyclic Polystyrenes via the Breath Figure Method,” *J. Phys. Chem. C*, vol. 122, no. 7, pp. 3926–3933, 2018.

[44] E. Ji, V. Pellerin, F. Ehrenfeld, A. Laffore, A. Bousquet, and L. Billon, “Hierarchical honeycomb-structured films by directed self-assembly in ‘breath figure’ templating of ionizable ‘clicked’ PH3T-: B -PMMA diblock copolymers: An ionic group/counter-ion effect on porous polymer film morphology,” *Chem. Commun.*, vol. 53, no. 11, pp. 1876–1879, 2017.

[45] B. Yao, Q. Zhu, L. Yao, and J. Hao, “Fabrication of honeycomb-structured poly(ethylene glycol)-block-poly(lactic acid) porous films and biomedical applications for cell growth,” *Appl. Surf. Sci.*, vol. 332, pp. 287–294, 2015.

[46] R. Daly, J. E. Sader, and J. J. Boland, “The dominant role of the solvent–water interface in water droplet templating of polymers,” *Soft Matter*, vol. 9, no. 33, p. 7960, 2013.

[47] N. Pionnier, S. Boroomandi Barati, E. Contraires, R. Berger, M. Guibert, S. Benayoun, and S. Valette, “Design of an environment controlled dew tracking setup to emphasize the role of the relative humidity on breath figures dynamics,” *EPJ Tech. Instrum.*, vol. 5, no. 1, p. 2, 2018.

[48] F. Galeotti, I. Chiusa, L. Morello, S. Gianì, D. Breviario, S. Hatz, F. Damin, M. Chiari, and A. Bolognesi, "Breath figures-mediated microprinting allows for versatile applications in molecular biology," *Eur. Polym. J.*, vol. 45, no. 11, pp. 3027–3034, 2009.

[49] A. Zhang, H. Bai, and L. Li, "Breath Figure: A Nature-Inspired Preparation Method for Ordered Porous Films," *Chem. Rev.*, p. 150818142718002, 2015.

[50] M. J. Mullan and P. a Campbell, "Breath-figure polymer films with local microporosity controlled via spatio-thermal templating.," *Conf. Proc. IEEE Eng. Med. Biol. Soc.*, vol. 2008, pp. 2514–2517, 2008.

[51] H. Yabu and M. Shimomura, "Simple fabrication of micro lens arrays.," *Langmuir*, vol. 21, no. 5, pp. 1709–11, Mar. 2005.

[52] Y. Lu, Y. Ren, L. Wang, X. Wang, and C. Li, "Template synthesis of conducting polyaniline composites based on honeycomb ordered polycarbonate film," *Polymer (Guildf).*, vol. 50, no. 9, pp. 2035–2039, Apr. 2009.

[53] L. Li, J. Li, Y. Zhong, C. Chen, Y. Ben, J. Gong, and Z. Ma, "Formation of ceramic microstructures: honeycomb patterned polymer films as structure-directing agent," *J. Mater. Chem.*, vol. 20, no. 26, p. 5446, Jun. 2010.

[54] J. Mansouri, E. Yapit, and V. Chen, "Polysulfone filtration membranes with isoporous structures prepared by a combination of dip-coating and breath figure approach," *J. Memb. Sci.*, vol. 444, pp. 237–251, Oct. 2013.

[55] L. Li, C. Chen, J. Li, A. Zhang, X. Liu, B. Xu, S. Gao, G. Jin, and Z. Ma, "Robust and hydrophilic polymeric films with honeycomb pattern and their cell scaffold applications," *J. Mater. Chem.*, vol. 19, no. 18, p. 2789, 2009.

[56] W. Wang, Y. Yao, T. Luo, L. Chen, J. Lin, L. Li, and S. Lin, "Deterministic reshaping of breath figure arrays by directional photomanipulation," *ACS Appl. Mater. Interfaces*, vol. 9, no. 4, pp. 4223–4230, 2017.

[57] U. Male, B. K. Shin, and D. S. Huh, "Polyaniline decorated honeycomb-patterned

pores: Use of a reactive vapor in breath figure method," *Polym. (United Kingdom)*, vol. 121, pp. 149–154, 2017.

[58] B. K. Shin, U. Male, and D. S. Huh, "In-situ pore filling of TiO2nanoparticles in honeycomb patterned porous films: A modified breath figure method," *Polym. (United Kingdom)*, vol. 135, pp. 1–8, 2018.

[59] N. Noor, J. Koll, C. Abetz, H. Notzke, and V. Abetz, "Continuous Production of Macroporous Films: An Alternative to Breath Figure Assembly /639/301/357/551 /639/301/923/966 /128 article," *Sci. Rep.*, vol. 7, no. 1, pp. 1–9, 2017.

[60] J. Castrejon-Pita and W. Baxter, "Future , Opportunities and Challenges of Inkjet Technologies," *At. ...*, pp. 1–13, 2013.

[61] G. D. Martin and I. M. Hutchings, "Fundamentals of Inkjet Technology," in *Inkjet Technology for Digital Fabrication*, John Wiley & Sons, Ltd, 2012, pp. 21–44.

[62] G. D. Martin, S. D. Hoath, and I. M. Hutchings, "Inkjet printing - the physics of manipulating liquid jets and drops," *J. Phys. Conf. Ser.*, vol. 105, p. 012001, Mar. 2008.

[63] "Thermal Inkjet Technology | ICE." [Online]. Available: http://www.interactivecoding.co.uk/products/viper-thermal-inkjet-coder/thermal-inkjet-technology/. [Accessed: 30-Jul-2015].

[64] "Secrets Behind the Development of Epson's Micro Piezo Technology (Part 2) - Innovation - Epson." [Online]. Available: http://global.epson.com/innovation/topics/201306_03.html. [Accessed: 30-Jul-2015].

[65] R. Daly, T. S. Harrington, G. D. Martin, and I. M. Hutchings, "Inkjet printing for pharmaceutics - A review of research and manufacturing.," *Int. J. Pharm.*, Mar. 2015.

[66] M. Palo, R. Kolakovic, T. Laaksonen, A. Määttänen, N. Genina, J. Salonen, J. Peltonen, and N. Sandler, "Fabrication of drug-loaded edible carrier substrates from nanosuspensions by flexographic printing.," *Int. J. Pharm.*, Jan. 2015.

[67] B. K. Lee, Y. H. Yun, J. S. Choi, Y. C. Choi, J. D. Kim, and Y. W. Cho, "Fabrication of drug-loaded polymer microparticles with arbitrary geometries using a piezoelectric inkjet printing system.," *Int. J. Pharm.*, vol. 427, no. 2, pp. 305–10, May 2012.

[68] M. Singh, H. M. Haverinen, P. Dhagat, and G. E. Jabbour, "Inkjet printing-process and its applications.," *Adv. Mater.*, vol. 22, no. 6, pp. 673–85, Feb. 2010.

[69] S. E. Shaheen, R. Radspinner, N. Peyghambarian, and G. E. Jabbour, "Fabrication of bulk heterojunction plastic solar cells by screen printing," *Appl. Phys. Lett.*, vol. 79, no. 18, pp. 2996–2998, 2001.

[70] N. Scoutaris, M. R. Alexander, P. R. Gellert, and C. J. Roberts, "Inkjet printing as a novel medicine formulation technique," *J. Control. Release*, vol. 156, no. 2, pp. 179–185, 2011.

[71] Y. Kudo, T. Nakahara, T. Nakagama, N. Seino, M. Shinoda, and K. Uchiyama, "Development of a surface-reaction system in a nanoliter droplet made by an ink-jet microchip.," *Anal. Sci.*, vol. 23, no. 1, pp. 91–95, 2007.

[72] C. N. Hoth, S. a. Choulis, P. Schilinsky, and C. J. Brabec, "On the effect of poly(3-hexylthiophene) regioregularity on inkjet printed organic solar cells," *J. Mater. Chem.*, vol. 19, no. 30, p. 5398, 2009.

[73] C. Waldauf, M. Morana, P. Denk, P. Schilinsky, K. Coakley, S. a. Choulis, and C. J. Brabec, "Highly efficient inverted organic photovoltaics using solution based titanium oxide as electron selective contact," *Appl. Phys. Lett.*, vol. 89, no. 23, pp. 1–4, 2006.

[74] Y.-T. Kwon, Y.-I. Lee, K.-J. Lee, Y.-M. Choi, and Y.-H. Choa, "A Novel Method for Fine Patterning by Piezoelectrically Induced Pressure Adjustment of Inkjet Printing," *J. Electron. Mater.*, 2015.

[75] S. Jeong, H. C. Song, W. W. Lee, S. S. Lee, Y. Choi, W. Son, E. D. Kim, C. H. Paik, S. H. Oh, and B.-H. Ryu, "Stable aqueous based Cu nanoparticle ink for printing well-defined highly conductive features on a plastic substrate.," *Langmuir*, vol. 27, no. 6, pp. 3144–9, Mar. 2011.

[76] “MicroFab Technologies. INC-Low Temp. Devices.” [Online]. Available: http://www.microfab.com/dispensing-devices/low-temp-devices. [Accessed: 27-Apr-2018].

[77] I. The, “Satellites occurrence and approaches to eliminate them,” pp. 1–4, 2007.

[78] “Principles - ImageJ.” [Online]. Available: http://imagej.net/Principles#Why_.28lossy.29_JPEGs_should_not_be_used_in_imaging. [Accessed: 04-Jun-2018].

[79] M. Yamaki, J. Higo, and K. Nagayama, “Size-Dependent Separation of Colloidal Particles in Two-Dimensional Convective Self-Assembly,” *Langmuir*, vol. 11, no. 8, pp. 2975–2978, 1995.

[80] A. U. Chen and O. A. Basaran, “A new method for significantly reducing drop radius without reducing nozzle radius in drop-on-demand drop production,” *Phys. Fluids*, vol. 14, no. 1, 2002.

[81] H. Dong, W. W. Carr, and J. F. Morris, “An experimental study of drop-on-demand drop formation,” *Phys. Fluids*, vol. 18, no. 7, 2006.

[82] A. U. Chen, P. K. Notz, and O. A. Basaran, “Computational and Experimental Analysis of Pinch-Off and Scaling,” *Phys. Rev. Lett.*, vol. 88, no. 17, p. 4, 2002.

[83] J. N. Israelachvili, *Intermolecular and Surface Forces*. 2011.

[84] J. Eggers and E. Villermaux, “Physics of liquid jets,” *Reports Prog. Phys.*, vol. 71, no. 3, p. 036601, 2008.

[85] G. H. McKinley and M. Renardy, “Wolfgang von Ohnesorge,” *Phys. Fluids*, vol. 23, no. 12, pp. 0–17, 2011.

[86] A. A. Castrejón-Pita, J. R. Castrejón-Pita, and I. M. Hutchings, “Breakup of liquid filaments,” *Phys. Rev. Lett.*, vol. 108, no. 7, pp. 15–19, 2012.

[87] D. Henderson, H. Segur, L. B. Smolka, and M. Wadati, “The motion of a falling liquid filament,” *Phys. Fluids*, vol. 12, no. 3, pp. 550–565, 2000.

[88] R. M. S. M. Schulkes, “The contraction of liquid filaments,” *J. Fluid Mech.*, vol. 309, pp. 277–300, 1996.

[89] P. K. Notz and O. A. Basaran, “Dynamics and breakup of a contracting liquid filament,” *J. Fluid Mech.*, vol. 512, pp. 223–256, 2004.

[90] A. M. Worthington, “On the forms assumed by drops of liquids falling vertically on a horizontal plate,” *Proc. R. Soc. London*, vol. 25, pp. 261–272, 1876.

[91] A. M. Worthington, “A Second Paper on the Forms Assumed by Drops of Liquids Falling Vertically on a Horizontal Plate.,” *Proc. R. Soc. London*, vol. 25, no. 171–178, pp. 498–503, 1876.

[92] R. M. Schotland, “Experimental results relating to the coalescence of water drops with water surfaces,” *Discuss. Faraday Soc.*, vol. 30, p. 72, 1960.

[93] J. W. Strutt, *The theory of sound. Vol. 2 of 2.*, 2nd ed. New York: Dover, 1945.

[94] B. M. W. G. and T. J. J. Ching, “Droplet impacts upon liquid surfaces,” *Science (80-.).*, no. November, pp. 1–3, 1984.

[95] S. L. Zhbankova and A. V. Kolpakov, “Collision of water drops with a plane water surface,” *Fluid Dyn.*, vol. 25, no. 3, pp. 470–473, 1990.

[96] M. Rein, “Phenomena of liquid drop impact on solid and liquid surfaces,” *Fluid Dyn. Res.*, vol. 12, no. 2, pp. 61–93, 1993.

[97] G. A. Bach, D. L. Koch, and A. Gopinath, “Coalescence and bouncing of small aerosol droplets,” *J. Fluid Mech.*, vol. 518, pp. 157–185, 2004.

[98] K. L. Pan and C. K. Law, “Dynamics of droplet-film collision,” *J. Fluid Mech.*, vol. 587, pp. 1–22, 2007.

[99] Q. Huang and H. Zhang, “A study of different fluid droplets impacting on a liquid film,” *Pet. Sci.*, vol. 5, no. 1, pp. 62–66, 2008.

[100] O. W. Jayaratne and B. J. Mason, “The Coalescence and Bouncing of Water Drops at

an Air/Water Interface," *Proc. R. Soc. A Math. Phys. Eng. Sci.*, vol. 280, no. 1383, pp. 545–565, 1964.

[101] P. . Pujado and L. . Scriven, "Sessile lenticular configurations: Translationally and rotationally symmetric lenses," *J. Colloid Interface Sci.*, vol. 40, no. 1, pp. 82–98, Jul. 1972.

[102] G. K. Batchelor, *An introduction to fluid dynamics*. Cambridge university press, 2000.

[103] Z. Cao and A. V. Dobrynin, "Polymeric Droplets on Soft Surfaces: From Neumann's Triangle to Young's Law," *Macromolecules*, vol. 48, no. 2, pp. 443–451, 2015.

[104] A. Amirfazli and A. W. Neumann, "Status of the three-phase line tension: a review.," *Adv. Colloid Interface Sci.*, vol. 110, no. 3, pp. 121–41, Aug. 2004.

[105] R. Aveyard and J. H. Clint, "Liquid lenses at fluid/fluid interfaces," *J. Chem. Soc. Faraday Trans.*, vol. 93, no. 7, pp. 1397–1403, 1997.

[106] R. Daly, J. E. Sader, and J. J. Boland, "Existence of Micron-Scale Water Droplets at Solvent/Air Interfaces.," *Langmuir*, 2012.

[107] E. L. Koschmieder, *Bénard cells and Taylor vortices / E.L. Koschmieder.* Cambridge: Cambridge University Press, 1993.

[108] Lord Rayleigh, "LIX. *On convection currents in a horizontal layer of fluid, when the higher temperature is on the under side*," *Philos. Mag. Ser. 6*, vol. 32, no. 192, pp. 529–546, 1916.

[109] R. Society and P. Sciences, "On the Stability of a Fluid Heated from below," *Proc. Roy. Soc. London A.*, vol. 204, no. 1078, pp. 297–309, 1950.

[110] B. E. Schubert, "Electronic Supplementary Information (ESI): Variable stiffness mate- rial based on rigid low-melting-point-alloy-microstructures embedded in soft poly (dimethylsiloxane) (PDMS)," pp. 3–5, 2013.

[111] D. C. Venerus, J. D. Schieber, H. Iddir, J. D. Guzman, and A. W. Broerman, "Measurement of thermal diffusivity in polymer melts using Forced Rayleigh Light

Scattering," *J. Polym. Sci. Part B Polym. Phys.*, vol. 37, no. 11, pp. 1069–1078, 1999.

[112] W. Zeng, Y. Du, Y. Xue, and H. L. Frisch, "Solubility Parameters," *Phys. Prop. Polym. Handb.*, no. c, pp. 289–303, 2007.

[113] J. N. Lee, C. Park, and G. M. Whitesides, "Solvent Compatibility of Poly(dimethylsiloxane)-Based Microfluidic Devices," *Anal. Chem.*, vol. 75, no. 23, pp. 6544–6554, 2003.

[114] P. A. Kralchevsky and K. Nagayama, "Capillary Forces between Colloidal Particles," *Langmuir*, vol. 10, no. 1, pp. 23–36, 1994.

[115] S. Herminghaus, "Dynamics of wet granular matter," *Adv. Phys.*, vol. 54, no. 3, pp. 221–261, 2005.

[116] R. Daly, J. E. Sader, and J. J. Boland, "Taming Self-Organization Dynamics to Dramatically Control Porous Architectures," *ACS Nano*, p. acsnano.5b06082, 2016.

Appendix

Script for polymer quality analysis (angle measurement)

```
%-- 04/07/2016, 13:41 --%

a=load('C:\Users\qz250\Desktop\Pattern Delaunay\test6.txt');
x = a(:,1);
y = a(:,2);
DT=delaunayTriangulation(x,y);
figure(1)
triplot(DT)
%calculate the triangulation
tri = delaunayTriangulation(x,y);

%Plot the graph
%triplot(tri,x,y)
%hold on

%plot(x,y,'ro')
%text(x,y,strsplit(num2str(1:length(x))))

ANGall = [];
% Determine each angle
for i = 1:size(tri,1)
    per = perms(tri(i,:));
    [~, ind] = unique(per(:,2)); %avoid to calculate two time the same angle.
    per = per(ind,:); %the 3 * 3 points that create the angle of each triangle
    for j = 1:3
       P_1 = per(j,1);
       P1 = [x(P_1),y(P_1)];
       P_2 = per(j,2);
       P2 = [x(P_2),y(P_2)];
       P_3 = per(j,3);
       P3 = [x(P_3),y(P_3)];
       ANG = rad2deg(atan2(abs(det([P3-P2;P1-P2])),dot(P3-P2,P1-P2))); %P2 is the point in the middle
       fprintf('Node %d %d %d angle %f\n',P_1, P_2, P_3, ANG);
       ANGall = [ANGall; ANG];
    end
end
ANGalls= sort(ANGall);

figure(2)
histogram(ANGalls);
```